Controlling wave-matter interactions using plasmonic and photonic structures: sensing, lensing and alternative materials

Joseph Arnold Riley

Supervisor: Dr Victor Pacheco-Peña,
Prof. Noel Healy

School of Engineering,
School of Mathematics, Statistics and Physics
Newcastle University

This dissertation is submitted for the degree of
Doctor of Philosophy

EPSRC-DTP programme August 2024

I dedicate this thesis to my loving Mam, Dad and Olive.

Declaration

I hereby declare that, except where specific reference is made to the work of others, the research and contents of this thesis are original and have not been submitted in whole or in part for consideration for any other degree or qualification in this, or any other university. This dissertation is my work and contains nothing which is the outcome of work done in collaboration with others, except as specified in the text and Acknowledgements.

Joseph Arnold Riley
August 2024

Acknowledgements

I extend my sincere gratitude for the financial support from the Engineering and Physical Sciences Research Council (EPSRC) through the EPSRC DTP PhD scheme (EP/R51309X/1), which enabled me to conduct the research outlined in this thesis at the School of Engineering, Newcastle University. I am deeply thankful to my supervisor and advisor, Dr Victor Pacheco-Peña, for not only offering me this invaluable opportunity to conduct the research presented in this thesis but also for his unwavering guidance and support. His mentorship has transcended the boundaries of academia, sustaining me through some of the most challenging periods of my life. I will always cherish his assistance and encouragement. I also wish to express my appreciation to Dr Vlastimil Křápek and Dr Michal Horák for their collaboration during my Ph.D. journey. Their insights and contributions have enriched my research experience significantly.

My gratitude also extends to my friends and colleagues within MERZ court, the metamaterials and plasmonics research group, and beyond. Christian, Wasem, Tony, Ross, Alex, Will, Luke, Toby, Amy, Georgia, Josh, Peter, Immie, Merve, Conner, Chloe, Nick, and Rachel, your friendship and support have been a source of immense strength over the years. I am eternally grateful for you all.

I owe my Dad, Kathryn and family a special debt of gratitude for their unwavering support during the tumultuous times we've faced together recently. In particular, I want to profound gratitude to my beloved Mam, who passed during my Ph.D. Her love and encouragement will forever be cherished in my heart.

Lastly, I could not have done any of this without the support of Olivia Palombo who has held me together every day through all of these years. Thank you for everything.

Abstract

Manipulating electromagnetic waves through controlled wave-matter interactions has driven advances in fields such as sensing and lensing. This thesis investigates three key mechanisms. First, photonic hooks (bent light beams) are generated by optimising diffraction and scattering through two dielectric cuboids. Various configurations of the dielectrics, including differing refractive indexes and geometries, are studied and analysed, showing excellent numerical and theoretical agreement. Second, surface plasmon polariton-based lenses with meniscus-like profiles are designed using an adapted lens maker equation for dielectric-metal configurations. These lenses exhibit significant improvements in power enhancement and focal spot resolution, with further studies demonstrating robust broadband response and resilience to fabrication errors. Finally, localised surface plasmons are exploited using complementary metal-dielectric nanostructures designed based on the Babinet principle. Validated with electron energy loss spectroscopy (EELS), these plasmonic structures are employed for dielectric sensing, revealing high sensitivities (up to $\sim$650 nm/RIU) in various configurations, including thin films and small particles. In summary, this work presents innovative methods for controlling wave-matter interactions using plasmonic and photonic structures, advancing applications in sensing, lensing, and alternative materials.

Table of contents

List of figures

List of tables

Nomenclature

Greek Symbols

β	Propagation constant
∇	$\mathbf{i}\frac{\partial}{\partial x}+\mathbf{j}\frac{\partial}{\partial y}+\mathbf{k}\frac{\partial}{\partial z}$
δ	Partial derivative
ε	Permittivity
γ	Collision frequency
i	unit imaginary number $\sqrt{-1}$
λ	Wavelength
μ	Permeability
ρ	Electric charge density
θ	Angle
ω	Angular frequency

Other Symbols

$\mathbf{B}$	Electric field density
c	Speed of light $\approx 2.9979 \times 10^8 ms^{-1}$
$\times$	Cross-product of two vectors
$\mathbf{D}$	Electric field displacement
d	Thickness

E Electric field vector

e Charge of an electron $= 1.6 \times 10^{-19}$C

H Magnetic field vector

J Electric current density

k Wave number

M Magnetisation

m Mass

P Polarisation

R Radius

S Poynting vector

$\sum$ Summation of multiple terms

t Time

Acronyms / Abbreviations

BVOH butene-diol vinyl alcohol

cLDA Complementary Longitudinal dipole Anti-bonding

cLDB Complementary Longitudinal dipole bonding

cSRR Complementary Split-ring resonator

cTDA Complementary Transverse dipole Anti-bonding

cTDB Complementary Transverse dipole bonding

DoF Depth of Focus

DPS Double positive

EFL Effective focal length

EM Electromagnetic

ENG Permittivity/ε negative

ENZ Permittivity/ε near zero

FWHM Full-width at Half-maximum

IIM Insulator-Insulator-Metal

IIMI Insulator-Insulator-Metal-Insulator

κ Extinction coefficient

LDA Longitudinal dipole Anti-bonding

LDB Longitudinal dipole bonding

LSP Localised surface plasmon

MNG Permeability/μ negative

MNZ Permeability/μ near zero

MTM Metamaterial

MTS Metasurface

n Refractive index

NNZ Near zero refractive index

PEC Perfect electric conductor

PLA Polylactic acid

PMC Perfect magnetic conductor

PNJ Photonic nanojet

rPET recycled polyethylene terephthalate

rPLA recylced Polylactic acid

SPP Surface plasmon polariton

SRR Split-ring resonator

TDA Transverse dipole Anti-bonding

TDB Transverse dipole bonding

TD Transverse dipole

TEM Transverse electromagnetic

TE Transverse electric

TM Transverse magnetic

ZIM Zero index material

Preface

This thesis represents the culmination of research conducted as part of the EPSRC DTP PhD scheme (EP/R51309X/1) at Newcastle University. The research explored in this doctoral thesis was advised, supervised and directed by Dr Victor Pacheco-Peña from Newcastle University. The scope of this doctoral work spans a wide range of electromagnetic frequencies, from millimetre waves to optical frequencies, with a primary focus on advancing the control of electromagnetic waves, particularly within the domain of plasmonics. The following chapters explain the methodologies, findings, and implications of this research:

Chapter 1 provides a comprehensive overview of traditional and modern methods for manipulating electromagnetic waves. First, traditional methods of manipulating electromagnetic waves will be discussed, such as the Babinet principle and the lens maker equation. Then, by classifying the properties of materials more modern methods will be expanded upon including a comprehensive exploration of plasmonics emphasising surface plasmon polaritons and localised surface plasmons.

In Chapter 2, dual-dielectric structures are designed to produce a bent focus. Initially, the concept of photonic nanojets is introduced. This is then expanded upon to exploit the interference of two dielectric particles to generate a focus. The scattering and diffraction properties of the particles are then calculated to design asymmetry in the two particles to produce curved focal spots. Different configurations are explored with a demonstration of the experimental viability of the structures.

Chapter 3 explores the use of a traditional technique to design lenses within the realm of surface plasmon polaritons. First, the effective media of surface plasmon polaritons is shown to determine the regions where surface plasmon polaritons will propagate and determine the desired geometries of the plasmonic lenses. The capabilities of plasmonic meniscus lenses and plasmonic convex-planar lenses are evaluated and contrasted in terms of power enhancement at the focus and their spatial resolution both along the propagation direction and transverse to it. The robustness of the plasmonic meniscus lenses is then explored introducing rotation and potential fabrication errors in the structures.

Chapter 4 discusses the other emphasis of plasmonics, exploiting complementary resonant localised surface plasmons to sense variations in a nearby dielectric. First, two complementary plasmonic nanostructures are designed using cylindrical metallic dimer particles and cylindrical dimer apertures in a metal film are designed using the Babinet principle. The complementarity of the structures is demonstrated in terms of the spectral location of the localised surface plasmon resonant modes and field distribution. These results are then corroborated using experimental data from collaborators. The complementary plasmonic structures are then exploited to detect variations of dielectric with various geometries and refractive index. The effect of different aspects on the properties of the complementary plasmonic structures is also explored.

Finally, in Chapter 5 the main conclusions established from the thesis are shown and a list of potential studies to be conducted in the near future is given.

Chapter 1

Introduction

Research aimed at improving the control and manipulation of electromagnetic (EM) waves has prompted the study of the intrinsic properties of natural materials and ways to bypass and overcome them in recent decades. Materials possess absolute values of magnetic permeability (μ) and electric permittivity (ε) at each frequency, which when compared relative (μ_r, ε_r) to free space (μ_0, ε_0) can be used to characterise their EM response. Consider common dielectrics used for microwave to optical frequency applications: they exhibit only an electric response with little to no magnetic response, so ε_r will only have values greater than one while μ_r will be approximately one, making it equivalent to a magnetic field in free space. Much of the progress in EM-related fields such as photonics and microwaves relies on these materials, forming the foundation for state-of-the-art structures in use today.

As these EM properties set the confines of possible structures due to the materials available to us, interest in surpassing these boundaries of EM properties found in nature has motivated the scientific community to find and explore new methods and media for manipulating EM waves. In recent decades, one of the ways that have been found to make this a reality has been through utilising artificial and effective media such as metamaterials (MTMs), metasurfaces (MTSs), and plasmonics. MTMs and MTSs offer much greater control over these EM properties, providing the ability to tailor the μ and ε of a medium. This can enable media to exhibit EM responses not easily found in nature, including extreme values of μ and ε, such as values approaching zero and even negative. Plasmonics, the study of EM waves coupled with conduction electrons in metals at optical frequencies, has also emerged as another field with effective media and subwavelength confinement of EM waves.

The first chapter of this thesis will provide a background and outline the core concepts of photonics, plasmonics and artificial media to put the thesis in context. This will include an exploration of classical concepts in optics and phenomena commonly employed within artificial media. Additionally, the chapter will provide a comprehensive exploration of the

field of plasmonics, detailing both localised surface plasmons (LSPs) in metallic nanoparticles and surface plasmon polaritons (SPPs) propagating at metal-dielectric interfaces.

1.1 Controlling EM waves: fundamentals

The conventional approach to controlling and manipulating EM waves relies on natural materials to guide and shape them [2]. The EM properties of these media are determined by the atoms, molecules, and interactions, such as molecular vibrations [3], within the material. These materials interact with external electromagnetic fields, with the extent of this interaction quantified by the complex values of the absolute permittivity (ε) and permeability (μ) of a medium, respectively. A relative value (μ_r, ε_r) for each medium is then derived by comparing it to free space. An example of this concept can be seen in Fig. 1.1 where a schematic representation of the atomic structure of a material is shown.

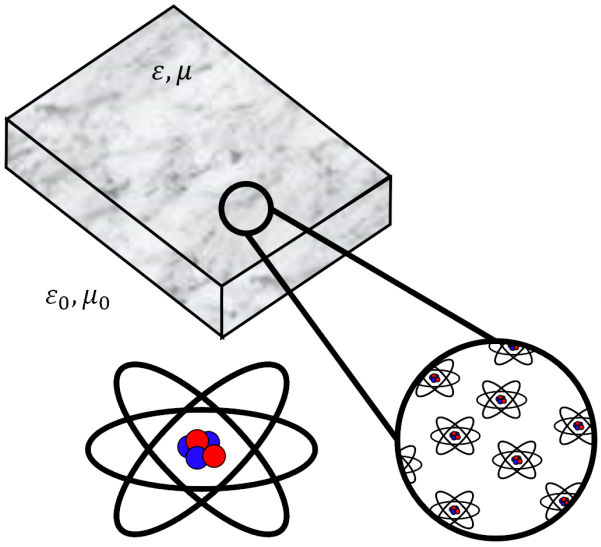

Fig. 1.1 Schematic representation of a natural material which has EM properties defined by the atomic structure

Materials, such as dielectrics like glass or quartz, are shaped and tailored to fulfil specific functions. For example, they can be crafted into lenses that can focus light, finding applications in optical telescopes for star gazing [4, 5], or in microscopes which led to the observation of bacteria and protists [6], among other applications. Therefore, given the significant potential in many diverse areas, increasing the understanding of the EM properties

of materials and improving our ability to control EM waves has been a focal point of intense research for centuries.

1.1.1 Maxwell equations

Understanding the response of EM waves within natural media serves as the foundation of many modern communication and information technologies. Since the late 1700s, extensive work has been conducted to comprehend these EM interactions. These efforts culminated in the development of a summary set of equations describing the fundamental principles governing the behaviour of EM waves. The macroscopic Maxwell's equations have since become the core of classical EM. This set of equations in their differential form, are shown here [7]:

$$\nabla \times \mathbf{E} + \frac{\partial \mathbf{B}}{\partial t} = 0 \tag{1.1}$$

$$\nabla \times \mathbf{H} - \frac{\partial \mathbf{D}}{\partial t} = \mathbf{J} \tag{1.2}$$

$$\nabla \cdot \mathbf{B} = 0 \tag{1.3}$$

$$\nabla \cdot \mathbf{D} = \rho \tag{1.4}$$

where **E** and **H** represent the electric field and magnetic field vectors, respectively, **B** denotes the magnetic field density, **D** is the electric field displacement and ρ and **J** are the electric charge and current densities, respectively. Eq. (1.1), known as the Maxwell-Faraday equation, states that the existence of a time-varying magnetic field necessitates the coexistence of a spatially- and time-varying electric field. Eq. (1.2), or the Ampere-Maxwell equation, states that if an electric current and electric field vary in time, a circulating magnetic field will be produced. Eq. (1.3), Gauss' law of magnetism, establishes that a magnetic field does not diverge at any point, giving the concept that there are no magnetic monopoles. Finally, Gauss' law, Eq. (1.4), relates the distribution of the resulting electric field from an electric charge, diverging from a positive charge while converging on a negative charge.

When an external electric or magnetic field source is introduced and acts on a medium, then it transforms the medium into a new vector source in the form of polarisation density, **P**, and magnetisation **M**. Polarisation density, shown in Eq. (1.5), expresses the electric dipole moment per unit volume within a material, while, the magnetisation, shown in Eq. (1.6),

represents the magnetic dipole moment per unit volume of a material.

$$\mathbf{P} = \varepsilon_0 \chi_e \mathbf{E} \tag{1.5}$$

$$\mathbf{M} = \mu_0 \chi_m \mathbf{H} \tag{1.6}$$

where $\varepsilon_0 = 8.854 \times 10^{-12}$ F/m and $\mu_0 = 4\pi \times 10^{-7}$ H/m are the absolute values of the permittivity and permeability of free space, respectively, and χ_e and χ_m represent the electric and magnetic susceptibility of a medium, respectively. If the medium is linear [8], as will be the case of materials used in this thesis, the magnetic and electric susceptibility of a medium are related to the relative permeability and permittivity by $\mu_r = \chi_m + 1$ and $\varepsilon_r = \chi_e + 1$. These can then be used to define **D** and **B** from Eq. (1.1)–(1.4) as follows [9]:

$$\mathbf{D} = \varepsilon_0 \mathbf{E} + \mathbf{P} = \varepsilon_0 \varepsilon_r \mathbf{E} \tag{1.7}$$

$$\mathbf{B} = \mu_0 \mathbf{H} + \mathbf{M} = \mu_0 \mu_r \mathbf{H} \tag{1.8}$$

with ε_r and μ_r denoting the respective relative permittivity and permeability of the linear medium. The values of these EM properties are dependent on several parameters, including the operational wavelength, considering the dispersive nature of materials [10, 11], and the orientation of the medium with regards to the incident field [12, 13].

Another important EM property of a medium is the complex refractive index ($\tilde{n}$), which describes the properties of a propagating wave within a medium [14]:

$$\tilde{n} = n + i\kappa = \sqrt{\varepsilon_r \mu_r} \tag{1.9}$$

where $\tilde{n}$ is the complex refractive index with the real and the complex component, known as the extinction coefficient, represented by n and κ, respectively. n represents the ratio by which the phase velocity [15] of an incident EM wave changes compared to propagating in free space. On the other hand, κ describes the spatial decay of the EM wave as it propagates through the medium. Collectively, these parameters contribute to a thorough comprehension of the behaviour of EM waves within a specified medium.

1.1.2 Classical concepts

Section 1.1.1 introduces the cornerstones of classical physics that have been exploited to develop methods to control and manipulate EM waves across a broad spectrum of wavelengths, from microwaves [16, 17] and millimetre waves [18, 19] down to optical wavelengths [20–22]. The following sections will introduce applications of these concepts and principles.

Snell's law

Snell's law, stated by Willebrørd Snell his 1621 manuscript [23, 24], describes the relationship between the angle of incident illumination at a boundary of two regions, each with a different refractive index, to calculate the angle of refraction within the second region [25]:

$$n_1 \sin(\theta_1) = n_2 \sin(\theta_2) \tag{1.10}$$

where n_1 and n_2 represent the refractive index of two adjoined media, θ_1 is the incident angle if an incident EM wave, and θ_2 is the refraction angle. Consider two regions with a boundary where they meet; region 1 has a refractive index of n_1 and region 2 has a refractive index of n_2. A wave propagates through region 1 towards the boundary with an incident angle θ_1 compared to the normal of the boundary. Upon crossing the boundary into the region with a different refractive index, the wave refracts with angle θ_2. This is represented schematically in Fig. 1.2. Snell's law is fundamental in various fields such as acoustics and EM, among others. It holds significant importance in designing many different applications such as acoustic ultrasound [26], optical lenses [25], and optical fibres through achieving total internal reflection [27].

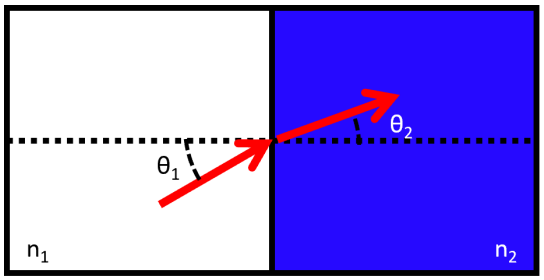

Fig. 1.2 Schematic representation of Snell's law of an EM wave propagating from one medium to another.

Lens maker equation

By applying Snell's law with the ray tracing principles of geometric optics (explored in detail in Appendix A) [28, 29], additional equations and formulas can be derived to design refractive elements for applications in more specialised settings. An example of this application is in the design and research of lenses to shape EM waves, an area of interest dating back to ancient times, even with manuscripts detailing *burning lens* shapes [30, 31]. Refractive elements, such as lenses, are considered transparent structures that alter the direction of propagation of an incident EM wave through refraction according to Snell's law [25]. The

changes in wave propagation will depend on the shape and EM properties of the refractive element and the surrounding media.

One way to categorise traditional lenses is based on whether a set of parallel rays, such as a plane wave, converge or appear to diverge after they have propagated through the lens [14, 28]. A converging lens causes a set of parallel rays to converge at a point known as a focus [32], an example shown in Fig. 1.3a. On the contrary, a diverging lens demonstrates the opposite behaviour, dispersing parallel rays as they traverse the lens, leading to the formation of a virtual image, with an example shown in Fig. 1.3b [32].

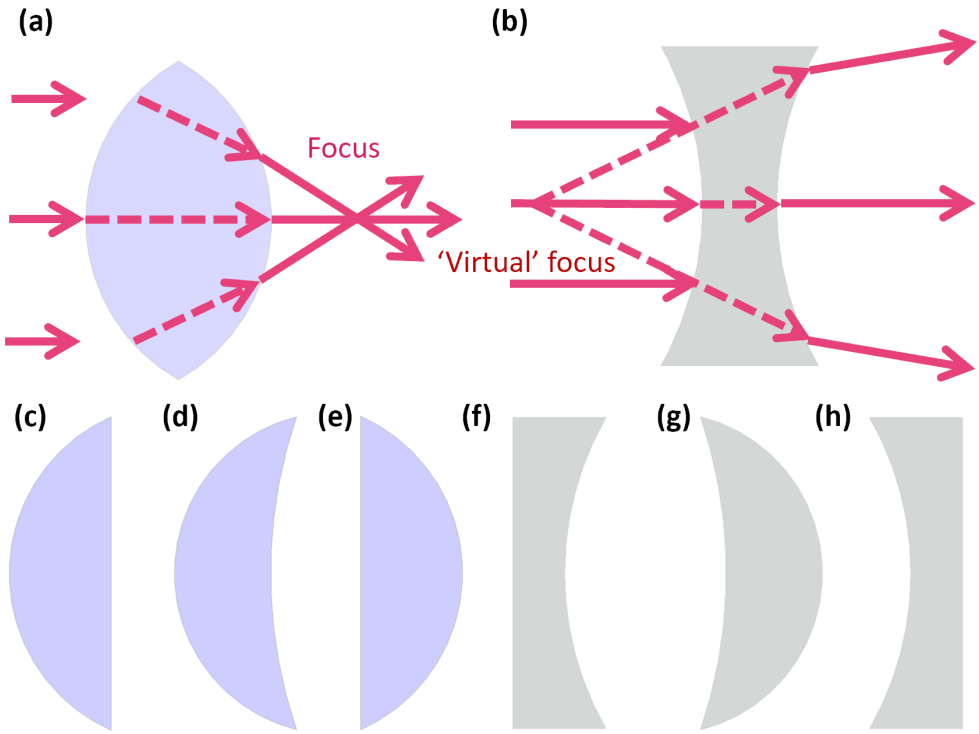

Fig. 1.3 Ray tracing schematic representations of (a) a double-convex lens and (b) a double-concave lens. Examples of (c) a convex-planar lens, (d) a positive meniscus lens, (e) a planar-convex lens, (f) a planar-concave lens, (g) a negative meniscus lens and (h) a concave-planar lens.

The different profiles of the lenses shown in Fig. 1.3 can be designed using methods such as the equation of a conical section to design lenses with a planar face [18]. However, one of the most versatile and straightforward approaches to lens design, employed since the 1600s [30] is the *lens maker equation*. This equation is schematically represented in Fig. 1.4a and mathematically defined as follows:

$$\frac{1}{EFL} = (\phi - 1)\left(\frac{1}{R_1} - \frac{1}{R_2} + \frac{(\phi - 1)d}{\mathbb{R}e(n_2)R_1R_2}\right) \tag{1.11}$$

where EFL denotes the effective focal length, $\phi = \frac{n_2}{n_1}$ represents the ratio between the n of the lens (n_2) and the surrounding medium (n_1), R_1 and R_2 denote the radii of curvature of the input and output surfaces of the lens, respectively, and d stands for the thickness of the lens along the direction of propagation at the middle of the lens. Simplified versions of the *lens maker equation* exist when criteria are met. If the lens is in free space $n_1 = 1$ then $\phi = n_2$ and for cases where $t < |R_1|, |R_2|, |R_1 - R_2|$;and the lenses can be considered as *thin*, the term $\frac{(\phi-1)t}{n_2 R_1 R_2} \to 0$. The derivation of this equation is shown in Appendix A.

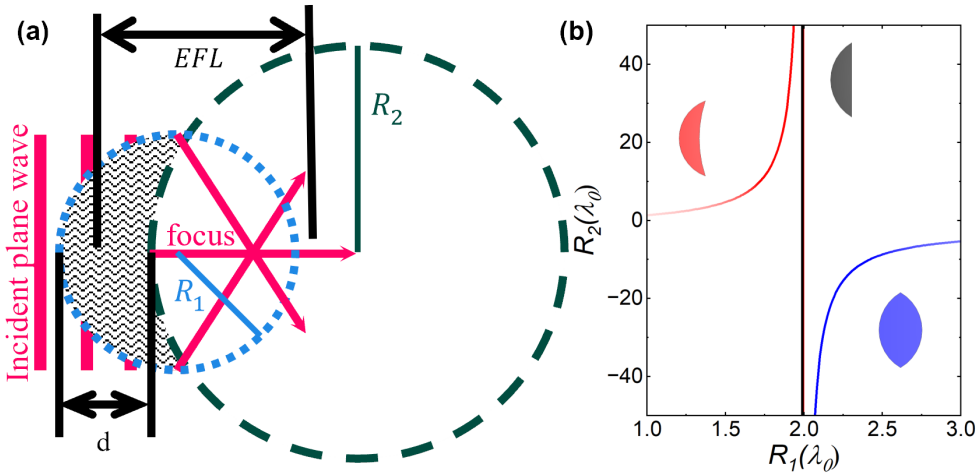

Fig. 1.4 (a) Schematic representation of the *lens maker equation*, where R_1 and R_2 represent the radii of curvature of the input (left) and output (right) surfaces of the lens, respectively, d is the thickness at the middle of the lens, and EFL is the effective focal length. (b) Value of R_2 from the *lens maker equation* considering $\lambda_0 = 1.55\,\mu$m, $n_1 = 1$, $n_2 = 2$, $d = 1\,\mu$m, and $EFL = 2\lambda_0$. Insets are included showing the three lens types, double-convex (blue), convex-planar (black) and positive meniscus (red) when n_2 is varied.

The *lens maker equation* facilitates the creation of both converging ($EFL > 0$), shown in Fig. 1.3a,c-d, and diverging lenses ($EFL < 0$), shown in Fig. 1.3b,f-h, by determining the sign convention of the radii of curvature (R) of the input (R_1) and output faces (R_2). If $R > 0$, the centre of the curvature is on the same side as the incident EM wave, whereas $R < 0$ indicates the opposite. To design a converging lens, $R_1 > 0$, and then the radius of the output face will determine the type of converging lens. If $R_2 < 0$, double convex is produced, shown in Fig. 1.3a; if $R_2 \to |\infty|$, then a convex planar lens is produced, shown in Fig. 1.3c, and if $R_2 > 0$ then a positive meniscus is obtained, shown in Fig. 1.3b. Diverging lenses can be designed when $R_1 < 0$, and then if $R_2 > 0$ is a double concave lens, shown in Fig. 1.3d, $R_2 \to |\infty|$ then a concave planar lens is produced, shown in Fig. 1.3f, and $R_2 < 0$ is a negative meniscus lens shown in Fig. 1.3e.

In a scenario for a converging lens with $n_1 = 1$, $n_2 = 2$, $d = 1\,\mu m$, and $EFL = 2\lambda_0$, the effect of R_1 on R_2 can be observed in Fig. 1.4b. Three regions are observed for these parameters: when $R_1 \lessapprox 1.95$, R_2 will be positive (red) with similar magnitude as R_1, producing a positive meniscus lens; if $R_1 \gtrapprox 2.05$, will be negative (blue) with a similar magnitude as R_1, resulting in a double convex lens. Finally, if R_1 is between these values, $R_2 \gg R_1$, and the profile will be a convex planar lens. Although the *lens maker equation* has been exploited in different frequency regimes, such as meniscus lenses in the microwave regime [33] and optical frequencies for telescopes, it has not yet been explored in the realm of plasmonics. In this thesis, the *lens maker equation* will be adapted for SPPs to engineer plasmonic meniscus lenses [34] capable of producing a sub-wavelength focus.

Babinet's principle

Another concept that has been proven useful for the design of EM structures is Babinet's principle. Originally, Babinet expressed this principle in the context of the Huygens-Fresnel propagation principle without providing a mathematical proof [35, 36]. Babinet's principle was formally formulated for EM using perfect electric and magnetic conductors (PEC and PMC, respectively) [37].

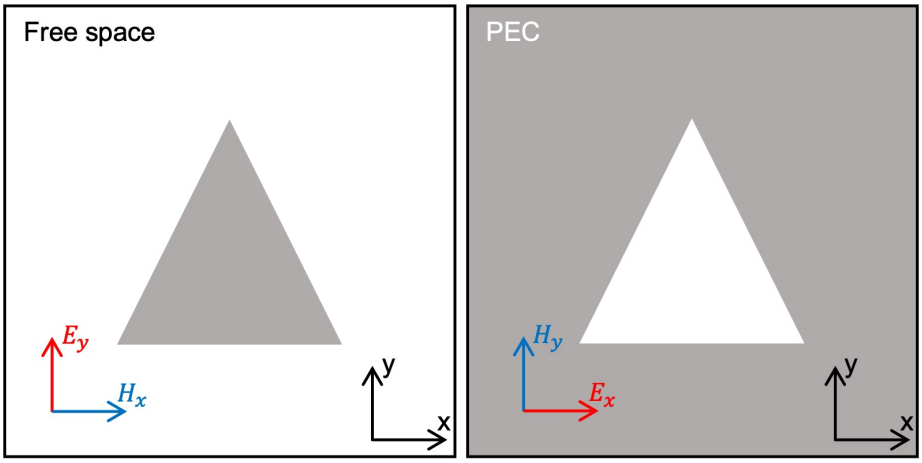

Fig. 1.5 Schematic representation of two equivalent antennas due to Babinet's principle with (left) an antenna from a perfectly conducting strip and (right) a slot in a perfectly conducting screen, with an infinitely thin thickness

An example of the principle in EM is shown in Fig. 1.5, where orthogonally polarised, complementary plane waves are incident on an infinitely thin PEC particle (left), depicted here as a triangle, and a complementary aperture in an infinitely thin screen of PEC (right) . Both scenarios in Fig. 1.5 yield the same diffraction pattern. Therefore, solving one of the cases for either the electric or magnetic fields means the other is solved with minimal

additional effort. This property significantly facilitates the simplification of complicated EM problems, enabling the design and evaluation of complex structures with reduced computational requirements. This proves highly beneficial in addressing challenging problems effectively.

Babinet's Principle has found applications in many frequency regimes, primarily within microwaves for antenna design [38], but has also been used for metamaterials and nanophotonics [39]. Recent efforts have been made to verify the validity of the Babinet principle in plasmonics [40–42]. This has opened the possibility of new ways to exploit plasmonics in diverse applications, some of which will be explored later in this thesis where complementary plasmonic structures are used to sense changes of a nearby dielectric [43].

1.2 Metamaterials and effective media – manipulating light at will

Recently, a new area of research has emerged, focused on developing artificial media, diverging from the classical concepts explored in the previous section. Artificial media refers to materials and structures that are designed, tailored and constructed to exhibit EM responses (permittivity, permeability and refractive index) which are not easily achievable in nature.

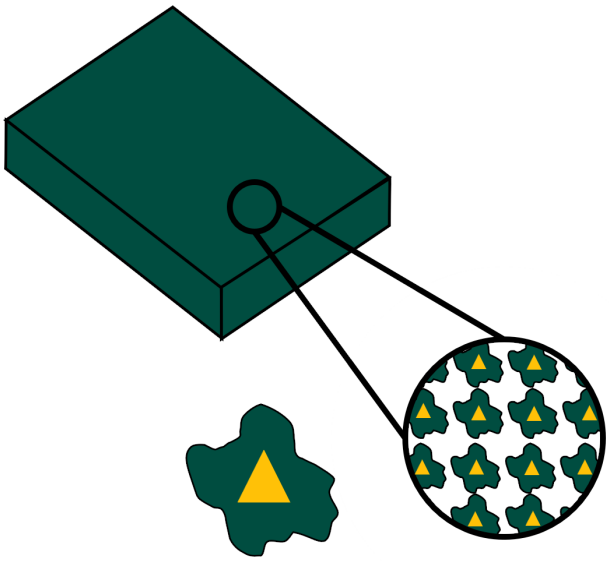

Fig. 1.6 Schematic representation of a metamaterial which has EM properties defined by its sub-wavelength unit cells.

Winston E. Kock initially conceived the concept of an artificial dielectric in the 1940s when he designed metal lenses using conducting plates for antenna applications for radio waves [44]. Then, Veselago postulated in 1968 that a material could exhibit negative refractive index when both ε and μ were negative simultaneously (using $n = \varepsilon_r = \mu_r = -1 = \exp(i\pi)$) [45]. In natural media ($n > 0$), the direction of the phase velocity and the power/Poynting vector are parallel, making it a *right-handed* material. However, in materials with negative refractive index ($n < 0$), the phase velocity is anti-parallel to the Poynting vector and is classified as a *left-handed* material. The realisation of a negative refractive index material was achieved experimentally around the turn of the millennium by artificial media utilising a wire medium and split-ring resonators (SRRs) [46].

Artificial media with controllable parameters that offer responses rarely found in nature are given the umbrella term *Metamaterials* (MTMs). The Greek prefix "*meta*" meaning beyond, signifies that these materials have properties beyond anything observed in nature [47]. MTMs often consist of lattices made up of unit cells that are notably smaller than the operational wavelength [48–50]. When an EM wave interacts with the MTM, it behaves as an effectively homogeneous macroscopic material rather than the array it is made of, producing an effective medium with effective properties such as effective permeability (μ_{eff}) and permittivity (ε_{eff}).

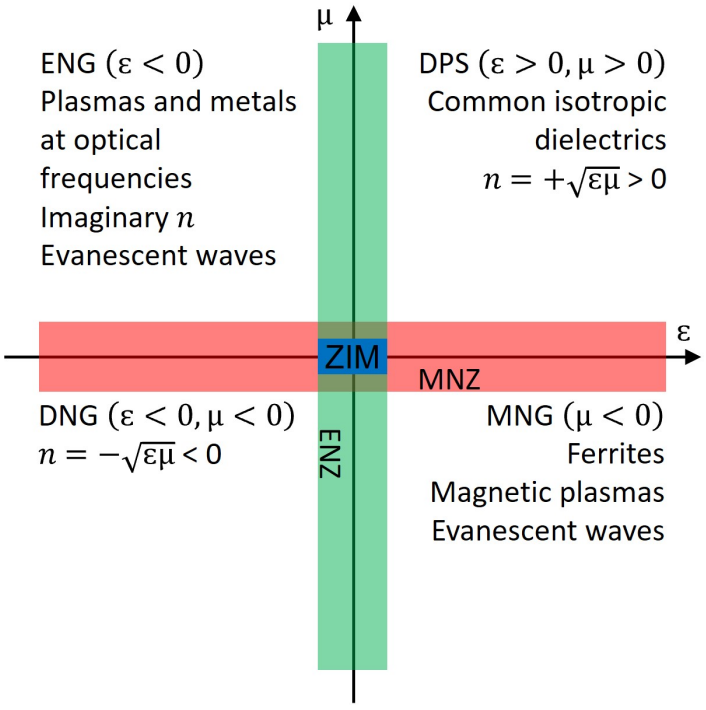

Fig. 1.7 Material classification depending on the relative permittivity and permeability.

The EM parameters of ε and μ can be used to classify materials into distinct categories depending on the sign of the relative parameters [51], shown in Fig. 1.7. These categories include double-positive (DPS) materials on the top right, negative permeability (MNG) on the bottom right, double-negative (DNG) on the bottom left, and finally negative permittivity on the top left (ENG). Additionally, there are interesting sub-classes of materials when the μ and/or the ε approach zero, resulting in permeability-near-zero (MNZ), permittivity-near-zero (ENZ), or refractive index near-zero/zero-index materials (NNZ/ZIM). Each of these classifications has its special properties which will be explored in the next sections.

1.2.1 Double Positive/Negative

DPS materials, located in the top right corner of Fig. 1.7 possess real values of absolute ε, μ that are greater than zero. Therefore, according to Eq. (1.9), they will have a positive refractive index that is often greater than the refractive index of free space (i.e. $n > 1$). This quadrant describes the majority of materials observed in nature, such as dielectrics at optical frequencies like glass, as discussed previously in Section 1.1.1. As stated earlier these materials will be *right-handed*.

On the contrary, DNG materials have values of ε, μ that are less than zero, resulting in a negative refractive index, as intially predicted by Veselago. This property makes the phase velocity anti-parallel to the Poynting vector, classifying it as a *left-handed* material, as mentioned before [45, 52]. Since its discovery, this concept has been exploited in several ways including the production of antennas [53] and the development of so-called perfect lenses, only limited by losses [54].

1.2.2 Single Negative (SNG) Materials

The top left and bottom right of Fig. 1.7 represent the cases where the materials are ENG and MNG, respectively. MNG materials support evanescent waves and are indicative of magnetic plasma, a phenomenon which is often only observed for ferromagnetic materials near their resonant wavelength [55–57]. ENG media represent electric plasma and can support evanescent waves, such as surface plasmons on metals at optical wavelengths, a topic which will be discussed in greater detail in Section 1.4.1 and 1.4.2. These media have also been realised in microwave, THz, IR, and visible frequency domains [48, 58].

1.2.3 Near Zero Materials

There is a special subset of materials where either the permeability $\mu \approx 0$ (MNZ), permittivity $\varepsilon \approx 0$ (ENZ) or both $\varepsilon \approx \mu \approx 0$ (ZIM) are close to zero [59–61]. This near-zero effective media has some interesting implications as an EM field within it will appear static in space with an effective propagation constant close to zero and, thus, an almost infinite effective wavelength i.e. approximately zero phase change inside the material. Natural materials, such as metals like gold and silver just above their plasma frequency, can exhibit a refractive index near zero properties. In the case of ZIM materials, when a source is embedded in them, rays will refract by a small angle as they leave the slab due to Eq. (1.10), thus travelling almost perpendicular from the surface [61].

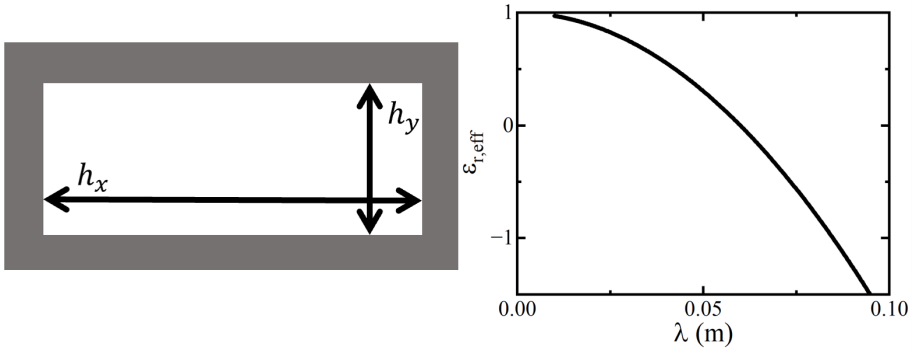

Fig. 1.8 Schematic representation of a cross-section of a hollow rectangular waveguide and the relative effective permittivity of a hollow waveguide with dimensions $h_x = 0.03$ m and $h_x = 0.015$ m.

Several methods have been demonstrated to realise the near-zero conditions of ZIM materials. These methods include photonic crystals [62], doped semiconductors [63] and plasmonics [64]. MTMs have also been shown to be effective at producing near-zero media, including multilayer media[65]. Another approach to creating an MTM that emulates ENZ conditions involves using the dispersive nature of hollow rectangular waveguides. The relative effective permittivity of a hollow rectangular waveguide ($\varepsilon_{r,\mathrm{eff}}$) can be defined as follows (assuming the media is non-magnetic, i.e. $\mu_{r,0} = 1$) [66]:

$$\varepsilon_{r,\mathrm{eff}} = \varepsilon_{r,\mathrm{fill}} - \frac{\lambda^2}{4h_x^2} \tag{1.12}$$

where $\varepsilon_{r,\mathrm{fill}}$ denotes the relative permittivity of the dielectric that fills the waveguide (typically air, $\varepsilon_{r,\mathrm{fill}} = 1$), λ represents the operational wavelength, and h_x is the widest transversal width of the waveguide which determines the cut-off wavelength ($\lambda_c = 2h_x$) of the waveguide. Therefore, if the operational wavelength is chosen to be very close to the cut-off wavelength

($\lambda \approx \lambda_c$), then $\varepsilon_{r,\text{eff}} \approx 0$, and the waveguide operates as an ENZ material. However, challenges arise due to the almost infinite impedance that occurs due to $\varepsilon_{r,\text{eff}} \approx 0$, resulting in significant impedance mismatches that need to be overcome, a topic that will be explored briefly in this thesis in Appendix B [67, 68].

1.3 Photonics

The emergence of quantum mechanics [69], has led to revolutionary inventions, including the laser (light amplification by stimulated emission of radiation) significantly expanding the capability of researchers to generate, control, and detect EM waves in the form of photons [70]. The realm of photonics spans across the near-infrared to visible wavelength ranges (750 nm - 2500 nm and 380 nm - 750 nm, respectively). In these wavelength ranges, photonics has found applications in diverse fields, such as biomedicine [71, 72] and photovoltaics [73].

Photonics has particularly excelled in long-distance telecommunications using optical fibres [74] and information processing [75], due to its high data-carrying capacities [76]. This challenges the traditional dominance of electrons - a necessary step due to the limitations imposed by the carrier speeds of electrons and the high power dissipation of electronic components, hindering further miniaturisation of transistor technology. Photonics applications are predominantly based on materials like silicon. However, the search for alternative materials is ongoing, with a brief study of polymers discussed in Appendix C.

1.3.1 EM material models

In EM work, knowledge of the ε and μ for materials of materials is crucial, as explored in Section 1.1.2. However, modelling the EM response of some materials, such as metals at optical wavelengths, can be challenging due to the quantum mechanical nature of electrons. To address this, a common approach for modelling the dispersive behaviour of metals when subjected to an external EM field is the Drude model [77, 78].

The Drude model considers the medium as an array of stationary positively charged ions surrounded by free-to-move electrons, taking into account intra-band transitions [79, 80]. The assumption is there are no interactions between electrons and other electrons or the ions, except for collisions (instantaneous and perfectly elastic) between the electrons and the ions, known as the independent electron approximation [81]. The electrons and ions share a density of ions/electrons per unit volume n_e, while the electrons have a mass and charge of m and e, respectively. Using this model, a complex relative permittivity ε_r of the medium can be calculated using relations between $\mathbf{J}$ and $\mathbf{E}$ [80]:

$$\varepsilon_r = \varepsilon_\infty + \frac{\omega_p^2}{\omega(i\gamma - \omega)} \tag{1.13}$$

where ε_∞ is the permittivity of the material at infinite frequency, $\omega_p = \sqrt{\frac{n_e e^2}{\varepsilon_0 m}}$ is the plasma frequency when the material's permittivity is zero, γ is the collision frequency, and ω is the operational frequency. Combining this with the Lorentz model, which incorporates multiple resonant wavelengths and intraband electron transitions [82], resulting in an improved expression for the complex relative permittivity known as the Drude-Lorentz model as:

$$\varepsilon_r = \varepsilon_\infty + \frac{\omega_p^2}{\omega(i\gamma - \omega)} - \sum_{m=1}^{N} \frac{\varepsilon_{l(m)}\omega_{l(m)}^2}{\omega_{l(m)}^2 - \omega^2 - 2\omega i\gamma_{l(m)}} \tag{1.14}$$

where γ_l, ω_l, and ε_l, are the collision frequency, plasma frequency, and permittivity of the Lorentz model, respectively. $m = 1, 2, \ldots, N$ is an integer value which represents the contribution of Lorentzian oscillations. The Drude-Lorentz model is shown for gold (Au) and silver (Ag) compared to the experimental data from [1] in Fig. 1.9. The parameters used for the Drude-Lorentz model of gold and silver are shown in Table 1.1.

Table 1.1 Parameters of Au and Ag for the Drude-Lorentz model.

Drude-Lorentz parameters		
	Au	Ag
ε_∞	9.1	1.174
$\omega_p\ (rads^{-1})$	1.3799×10^{16}	1.36973×10^{16}
$\gamma_d\ (rads^{-1})$	6.116×10^{13}	3.058×10^{13}
ε_l	3.2	1.69
$\omega_l\ (rads^{-1})$	6.91115×10^{15}	7.5398×10^{15}
$\gamma_l\ (rads^{-1})$	1.900×10^{15}	1.839×10^{15}

1.4 Plasmonics

The study of photonics and the behaviour of light at nanometer scales, nanophotonics, has expanded a research area in recent decades, offering more compact manipulation and control of EM waves, among other benefits [83]. Plasmonics has emerged as a sub-field of nanophotonics, which encompasses two important aspects: localised surface plasmons (LSPs) and surface plasmon polaritons (SPPs). Plasmonics exploits the response of metals

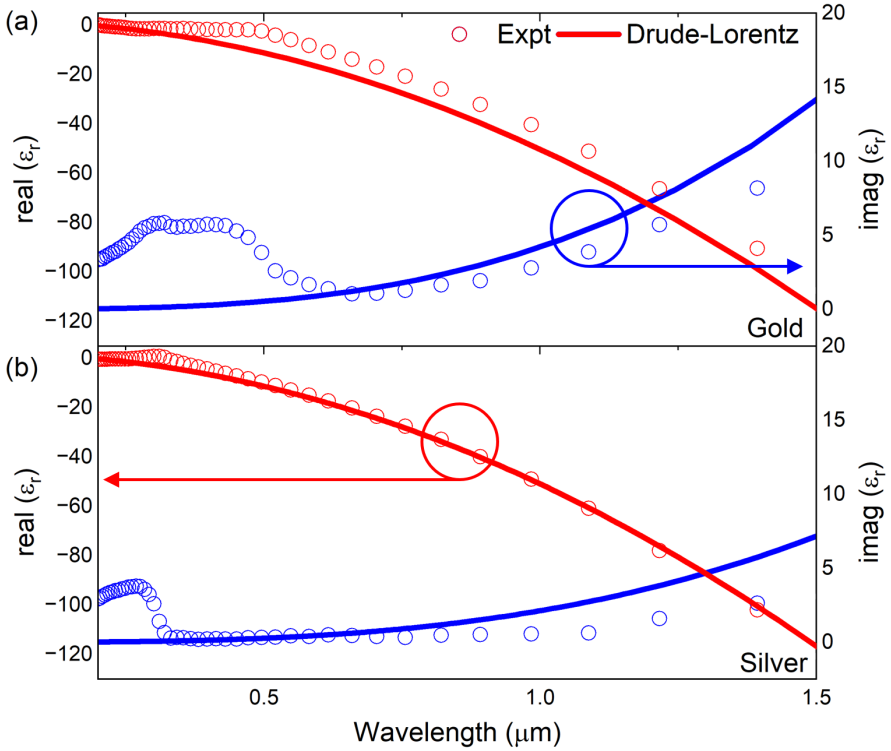

Fig. 1.9 Real (red) and imaginary (blue) values of the relative permittivity (ε_r) of (a) Au and (b) Ag using the Drude-Lorentz model (curve) and experimentally retrieved data from the work of Johnson and Christy [1] (circles)

at optical wavelengths, where they behave as dispersive media that can be modelled using the approaches in Section 1.3.1. When modelling metals this way, an incident EM wave can couple with the free conductive electrons in metallic nanoparticles and metallic films inducing collective, coherent oscillations of the electrons [84, 85]. Plasmonics offers a combination of the data-carrying capacity of photonics with the compactness of electronics, by effectively working at nanometer scales [86, 84].

1.4.1 LSPs

LSPs are non-propagating excitations of conduction electrons in metallic nanoparticles which are observed when they couple with an oscillating EM wave, as seen in Fig. 1.10. LSP modes naturally occur due to the scattering of a conductive sub-wavelength particle [87, 88] and have been studied since the 1850s by Faraday [89]. Resonances of LSPs arise when the coupled, driven electrons have an effective restoring force upon them by the surface of the particle [90]. This leads to high concentrations of the EM field in the near-field outside the particle and with the particles themselves. The frequency resonance where the LSP resonance occurs is determined by the geometric size and shape of the nanoparticles [91, 92] as well as the metal and surrounding dielectric [93, 94]. The resonances of gold and silver particles will often occur at visible frequencies of the EM spectrum, which the Romans exploited to stain glass, creating the Lycurgus Cup [95]. LSPs have since proven effective in a wide range of applications such as biosensors for chemical and bio-molecules [96], spectroscopy, sensing [97], lithography [98], and photo-thermal cancer therapies [99].

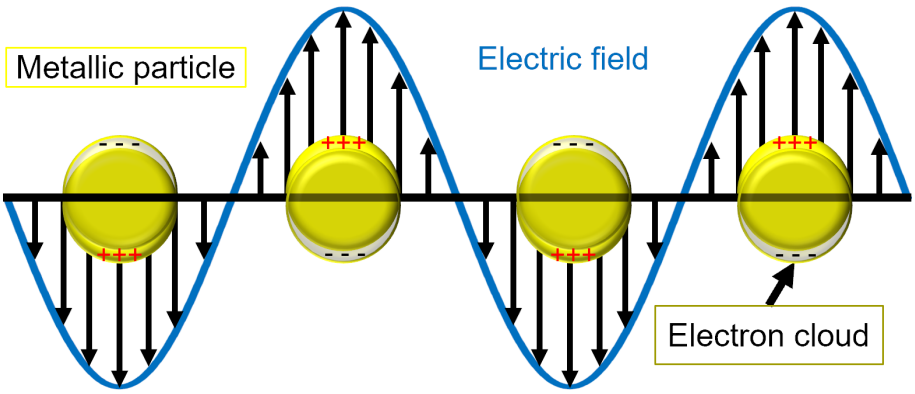

Fig. 1.10 Schematic representation of a LSP caused by EM wave incident on a metallic nanoparticle.

To achieve high field concentrations with LSPs different configurations such as spherical metallic nanoparticles and bowtie nanoantennas [100] can be employed. An example of an

Au bowtie antenna illuminated by an E_x polarised plane wave can be seen in Fig. 1.11. Strong field confinement can be observed at the apex of their geometry, providing a broadband high-field enhancement [101]. As observed in Fig. 1.11, the absorption (blue line) is highest at a wavelength of 657 nm, where a LSP resonance has formed in the bowtie nanoantenna. A slight deviation between the reflection (R, black), transmission (T, red) and (A, blue) is a result of near- and far-field effects [102–104]. Recent investigations into new methods to achieve LSP resonances. This includes exploiting Babinet's principle to interchange the plasmonic particles with metallic films [41], a topic that will be explored further in this Thesis.

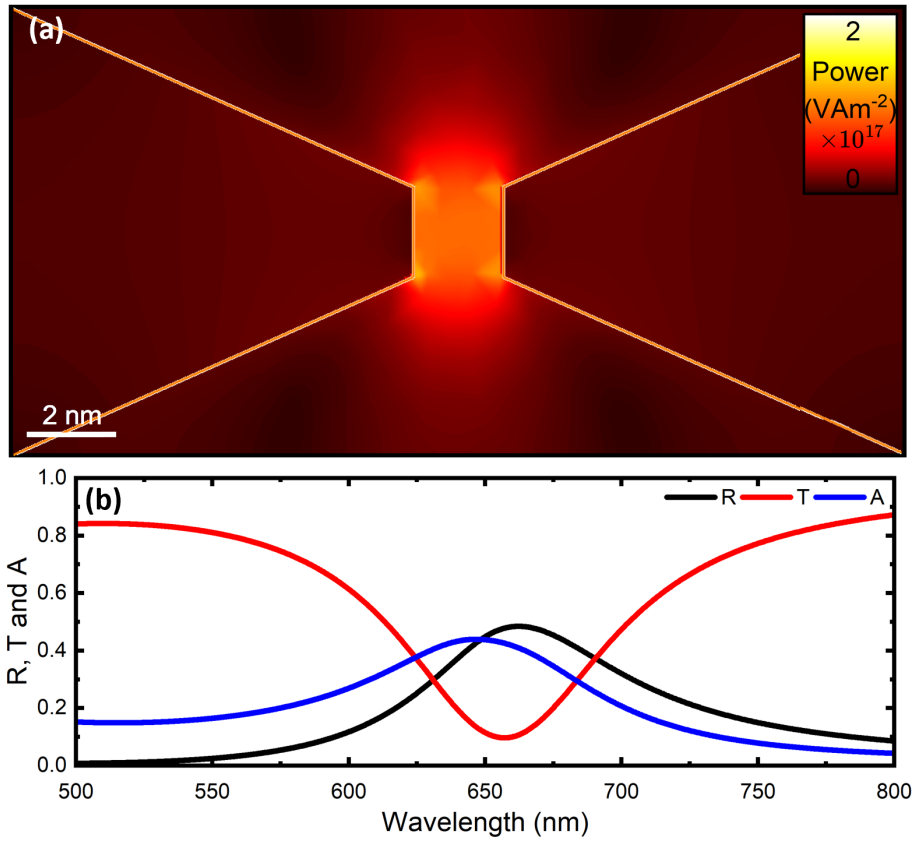

Fig. 1.11 (a) Power distribution of a gold bowtie antenna with an arm length of 9.85 nm separated by 2nm in free space at the resonant wavelength $\lambda = 657$ nm (b) The reflection (R) (black), transmission (T) (red) and absorption (A) for the bowtie antenna showing the significantly reduced T and increased A at the wavelength $\lambda = 657$ nm demonstrating the presence of a LSP resonance.

1.4.2 SPPs

SPPs are EM excitations that propagate at the boundary between a conductor and a dielectric [84, 86] confined evanescently to this boundary in the perpendicular direction. SPPs arise due to the dispersive nature of metals at optical wavelengths, allowing EM fields to slightly penetrate the metals and couple with the electron plasma of the conductor [105, 106]. Surface waves have been studied since Sommerfeld [107], and then Zenneck [108] described radio waves propagating as surface waves on a conductor of finite conductivity. Later, Fano [109] and Ritchie associated losses with interactions of electron beam diffraction at thin metallic films to surface plasmon resonances [110, 111]. The phenomena of SPPs were fully established by Kretschmann and Raether, who used prism couplings of visible light to excite Sommerfeld's surface waves on the boundary of metals and dielectrics [112].

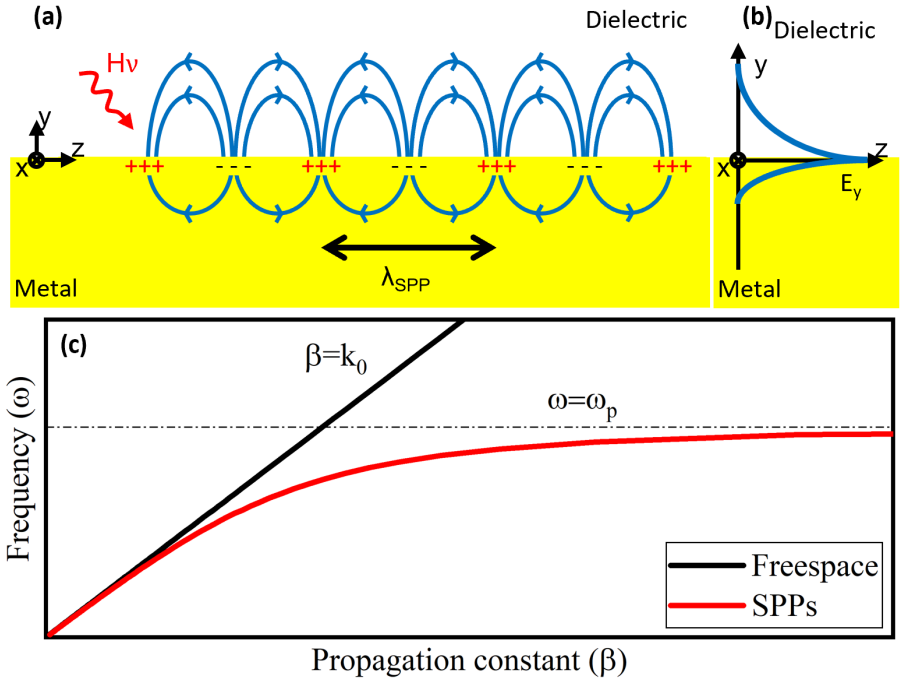

Fig. 1.12 Schematic representation of SPPs in a metal-dielectric system where the yellow is metal (b) Amplitude of the electric field penetration into the dielectric and metal for SPPs (c) Dispersion relation as a function of angular frequency for SPPs.

SPPs are transverse magnetic (TM) waves. if a SPP is considered to be propagating in the z-direction, then $H_x \neq 0$, $E_y \neq 0$, $E_z \neq 0$, and $E_x = H_y = H_z = 0$. A comprehensive exploration of the TM and TE properties of SPPs is detailed in Appendix D. A schematic representation of SPPs in the simplest configuration is shown in Fig. 1.12a, where a semi-infinite metal and a semi-infinite dielectric are shown with the electric field of the SPPs propagating along the

interface of the two materials. Fig. 1.12b shows the evanescent penetration of the electric field into the metal and the dielectric, with the E_y field component shown to decay exponentially into both the dielectric and the metal, although the field component decays significantly quicker into the metal [85]. The dispersion and propagation constant in the direction of propagation (β) of the SPPs in this configuration can be calculated by applying Maxwell's equations to derive the required wave equation and applying boundary conditions. Through these calculations, the dispersion relation of SPPs is found to be [113]:

$$\beta = k_0 \sqrt{\frac{\varepsilon_m \varepsilon_d}{\varepsilon_m + \varepsilon_d}} = k_0 n_{\text{eff}} \tag{1.15}$$

where k_0 is the wave vector of a wave in vacuum, $\varepsilon_{m,d}$ are the permittivity of the metal and dielectric, respectively. The dispersion relation when solving Eq. (1.15) using Au for the metal and air as the dielectric, is shown in Fig. 1.12, where two regions can be observed. At lower values of ω, the propagation constant is close to the light line ($\beta \approx k_z$ where $k = \frac{\omega}{c}$). As the frequency increases, β becomes greater than k. This condition of $\beta > k$ means that to excite SPPs, the incident wave cannot be oblique to the surface of the conductor and excite SPPs as the momentum of the photons incident on the surface will always have a value smaller than β. Several methods have been developed to excite SPPs on metal-dielectric interfaces [84, 114]. One way to overcome the mismatch between the in-plane momentum of the photons ($k_z = ksin\theta$) and β is to use a grating of holes or grooves in a metal with a lattice constant, a. For a 1D grating, shown in Fig. 1.13a, there will be phase-matching allowing SPPs whenever the following is fulfilled [113]:

$$\beta = ksin\theta \pm mg \tag{1.16}$$

where $g = \frac{2\pi}{a}$ is the reciprocal vector of the metallic grating and $m = 1, 2, 3...$ is an integer. Another common method to excite SPPs is to use a three-layer system with two dielectrics with different ε sandwiching a thin metal film, known as an insulator-metal-insulator (IMI) configuration. If the first dielectric is considered to be free space ($\varepsilon_1 = \varepsilon_0$) and the second has $\varepsilon_2 > \varepsilon_0$, SPPs can be excited at the interface between the metal and the first dielectric. This is because a beam reflected at the interface between the metal and the second dielectric will have an in-plane momentum of $k_z = k\sqrt{\varepsilon}sin\theta$, allowing phase-matching. Typically a prism will be used for the second dielectric, as shown in Fig. 1.13b.

Once SPPs have been excited and propagate along the dielectric-metal interface, they need to be controlled and manipulated as desired. This can be done by shaping the metal such as with grooves cut in the metal to produce channel plasmons [115]. However, another way to control SPPs is to exploit the concept of effective media. By introducing a second

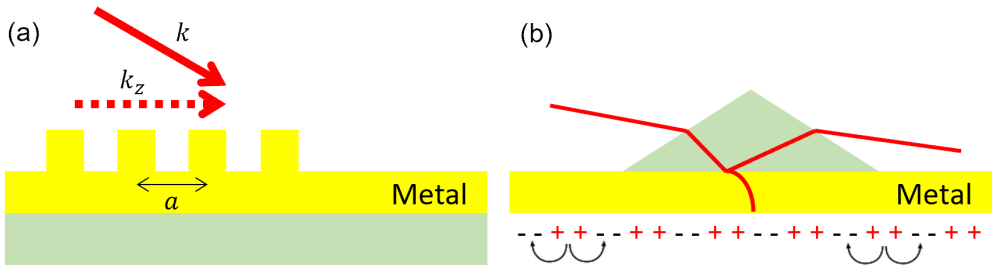

Fig. 1.13 Schematic representation of (a) a grating on a metal film and (b) a prism configuration to excite SPPs.

dielectric of a finite thickness (d_y) between the semi-infinite metal and semi-infinite dielectric layers to form an insulator-insulator-metal (IIM) structure. A schematic representation of this configuration is shown in Fig. 1.14 [116]. Before determining the effective properties of the effective media when the SPPs propagate through IIM, the configuration of insulator-insulator-metal-insulator (IIMI) must be solved first. Again, this involves obtaining the correct wave equation through Maxwell's equations, applying boundary conditions (a complete evaluation of all configurations can be found in Appendix D), and then solving this to produce a transcendental equation. However, this equation can be simplified, as the thickness of the metal layer can be assumed to be semi-infinite for relatively small values of metal thickness (on the order of hundreds of nanometers) due to the relatively shallow penetration of the SPPs [84], producing the IIM configuration shown in Fig. 1.14. Therefore, the simplified equation is:

$$\tanh(k_3 d_y) = \frac{\varepsilon_2 \varepsilon_3 k_3 k_4 + \varepsilon_4 \varepsilon_3 k_2 k_3}{\varepsilon_3 \varepsilon_4 k_3^2 + \varepsilon_3^2 k_2 k_4} \tag{1.17}$$

where k_i, and ε_i are the respective wave number and permittivity of the materials in the regions $i = 1,2,3$ shown in Fig. 1.14, and d_y denotes the thickness of the finite dielectric layer. The propagation constant in Eq. (1.17) is implicit and so $k_i = (\beta^2 - \varepsilon_i k_0^2)$ must be solved for, where β as a function of d_y, for a structure made of Au and Poly(methyl methacrylate) (PMMA), is shown in Fig. 1.14.

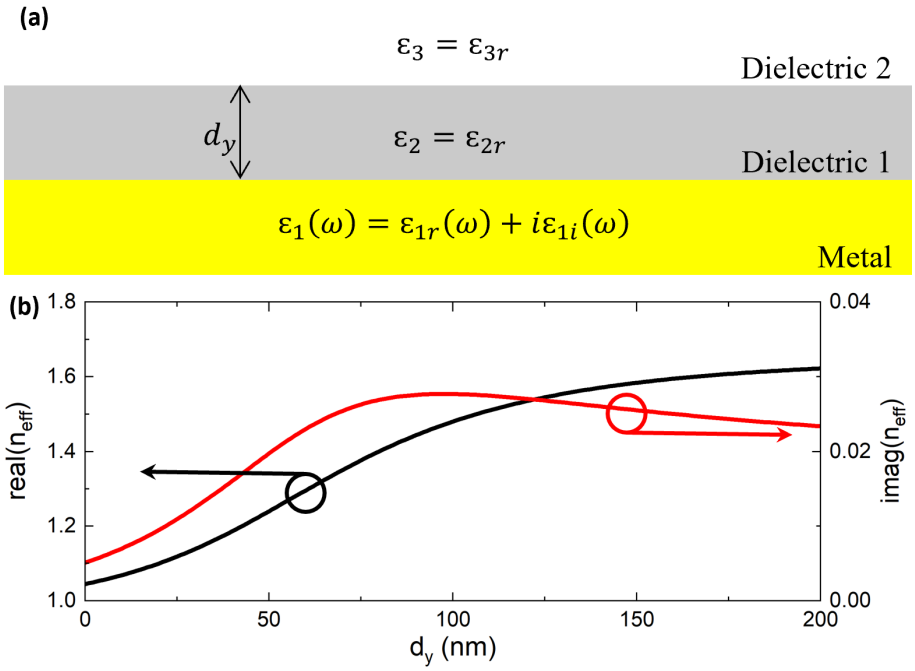

Fig. 1.14 (a) Schematic representation of an IIM system (b) Real (black) and imaginary (red) effective refractive index in a SPP IIM structure made of Au and PMMA as the dielectric thickness increases.

Chapter 2

From photonic nanojets to photonic hooks to bend light

Research aimed at challenging traditional concepts in optics, such as that diffraction limits the spatial resolution of imaging systems [117] and EM waves are considered to propagate rectilinearly [118], can contribute to improved efficiency and performance of EM devices for applications such as lenses [119] and optical trapping [120, 121]. Overcoming this fundamental limitation is crucial for resolving sub-wavelength objects or features [122]. This has prompted researchers to explore many different techniques, from MTMs [54, 123–125] and plasmonic structures [126–128], superlenses [129, 130], superoscillatory lenses [131], photonic crystals [132], diffractive optics [133] and dielectric particles at micro/nano-meter scales [134–137], among others. The traditional notion of ray optics where EM waves propagate in straight lines, dates back to Euclid in ancient Greece [138]. The exploration of curved beams initially emerged within the context of quantum mechanics, with experimental demonstrations using Airy-like accelerating curved beams. These beams are formed by freely accelerating wave packets, resulting in a parabolic arc within a medium. [139–141].

Recently, alternative methods exploiting mesoscale (sizes on the order of the incident wavelength) dielectric particles have been proposed. These particles have demonstrated the ability to produce a focus surpassing the diffraction limit [142] or causing light beams to bend [143]. This chapter discusses mesoscale dielectric particles in two different configurations, single dielectric particles, generating high spatial resolution beams and dual-dielectric particles to produce diffraction-limited bent light beams. The first configuration introduces singular dielectric particles in different geometries and illuminated types generating high-intensity narrow beams, known as photonic nanojets (PNJs). Collaborative work on PNJs is briefly outlined involving truncated high-index cylindrical(2D)/spherical(3D) dielectrics attached to the end of an optical fibre, including an evaluation of the power enhancement of

the structure and its spatial resolution [144]. Subsequently, some of the concepts of PNJs are applied in a second configuration to produce diffraction-limited structures EM beams with curvature, known as photonic hooks. This is achieved using two asymmetric 2D dielectric bars under plane wave illumination. The structures are first carefully designed, initially using a single particle to determine the minimum diffraction and maximum scattering. A systematic study of the two dielectrics explores the impact on the photonic hooks using various geometries, such as particle separation. The photonic hooks are evaluated quantitatively in terms of their length, Full-width at half-maximum (FWHM), and the spatial curvature on the focal plane.

2.1 Introduction to photonic nanojets

The Abbe barrier states that the diffraction of EM waves imposes an intrinsic limit on the spatial resolution of an imaging system. Consequently, the minimum resolvable distance of a focus converging to a spot will have a half angle (θ) defined as follows [25]:

$$d = \frac{\lambda}{2nsin\theta} \tag{2.1}$$

where λ is the operational wavelength and n is the refractive index of the medium the wave is propagating in.

In recent years, the exploration of PNJs has emerged as a promising strategy to surpass the intrinsic diffraction limit by exploiting evanescent fields [145, 146]. PNJs are defined as near-field, high-intensity narrow beams generated at the output surface of shaped dielectric particles [142]. Early works to achieve PNJs involved illuminating dielectric structures with a plane wave [147, 148]. This concept has been demonstrated across several frequency ranges. For example, Terajets have been observed at THz frequencies [149–151] while photonic nanojets (PNJs) are observed at optical frequencies [148, 146, 152].

A schematic representation in two- (2D) and three-dimensions (3D) of a potential structure to produce a PNJ consisting of a spherical dielectric structure with radius r is shown in Fig. 2.1a,b, respectively. Using this structure in a numerical simulation, illuminated by a plane wave, with a radius, $r = \lambda_0 = 1550\,\text{nm}$, a high-intensity narrow beam, a PNJ, can be seen in the power distribution, shown in Fig. 2.1c, of the dielectric sphere, at the output surface of the particle. Many geometries have been proposed for the dielectric particle including cylindrical/spherical as shown in Fig. 2.1 [153], cuboids [154, 149], graded-index structures [155] and plasmonic structures [100, 145], among others. PNJs have been demonstrated in a wide array of applications, including imaging and sensing [21, 142]. However, for

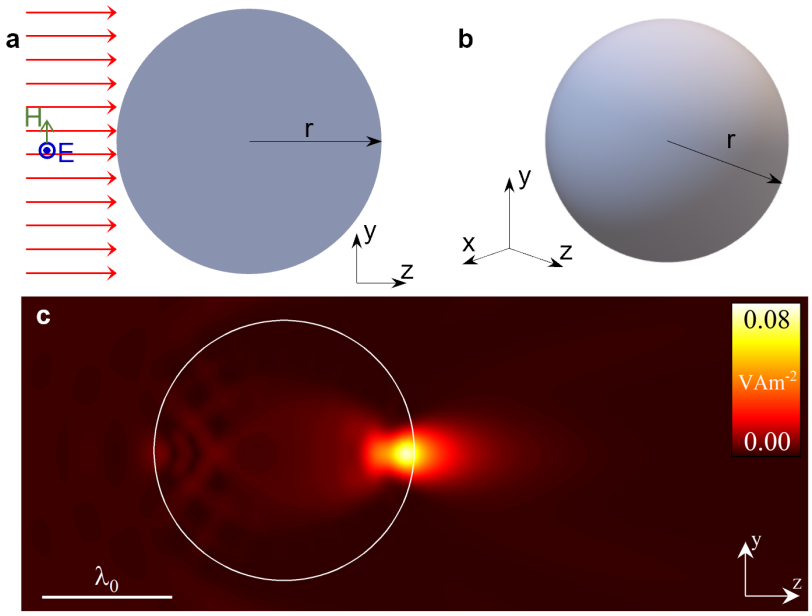

Fig. 2.1 (a) 2D and (b) 3D schematic representation of a spherical dielectric particle, radius r, capable of generating a PNJ when illuminated by a plane wave. (c) Power distribution of a spherical dielectric with a radius $r = 1550\,\text{nm}$ when illuminated by a plane wave.

these structures to generate a focus outside of the particle, the ratio of the refractive index of the particle n_d and the surrounding medium n_s must be less than 2 ($\frac{n_d}{n_s} < 2$) [156, 157]. Recent studies have explored dielectric particles with $\frac{n_d}{n_s} > 2$, achieving a focus outside of the particle by truncating a spherical particle in the direction of propagation, forming a hemispherical particle [158]. Additionally, studies into changing the illumination type such as using a Gaussian rather than a plane wave [159], have been explored. However, much of the work exploring PNJs uses an idealised design, which involves being free-standing in free space (without a substrate) while being illuminated with a plane wave. In a collaborative work, high-index $(n > 2)$ dielectric particles positioned on an optical fibre, operating at telecommunication wavelengths $(\lambda_0 = 1550\,\text{nm})$ were explored to generate PNJs. To achieve this, the particle was truncated to generate a sub-diffraction limit focus outside of the particle. A brief overview of this work is presented in Section B.2, with the full comprehensive study shown in Ref [144].

2.2 Introduction to photonic hooks

The exploitation of some concepts derived from PNJs has given rise to advancements that challenge established notions in structured light, allowing researchers to transcend traditional beliefs of EM, such as the rectilinear propagation of EM waves. This is achieved by

concentrating on specific regions of interest within an EM field [160–162]. Previous efforts have been able to achieve curved beams by generating artificial curved light using Airy beams [163, 141]. However, photonic hooks have demonstrated the capability to generate highly localised, curved beams of light in the near-field using specialised asymmetric mesoscale structures [160, 161]. The curvature of the photonic hook results from the constructive interference of the incident and tailored diffracted and scattered fields near the dielectric particles due to interactions in the near fields [164, 162]. These curved beams hold the potential to achieve beam waist sizes smaller than half of λ in the surrounding medium, offering opportunities for applications in sensing and optical trapping [160]. The realisation of photonic hooks involves breaking the symmetry of the structures through different methods [165]. For instance, the spatial symmetry of the structures can be broken by introducing a prism and attaching it to a dielectric cube, which would have generated a straight PNJ [160]. Another way to introduce asymmetry is to use oblique illumination to make the incident phase of the illuminating source asymmetric [151]. Janus particles, characterised by two carefully designed regions with distinct refractive indices and a determined angle of their internal boundary, offer another means of breaking symmetry [17, 161].

In a recent study, a plane wave was incident on two dielectric rectangular particles. When the two particles are symmetrical in terms of their size, shape and refractive index, a diffraction-limited focus is generated away from the shadow surface of the particles. The focal length, or the distance of the focus away from the shadow surface of the particles, is dependent on the separation between the two dielectrics [166]. The next section explores an interesting scenario when the symmetry of the two particles is intentionally broken. By using two distinct dielectric particles, the variations in phase velocity caused by their asymmetry can lead to interference effects that produce a focal point with curvature, resulting in a photonic hook [164], a phenomenon that cannot be achieved with identical particles.

2.3 Dual-dielectric photonic jets and hooks

The schematic representation of the proposed dual-dielectric structure, capable of generating both a PNJ and a photonic hook, is shown in Fig. 2.2. This structure consists of two dielectric particles made of different materials positioned in free space (refractive index of $n_0 = 1$), separated by a distance S. The refractive index for the two dielectrics is represented as $n_{1,2}$, for particles one and two, respectively. The dielectrics are modelled as 2D rectangular shapes with dimensions along the x- and z-directions represented by $(L_{x,1}, L_{z,1})$ for particle one and $(L_{x,2}, L_{z,2})$ particle 2.

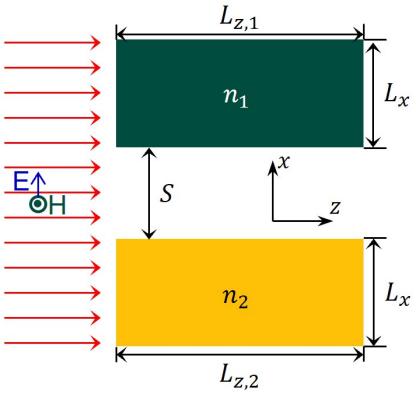

Fig. 2.2 Schematic representation of a plane wave incident on the proposed dual-dielectric particle structures designed to generate a photonic hook.

The evaluation of the structures is conducted utilising the transient solver of the commercial software CST Studio Suite®, for full-wave simulations (additional details provided in Section E.1), using an extra-fine hexahedral mesh. In the simulations, the dual-dielectric structures are illuminated under normal incidence using a TEM plane wave propagating in the $z-$ direction and polarised in the E_x direction, with a wavelength of $\lambda_0 = 3\,\text{mm}$. The particles are treated as 2D entities in free space, with open-add-space boundaries in the $\pm x$- and $\pm z$ directions and magnetic boundaries in the $\pm y$-direction.

2.3.1 Diffraction and Scattering of Dielectric Particles

Before generating photonic hooks using the two rectangular dielectric particles, it is essential to carefully engineer the refractive index of each particle and their respective geometries. As reported in [166] to produce an optimal focus using two symmetrical dielectric particles, the geometry and the EM properties of the particles should be selected to minimise diffraction in the direction of propagation at a selected point.

To evaluate the diffraction of a dielectric particle, a single particle from Fig. 2.2 is considered to be illuminated with a plane wave. From this, the diffraction of the particle $|\mathbf{E_{diffr}}|$ can be calculated. This involves evaluating the total $\mathbf{E}-$field ($\mathbf{E_{tot}}$) at a chosen point along the direction of propagation. Subsequently, the diffraction of the particle at the selected position is determined by taking the magnitude of $\mathbf{E_{tot}}$:

$$|\mathbf{E_{diff}}| = |\mathbf{E_{tot}}| = \sqrt{\mathbf{E_{tot,x}}^2 + \mathbf{E_{tot,y}}^2 + \mathbf{E_{tot,z}}^2} \tag{2.2}$$

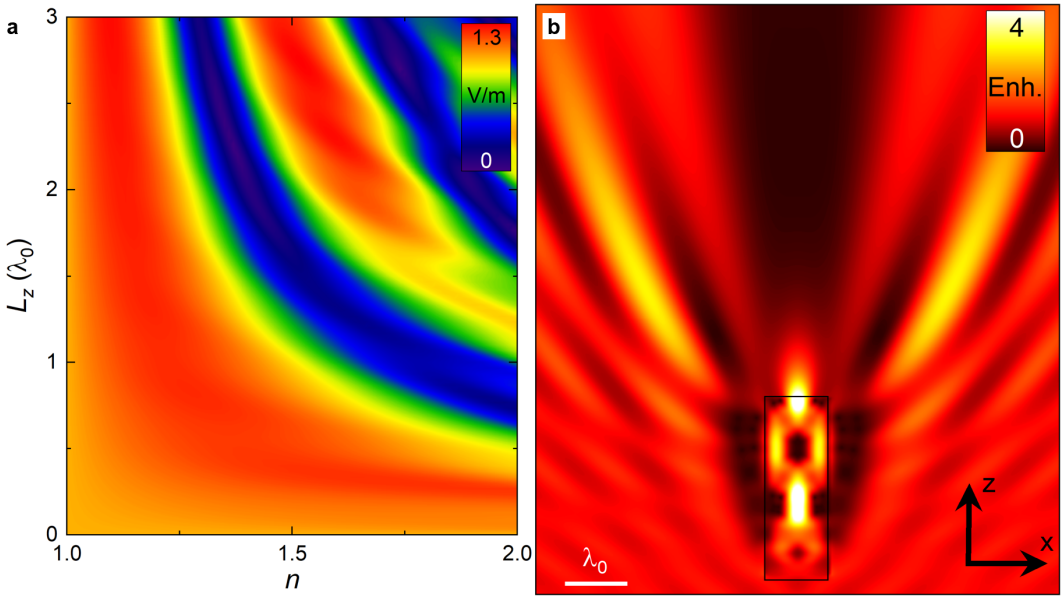

Fig. 2.3 (a) Electric field diffraction by a single dielectric particle in free space, evaluated $4\lambda_0$ from the shadow surface, while n and L_z of the particle varies. (b) Power enhancement of a single dielectric particle on the $xz-$plane with optimised parameters, $L_z = 2.3\lambda_0$ and $n = 1.37$

where $\mathbf{E_{tot,x}}$, $\mathbf{E_{tot,y}}$ and $\mathbf{E_{tot,z}}$ are the $x-$,$y-$ and $z-$ field components of the $\mathbf{E_{tot}}-$field. To determine the optimal properties for the particles, a systematic numerical evaluation of a single particle was conducted with variations in the $L_{z,1} = L_{z,2} = L_z$ dimension and the refractive index $n_1 = n_2 = n$. Throughout the following simulations, the widths of the two rectangular particles are fixed to $L_{x1,2} = \lambda_0$ to ensure a consistent basis to evaluate the impact of changing L_z and n. The L_z dimension is varied from 0 to $3\lambda_0$ in steps of $0.033\lambda_0$ while n varied from 1 to 2 in steps of 0.01. The evaluation of $|\mathbf{E_{diffr}}|$ for the particle is conducted at a point $z = 4\lambda_0$ from the centre ($x = 0$) of the shadow surface of the particle ($z = 0$). The values of $|\mathbf{E_{diffr}}|$ as these two parameters vary is shown in Fig. 2.3a, where it can be observed that $|\mathbf{E_{diffr}}|$ oscillates between minima and maxima. As stated earlier, the minimum $|\mathbf{E_{diffr}}|$ is desirable, so from Fig. 2.3a the minimum $|\mathbf{E_{diffr}}|$ is $0.0165\,\mathrm{Vm}^{-1}$ when $L_z = 2.3\lambda_0$ and $n_d = 1.37$. The power enhancement (ratio of the power distribution with and without the dielectric particle) of the single particle in this configuration is shown in Fig. 2.3b. Using these optimised values for two symmetrical particles ($n_1 = n_2 = 1.37$ and $L_{z,1} = L_{z,2} = 2.3\lambda_0$) separated by $S = 2\lambda_0$, a focus is generated, as shown in Fig. 2.4a. The focus is located at $2.41\lambda_0$, from the shadow surface, with a full-width at half-maximum, $FWHM = 0.705\lambda_0$, as shown in Fig. 2.4b,c, respectively.

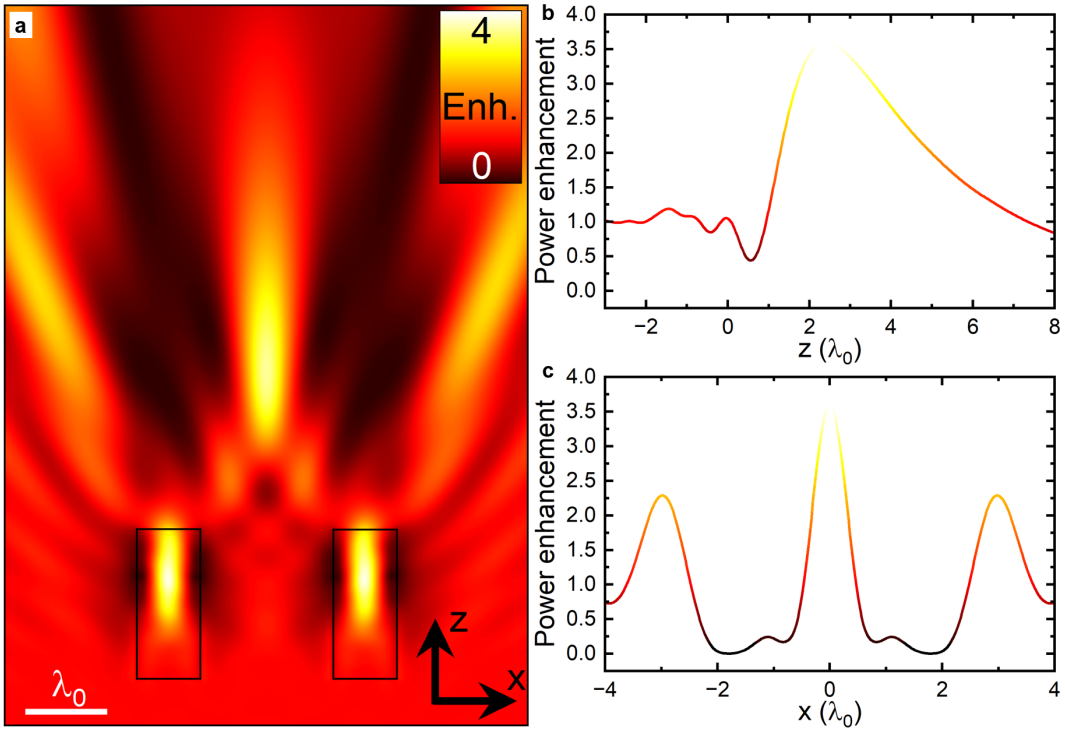

Fig. 2.4 Power enhancement (a) on the $xz-$plane of two symmetric dielectric particles with parameters, $L_z = 2.3\lambda_0$ and $n = 1.37$) and along the (b) $z-$axis at $x = y = 0$ and (c) $x-$axis at the focal length, $z = 2.41\lambda_0$

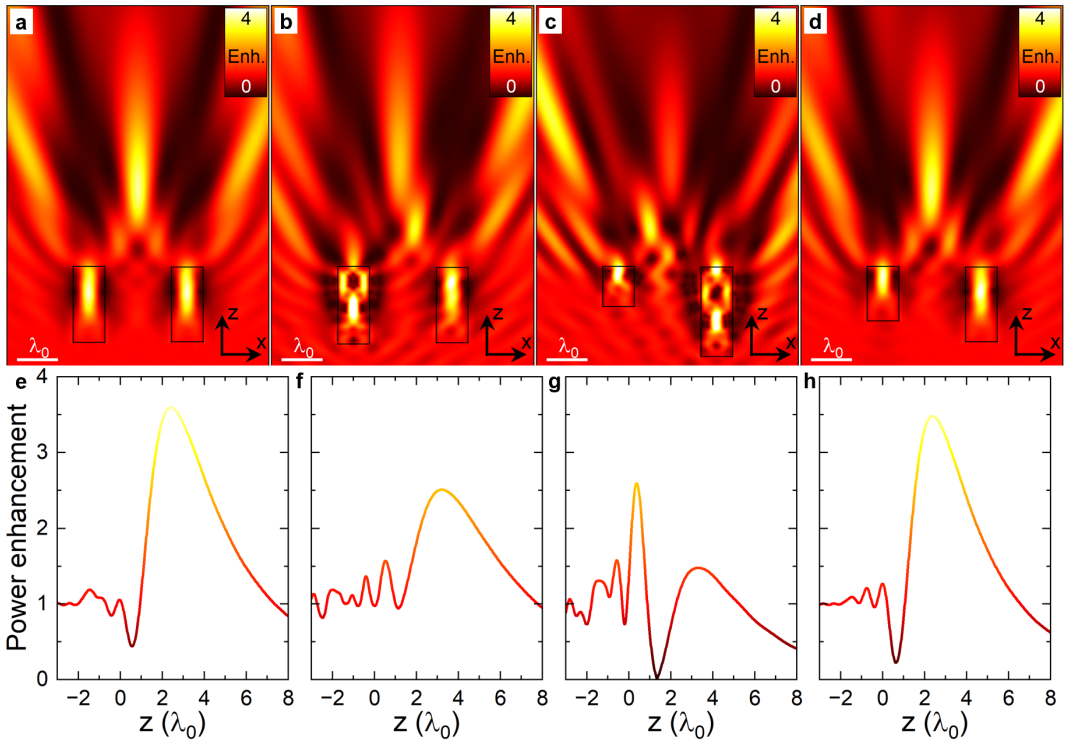

Fig. 2.5 Power enhancement on the $xz-$plane of different configurations of a dual-dielectric structure: (a) both particles have $L_z = 2.3\lambda_0$ and $n = 1.37$, (b) both particles have the same $L_z = 2.3\lambda_0$ but distinct $n_1 = 1.37$ and $n_2 = 1.83$, (c) both particles have the same $n = 1.74$ but different $L_{z,1} = 2.7\lambda_0$ and $L_{z,1} = 1.13\lambda_0$, and (d) the two particles are completely asymmetric with parameters $L_{z,1} = 2.3\lambda_0, L_{z,2} = 1.60\lambda_0$, $n_1 = 1.37$ and $n_2 = 1.5$. (e-h) Corresponding power enhancement at $x = y = 0$ along the $z-$axis for the configurations shown in (a-d).

Interestingly, a similar focus to the one shown in Fig. 2.4 can be achieved even when the particles are no longer symmetrical in terms of either n, L_z, or both. Altering these parameters to have similar small values of $|\mathbf{E_{diffr}}|$ results in the generation of a relatively straight focus. Examples are shown in Fig. 2.5, where Fig. 2.5a is the symmetric case shown previously, Fig. 2.5b has dielectric particles with the same $L_z = 2.3\lambda_0$ but $n_1 = 1.37$ and $n_2 = 1.83$, Fig. 2.5c has particles with the same $n_1 = n_2 = n_d = 1.74$ but $L_{z,1} = 2.7\lambda_0$ and $L_{z,1} = 1.13\lambda_0$, and Fig. 2.5d is completely asymmetric where $L_{z,1} = 2.3\lambda_0, L_{z,2} = 1.60\lambda_0$, $n_1 = 1.37$ and $n_2 = 1.5$. Note, the case where n is the same and L_z changes did not use the minimum diffraction from Fig. 2.3a at $n = 1.37$, as there is no second minimum in $|\mathbf{E_{diffr}}|$ within the range of L_z values shown in Fig. 2.3a.

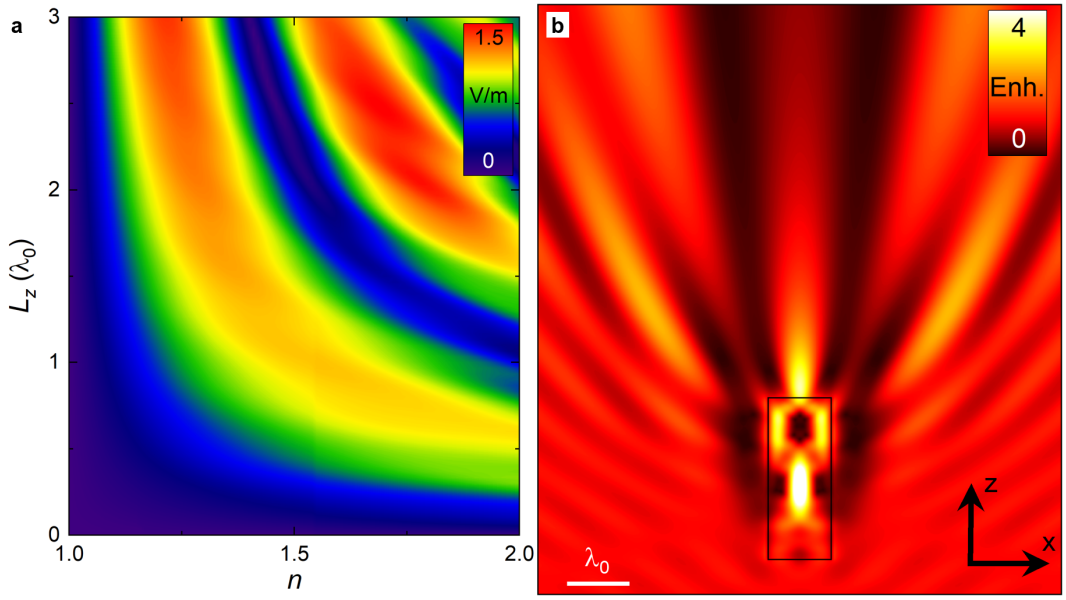

Fig. 2.6 (a) Electric field scattering by a single dielectric particle, evaluated $4\lambda_0$ from the shadow surface, as n and L_z vary. (b) Power enhancement on the $xz-$plane of a single dielectric particle with parameters, $L_z = 2.47\lambda_0$ and $n = 1.7$.

By calculating the power enhancement along the propagation direction and comparing the focal length of the three cases, it is demonstrated that the focus is generated at similar positions, $z \approx 2.4\lambda_0$, with some discrepancies due to different values of $|\mathbf{E_{diffr}}|$. The observation from Fig. 2.5 indicates that breaking the symmetry of the two particles solely in terms of geometry and/or refractive index does not introduce curvature to the focus. Therefore, to generate a bent focus, the other particle must influence the $\mathbf{E}-$field in a distinct way, different to the $|\mathbf{E_{diffr}}|$. Therefore, a further understanding of the EM properties of the particles is required, and so the scattering characteristics of a single particle are analysed. To calculate the magnitude of the scattered field ($|\mathbf{E_{scatt}}|$) by a dielectric particle, the $\mathbf{E}-$field

with dielectric particle ($|\mathbf{E_{tot}}|$) and the background $\mathbf{E}-$field without the particle ($|\mathbf{E_{bg}}|$), are obtained at the same position used for the calculation of $|\mathbf{E_{diffr}}|$. Then the $|\mathbf{E_{scatt}}|$ of the particle can be calculated as follows:

$$|\mathbf{E_{scatt}}| = |\mathbf{E_{bg}} - \mathbf{E_{tot}}| = \sqrt{(\mathbf{E}_{bg,x} - \mathbf{E}_{tot,x})^2 + (\mathbf{E}_{bg,y} - \mathbf{E}_{tot,y})^2 + (\mathbf{E}_{bg,z} - \mathbf{E}_{tot,z})^2} \quad (2.3)$$

Through a systematic variation of L_z and n using the same range to calculate $|\mathbf{E_{diffr}}|$, the values of $|\mathbf{E_{tot}}|$ and $|\mathbf{E_{bg}}|$ are obtained at the same position ($z = 4\lambda_0$). These are used to calculate the magnitude of the scattered field, $|\mathbf{E_{scatt}}|$, which is shown in Fig. 2.6a. Analysis of Fig. 2.6a reveals that the maximum scattering occurs when $L_z = 2.47\lambda_0$ and $n = 1.7$ with a value $|\mathbf{E_{scatt}}| = 1.51\ \mathrm{Vm}^{-1}$. The corresponding power enhancement of the single particle, under these specific values for maximum scattering, is shown in Fig. 2.6b. This analysis is pivotal for identifying conditions that maximise scattering and, consequently, contribute to the generation of a curved focus in the subsequent configuration of the two particles.

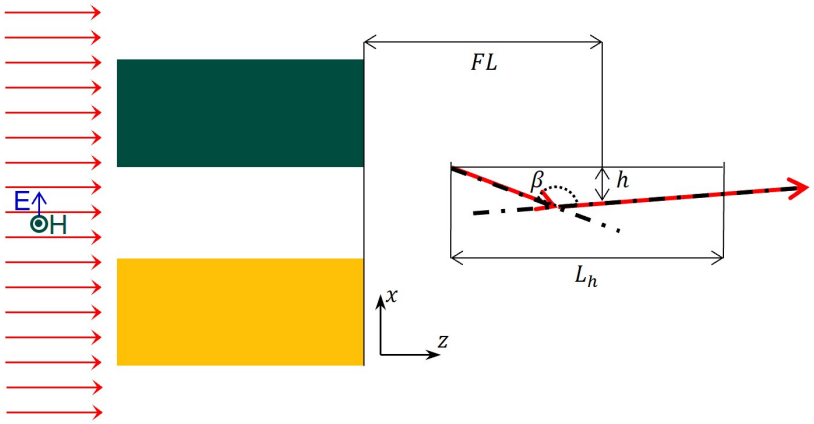

Fig. 2.7 Schematic representation of a photonic hook with properties L_h, h and β

To generate a bent focus, one of the particles is selected to have minimum diffraction and the other maximum scattering. A systematic exploration, varying one parameter at a time, will be presented in the next section. Initially, the case where both particles have the same n but different L_z will be discussed, followed by the opposite scenario, where L_z is kept the same and n varies. Then, for completeness, the case where both particles are asymmetric in terms of n and L_z is analysed. The quantitative analysis of the photonic hook properties involves calculating four parameters based on their respective power enhancements: the FWHM in the transversal direction, the length of the photonic hook (L_h), the height of the photonic hook (h), and the curvature of the hook (β). L_h represents the distance between the points when the power enhancement has decayed to $1/e$ of the power enhancement

of the focal point in the z-direction. h is the distance between L_h and the focal point in the x-direction. Finally, β denotes the curvature of the photonic hook itself. A schematic representation of how these parameters are calculated is presented in Fig. 2.7.

2.3.2 Particles with constant refractive index: effect of changing lengths

In this initial exploration, two configurations involving dual-dielectric rectangular blocks with the same value of n but with different L_z are studied. In the first configuration, one of the dielectric blocks is designed with n and L_z selected with minimum diffraction, as determined from Fig. 2.3a. The second block will be tailored to exhibit maximum scattering while maintaining the same n, achieved by varying L_z. In the second configuration, the roles are reversed, with the properties of one block chosen to have maximum scattering from Fig. 2.6a, and the second block is optimised to minimise diffraction with the same n.

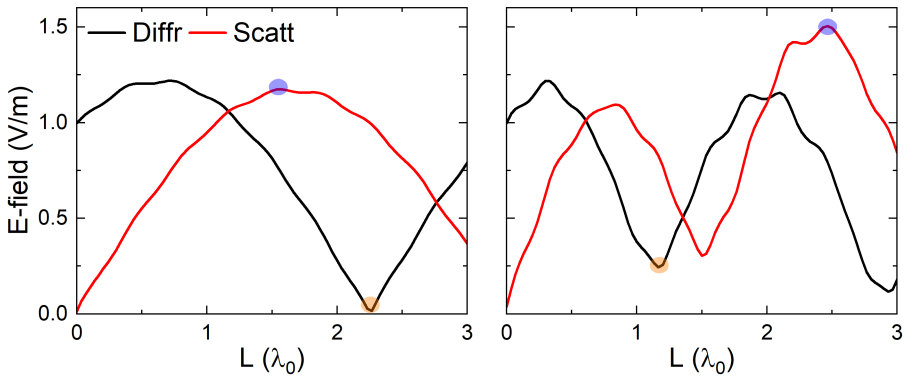

Fig. 2.8 Diffraction (black) and scattering (red) of a single dielectric particle with (a) $n = 1.37$ and (b) $n = 1.7$ as L_z varies. Circles show the position where minimum diffraction (orange) and maximum scattering (blue) occur.

For the first configuration, both blocks will have $n = 1.37$, with particle one designed to have $L_{z,1} = 2.3\lambda_0$ exhibit minimum diffraction at $z = 4\lambda_0$, from Fig. 2.3a. In configuration two, both blocks will have $n = 1.7$, and particle one will be tailored for maximum scattering at $z = 4\lambda_0$, with $L_{z,1} = 2.47\lambda_0$ from Fig. 2.6a. The values of $|\mathbf{E_{diff}}|$ and $|\mathbf{E_{scatt}}|$ for these values of n as L_z varies are shown as black and red lines in Fig. 2.8a,b, respectively. Orange and blue circles mark the values of L_z where minimum $|\mathbf{E_{diff}}|$ and maximum $|\mathbf{E_{scatt}}|$ occur, respectively, for these values of n. From this analysis, it is observed that maximum scattering for the second particle in configuration one occurs for $L_{z,2} = 1.57\lambda_0$. Meanwhile, particle two in the second configuration will have minimum diffraction when $L_{z,2} = 2.93\lambda_0$. Due to the discrepancy in the length of the particles, the alignment of the output and input surfaces

will influence the photonic hook produced. Therefore, the alignment of the particles will be explored to understand if and how this will impact the generated photonic hook.

Dual-dielectric particles aligned at their output surface

The schematic representation of the structure, with the output surfaces of the dielectric particles aligned, is presented in Fig. 2.9a. Both configurations are evaluated for different separations (S) ranging from 0 to $4\lambda_0$ in increments of λ_0 between the particles. These separations are chosen because diffraction and scattering are evaluated at $z = 4\lambda_0$, and the focal length is typically comparable to the separation distance [166]. The power enhancement for configuration one is shown in Fig. 2.9b, as a function of S. When there is no separation between the particles ($S = 0$), they behave as a single particle [17]. The power enhancement for configurations one and two with $S = 0\lambda_0$, are shown in Fig. 2.9b(i) and Fig. 2.9c(i), respectively. As expected, with no separation between the two dielectric particles, a power enhancement hotspot is produced close to the output surface of the two dielectric particles, primarily from the refracted wave generated within the dielectrics. This resembles the structures used to generate PNJs, as discussed in Section 2.1, albeit with an off-centre and slightly curved focus due to asymmetry.

The power enhancement for configuration one as S increases from λ_0 to $4\lambda_0$ is shown in Fig. 2.9b(ii-v). As the separation between the particles increases, the photonic hook becomes more clearly visible and extends further away from the output surfaces of the particles. This phenomenon results from the intensified interaction of scattering and diffraction field patterns from both particles. The power enhancement for the second configuration as S varies is shown in Fig. 2.9c. For small separations, $S = \lambda_0$ and $S = 2\lambda_0$, as with configuration one shown in Fig. 2.9b(ii-v), the photonic hook is close to the output surfaces of the particles. However, distinct photonic hooks can be clearly observed when $S = 3\lambda_0$ and $S = 4\lambda$. Quantitative analysis of the performance of the hooks is then conducted by calculating the parameters FWHM, L_h, h and β for each of the photonic hooks. These parameters for configuration one (black) and two (red) are presented in Fig. 2.10 as a function of S. From this analysis, several observable changes occur as the separation S increases. First, for larger values of S, L_h and the $FWHM$ also increase indicating that the photonic hooks are elongated with lower spatial resolution. Simultaneously, h and β generally both decrease due to the focal length of the photonic hook being further away from the shadow surface while taking longer to decay which is in agreement with the findings in [161]. From this, configuration one when the first particle has properties tailored for minimum diffraction from Fig. 2.3a performs better than configuration two.

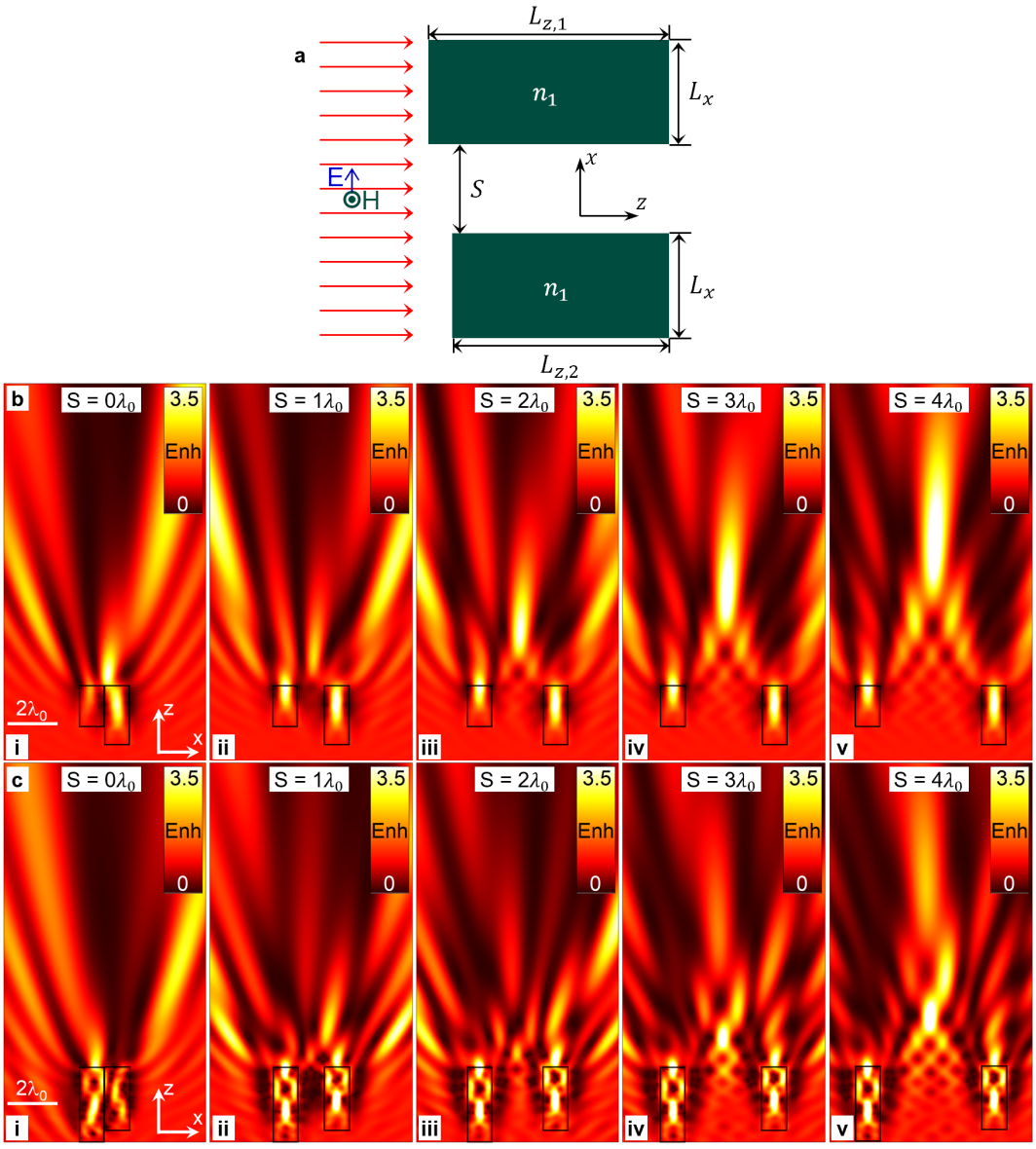

Fig. 2.9 (a) Schematic representation of the dual-dielectric structure with the same n and different L_z with the output surfaces of the particles aligned at $z = 0$. Power enhancement on the $xz-$plane of two dual-dielectric structure configurations with the output surfaces aligned at $z = 0$. (b) Configuration one has particles with $L_{z,1} = 2.3\lambda_0$, $L_{z,2} = 1.57\lambda_0$ and $n_1 = 1.37$ (c) Configuration two has particles with parameters $n = 1.7$, $L_{z,1} = 2.47\lambda_0$, and $L_{z,2} = 2.93\lambda_0$. The separation between the particles (S) is varied by values of (i) $0\lambda_0$, (ii) $1\lambda_0$, (iii) $2\lambda_0$, (iv) $3\lambda_0$ and (v) $4\lambda_0$.

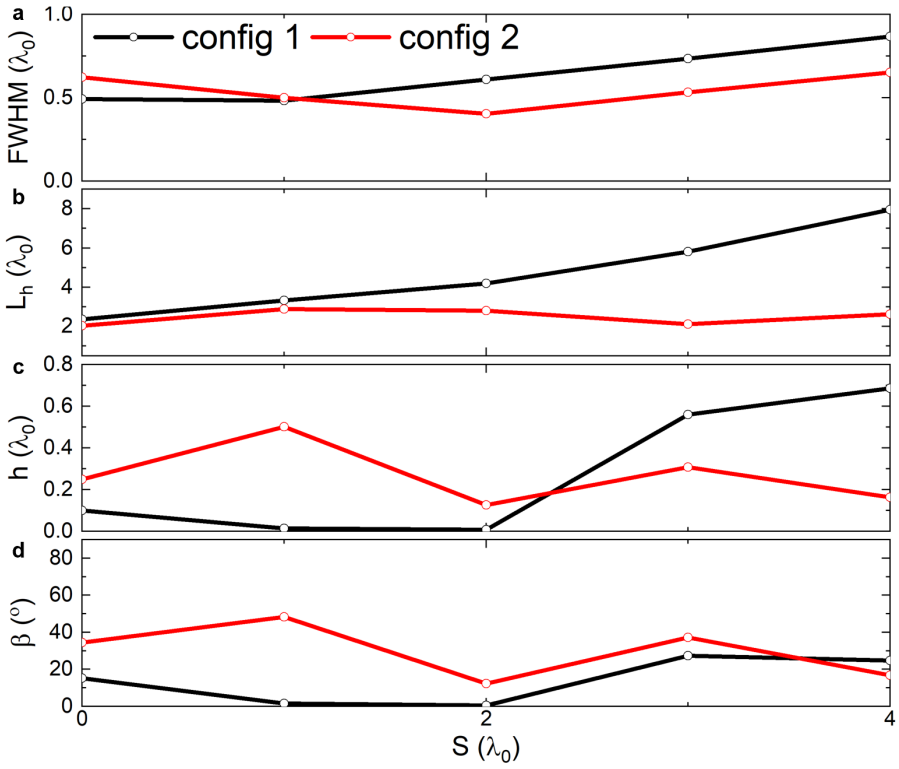

Fig. 2.10 (a) FWHM, (b) L_h, (c) h and (d) β of the photonic hooks produced by the dual-dielectric configurations one (black) and two (red) shown in Fig. 2.9.

Dual-dielectric particles aligned at their input surface

In this further analysis, the same dielectric particle structures as in the previous section are reconsidered. However, this time the input surfaces of the particles aligned instead of the output surfaces. By changing the alignment of the particles, one would expect slightly different interference of the $|\mathbf{E_{diff}}|$ and $|\mathbf{E_{scatt}}|$ fields, resulting in different properties of the photonic hooks. A schematic representation of this arrangement of the particles is shown in Fig. 2.11a. The power enhancements for the two configurations, previously examined with their output surfaces aligned, now evaluated with their input surfaces aligned as the S varies from 0 to $4\lambda_0$, are shown in Fig. 2.11b,c, respectively. As expected, the generated photonic hooks closely resemble those shown in Fig. 2.9. However, there are some slight differences when conducting quantitative comparisons of the hooks. Once again, as S increases, the hooks become more elongated with lower spatial resolutions, indicated by the increased values of L_h and FWHM, while the hooks exhibit less curvature as h and β decrease. When $S = 0$, there is a significant difference between the values of the parameters for the two alignments. This is due to the hook being close to the surface so changes to the geometry, such as the particle alignment, will have a more significant effect on the mostly refracted EM wave when $S = 0$ as the dual-particles behave like a single particle as with the cases shown in Section 2.3.2. However, as S increases in Fig. 2.12, the parameters of the photonics hooks generated by the different particle alignments converge until there is little difference between the two.

2.3.3 Effect of changing refractive index with constant particle length

This subsequent exploration investigates maintaining the same L_z for both particles and changing n, representing the reverse scenario from Section 2.3.2. A schematic representation of this scenario is shown in Fig. 2.13a. As in Section 2.3.2, two configurations are considered. These configurations utilise the same initial blocks with minimum diffraction ($n_1 = 1.37$ and $L_z = 2.3\lambda_0$) and maximum scattering from ($n_1 = 1.7$ and $L_z = 2.47\lambda_0$) for configurations one and two, respectively. The properties of the second block for each configuration are then selected maintaining the same L_z as the first particle but varying n to tailor a particle that exhibits high scattering for configuration one, and low diffraction for the second configuration. The corresponding $|\mathbf{E_{diff}}|$ and $|\mathbf{E_{scatt}}|$ at these values of L_z are shown in Fig. 2.13b,c for configurations one and two, respectively. For configuration one, the second dielectric particle has properties of $n_2 = 1.72$ and $L_z = 2.3\lambda_0$, while the particle in configuration two has properties of $n_2 = 1.49$ and $L_z = 2.47\lambda_0$. Again, the separation between the two dielectric particles is varied, and the photonic hook is observed using the power enhancement on

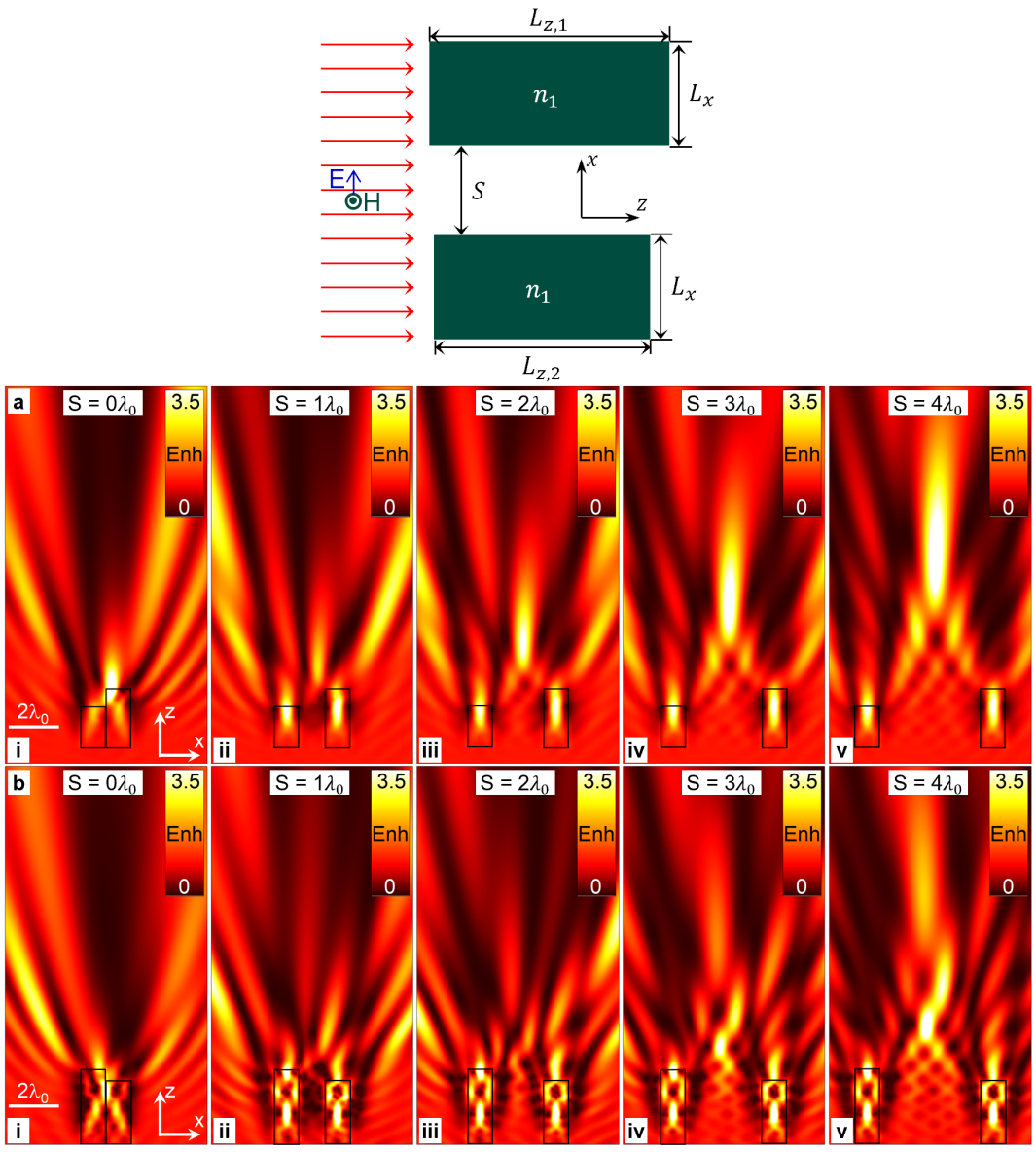

Fig. 2.11 (a) Schematic representation of the dual-dielectric structure with fixed n and different L_z with the input surfaces aligned. Power enhancement on the $xz-$plane of two dual-dielectric structure configurations with the input surfaces aligned. (b) Configuration one has particles with $L_{z,1} = 2.3\lambda_0$, $L_{z,2} = 1.57\lambda_0$ and $n_1 = 1.37$ (c) Configuration two has particles with parameters $n = 1.7$, $L_{z,1} = 2.47\lambda_0$, and $L_{z,2} = 2.93\lambda_0$. The separation between the particles (S) is varied by values of (i) $0\lambda_0$, (ii) $1\lambda_0$, (iii) $2\lambda_0$, (iv) $3\lambda_0$ and (v) $4\lambda_0$.

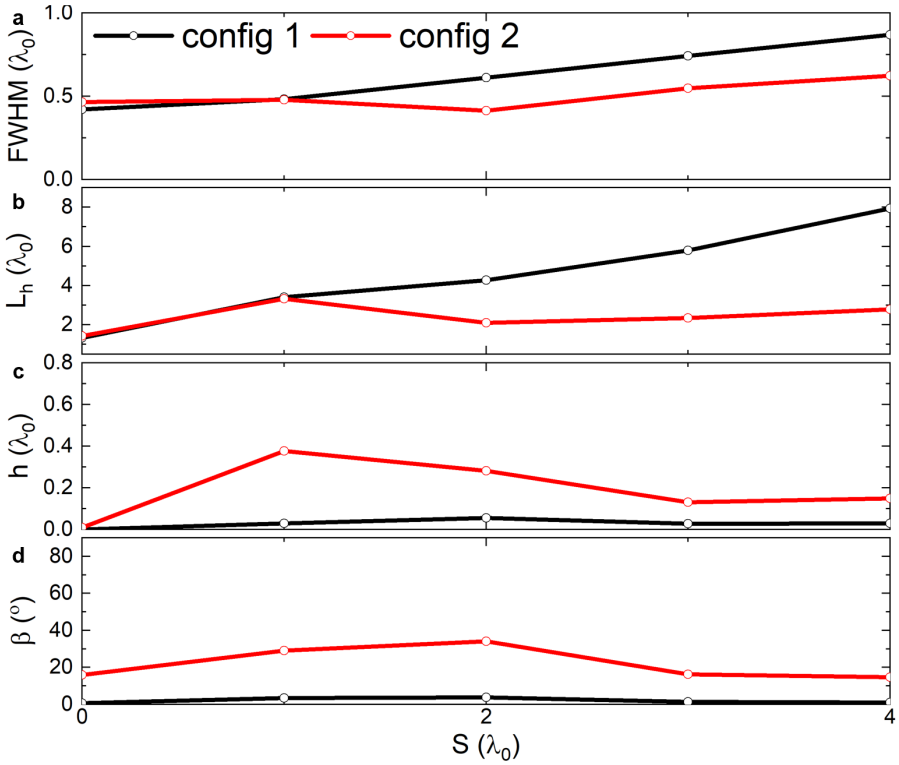

Fig. 2.12 (a) FWHM, (b) L_h, (c) h and (d) β of the photonic hooks in Fig. 2.11 for configurations one (black) and two (red) with aligned input surfaces.

the xz-plane. For configuration one, the power enhancement is shown in Fig. 2.13d, and configuration two is shown in Fig. 2.13e. For all separations, a photonic hook is observed. Similar to the case in Section 2.3.2, as the separation increases the photonic hook shifts away from the shadow surface of the dielectrics, becoming elongated. The quantitative parameters of the photonic hooks are then shown in Fig. 2.14. Using a fixed value of L_z behaves similarly to the case with fixed n, as one would expect. Fig. 2.14a quantitatively shows the observations of the photonic hook becoming elongated as the separation increases, while the spatial resolution decreases, as shown in Fig. 2.14b. Meanwhile, as with the reverse scenario, the magnitude of h decreases as the curvature of the hook, β, decreases, shown in Fig. 2.14c,d, respectively.

2.3.4 Full asymmetry

The final scenario investigated involves complete asymmetry of the particles in terms of the geometry and EM properties. This scenario employs the optimal cases for minimum diffraction and maximum scattering obtained from Fig. 2.3a and Fig. 2.6a, respectively. The first dielectric particle has minimum diffraction with properties of $L_{z,1} = 2.3\lambda_0$ and $n_1 = 1.37$, while the second dielectric particle will have maximum scattering with properties of $L_{z,2} = 2.47\lambda_0$ and $n_2 = 1.7$. As with Section 2.3.2, the particles can be aligned either by their input or output surface. The power enhancement on the xz-plane as the separation increases from $S = 0$ to $S = 4\lambda_0$ in steps of λ_0, with the input and output surfaces aligned, is shown in Fig. 2.15a,b, respectively. Once again, a photonic hook is produced for all separations of the particles, with a quantitative analysis of the generated photonic hooks by the fully asymmetric particles shown in Fig. 2.16. The behaviour of these structures is similar to the cases explored in Section 2.3.2, with the photonic hooks becoming elongated, moving further away from the shadow surface of the particles with lower spatial resolutions and less curvature as the separation increases.

2.3.5 Experimental practicalities

Finally in this section, a study is conducted to ascertain the practical feasibility and validity of the proposed structures outlined in Section 2.3.2, 2.3.3 and 2.3.4 within an experimental context. This is necessary given that all of the numerical simulations considered in the previous section evaluate the particles as free standing in free space, making them potentially challenging to realise experimentally. To validate these scenarios for potential fabrication in the future, a comprehensive study is conducted to evaluate their response when the two dielectric particles are placed on a dielectric substrate. The schematic representations of

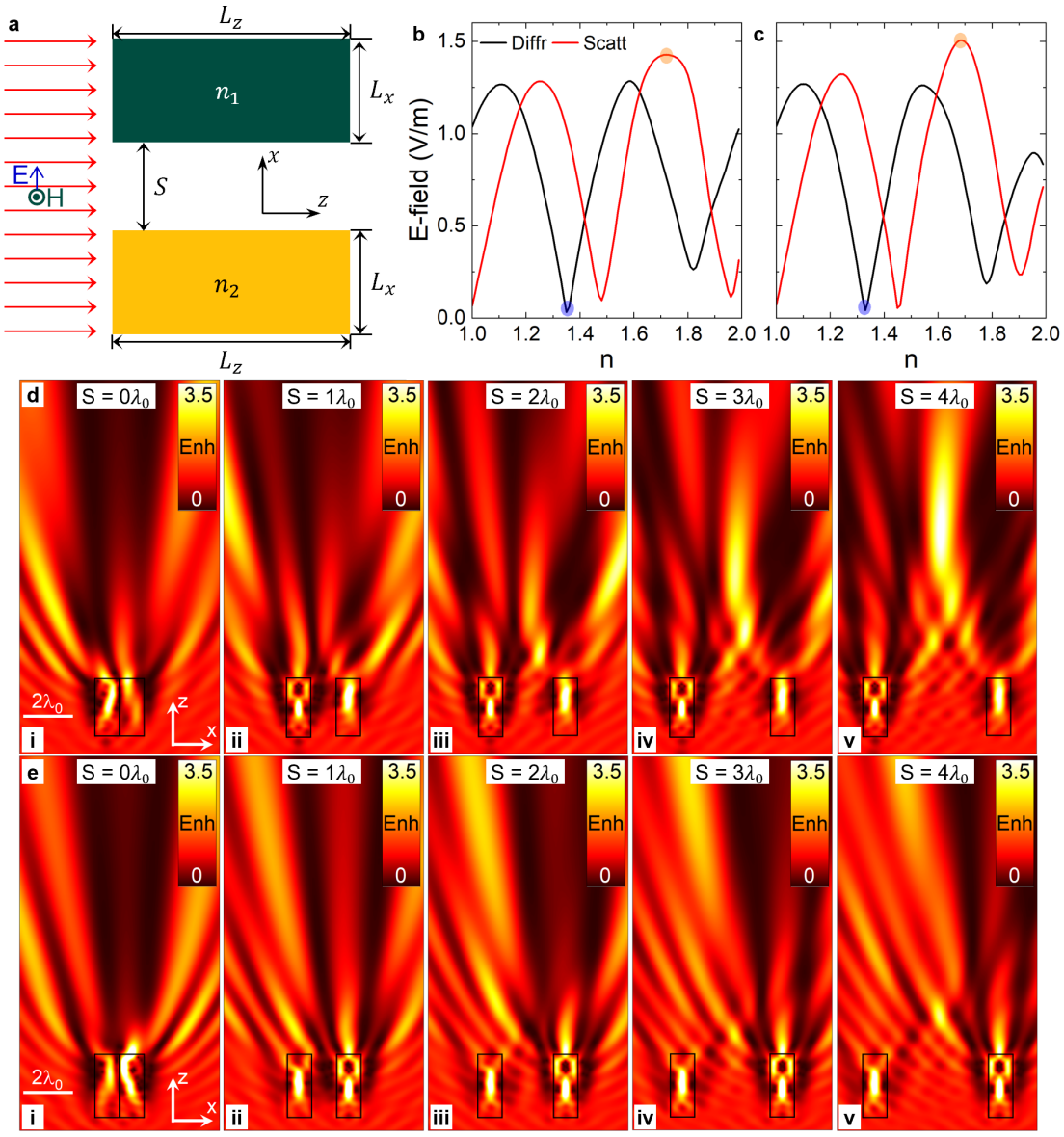

Fig. 2.13 (a) Schematic representation of the dual-dielectric structure with the same L_z and different n. Diffraction (black) and scattering (red) of a single dielectric particle with (b) $L_z = 2.3\lambda_0$ and (c) $L_z = 2.47\lambda_0$ as n varies. Circles show where minimum diffraction (orange) and maximum scattering (blue) occur. Power enhancement on the $xz-$plane of two dual-dielectric structure configurations with the input surfaces aligned. (d) Configuration one has particles with $L_{z,1} = 2.3\lambda_0$, $n_1 = 1.37$ and $n_2 = 1.72$ (e) Configuration two has particles with parameters $n = 1.7$, $L_{z,1} = 2.47\lambda_0$, and $n_2 = 1.49$. The separation between the particles (S) is varied by values of (i) $0\lambda_0$, (ii) $1\lambda_0$, (iii) $2\lambda_0$, (iv) $3\lambda_0$ and (v) $4\lambda_0$.

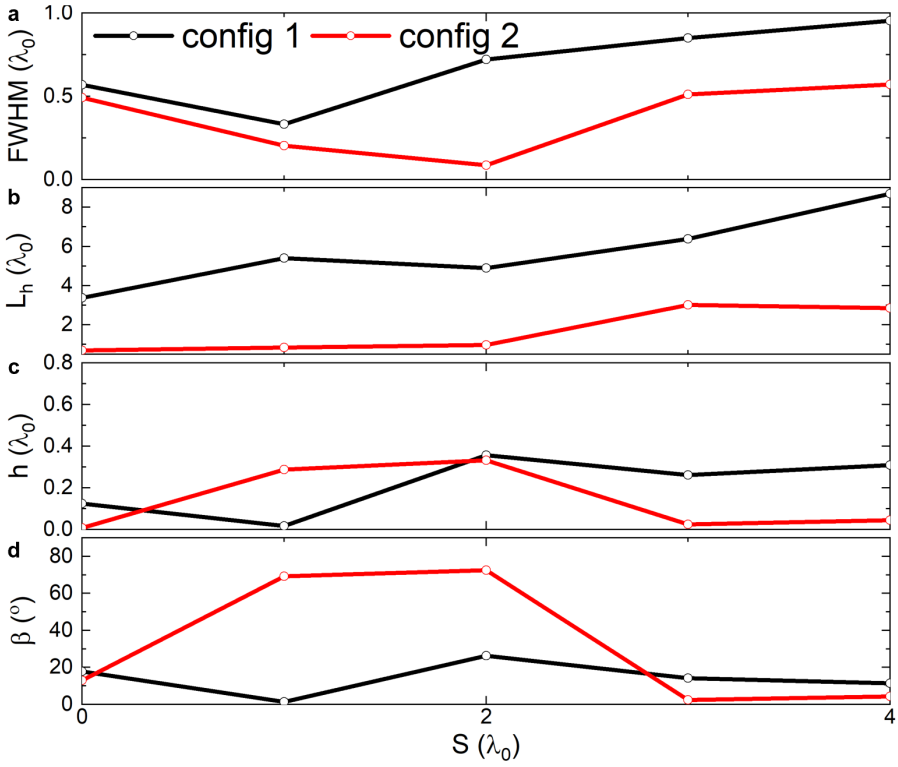

Fig. 2.14 (a) FWHM, (b) L_h, (c) h and (d) β of the photonic hooks produced by the dual-dielectric configurations one (black) and two (red) from Fig. 2.13

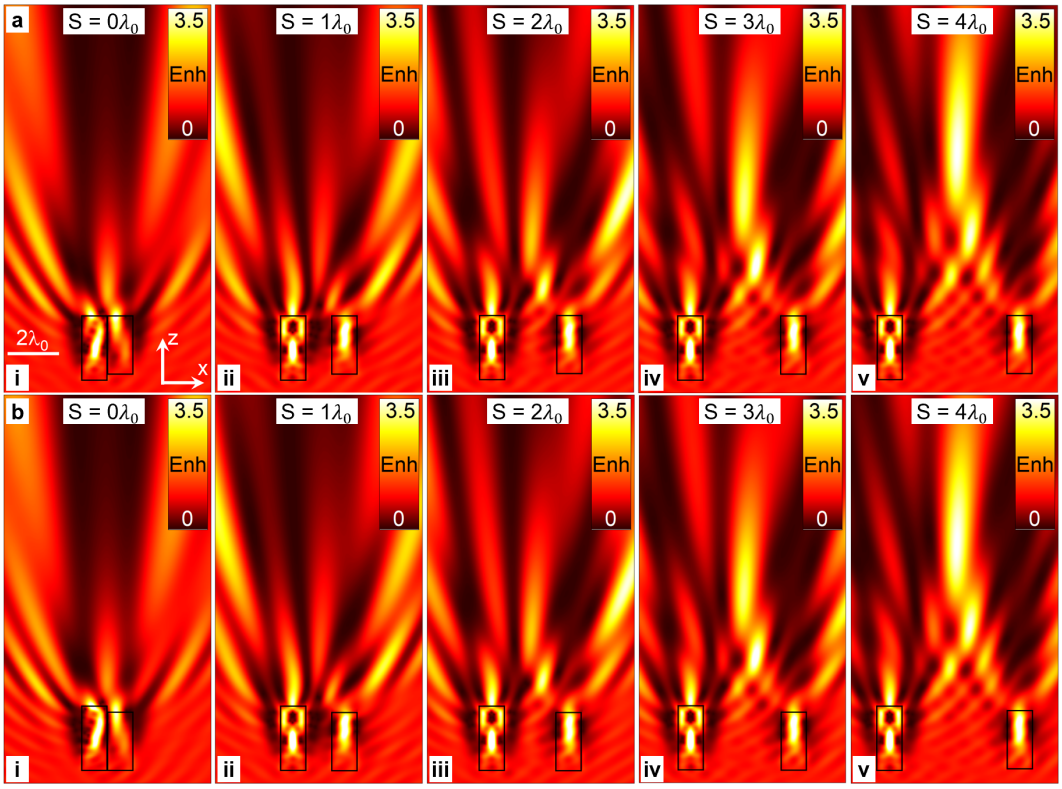

Fig. 2.15 Power enhancement on the $xz-$plane of dual-dielectric structures with particle properties, $L_{z,1} = 2.3\lambda_0$, $n_1 = 1.37$ and $L_{z,2} = 2.47\lambda_0$ and $n_2 = 1.72$. The two particles are then aligned at their (a) output or (b) input surface. The separation between the particles (S) is varied by values of (i) $0\lambda_0$, (ii) $1\lambda_0$, (iii) $2\lambda_0$, (iv) $3\lambda_0$ and (v) $4\lambda_0$.

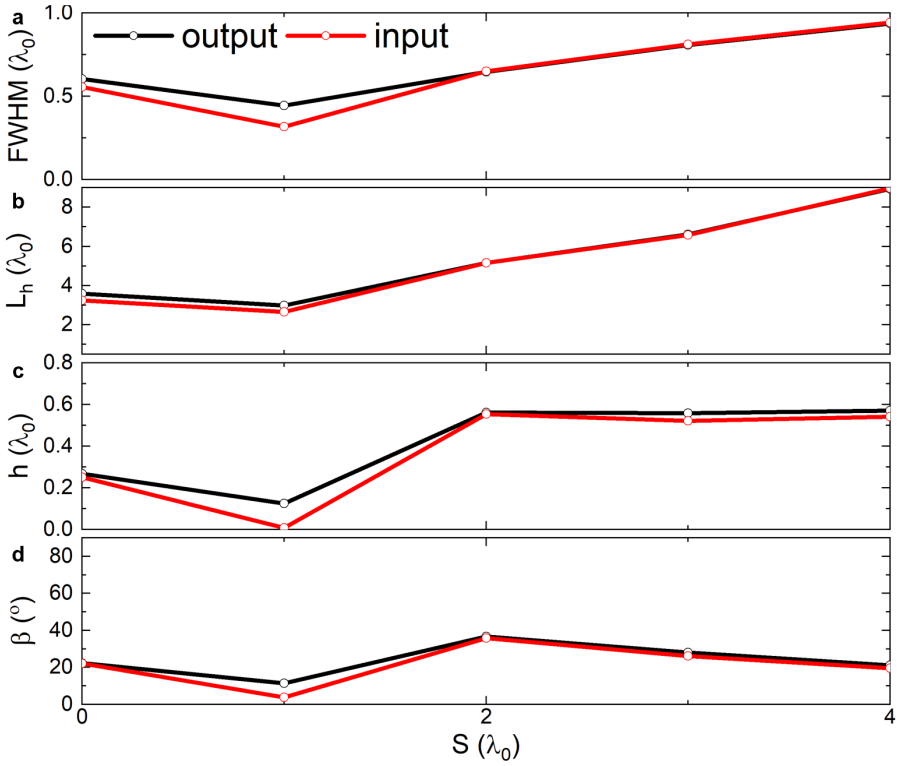

Fig. 2.16 (a) FWHM, (b) L_h, (c) h and (d) β of the photonic hooks produced in Fig. 2.15 when aligned at the output (black) and input (red) surfaces.

the two potential experimental setups are shown in Fig. 2.17a,b, where the planar dielectric substrate is attached to the input or output surface of the particles, respectively, with a thickness in the direction of propagation of $L_{z,3} = \lambda_0$. The refractive index (n_3) of the dielectric material is varied ranging from 1 to 1.4 in steps of 0.2.

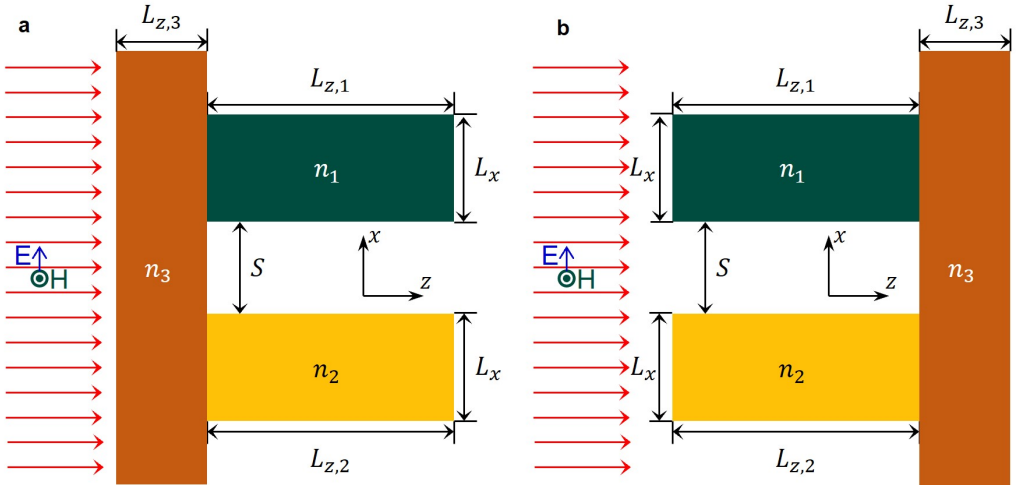

Fig. 2.17 Schematic representation of the dual-dielectric particle structures with a dielectric substrate with refractive index n_3 and thickness $L_{z,3}$ attached to the (a) input and (b) output surfaces of the particles

The power enhancement on the xz-plane of the input surface of the particles aligned and attached to the substrate, as shown in Fig. 2.17a, is shown in Fig. 2.18 for each of the methods used to break the symmetry, as explored in the previous sections. In Fig. 2.18a, the symmetry of the structures is broken using the same n configuration while varying L_z (Section 2.3.2). In Fig. 2.18b varies n while the value of L_z is kept constant (Section 2.3.3) and Fig. 2.18c explores the asymmetrical case (Section 2.3.4). The power enhancement for these cases is evaluated as the power distribution ratio when particles are attached to the substrate and when it is the substrate alone.

The cases where L_z and n vary as well as the completely asymmetric case, with the particles attached to the substrate on their output surface, the power enhancement for the are shown in Fig. 2.19a,b,c, respectively. As observed in Fig. 2.18 and Fig. 2.19, a photonic hook is still generated for all three methods of breaking the symmetry of the structures when the substrate is attached to both the input and output surfaces of the particles. As expected, when the refractive index of the substrate $n_3 = 1$ the photonic hook is the same as the cases when they are shown in free space in the previous sections. However, when $n_3 > 1$ distortions occur in the generated photonic hooks due to the interference being changed by the presence of the substrate. Therefore, this configuration could be used in a potential experimental

realisation, however careful consideration must go into the dielectric used for the substrate to minimise these distortions. The results shown in this chapter could be extended to different EM frequency ranges from microwaves to the optical regime.

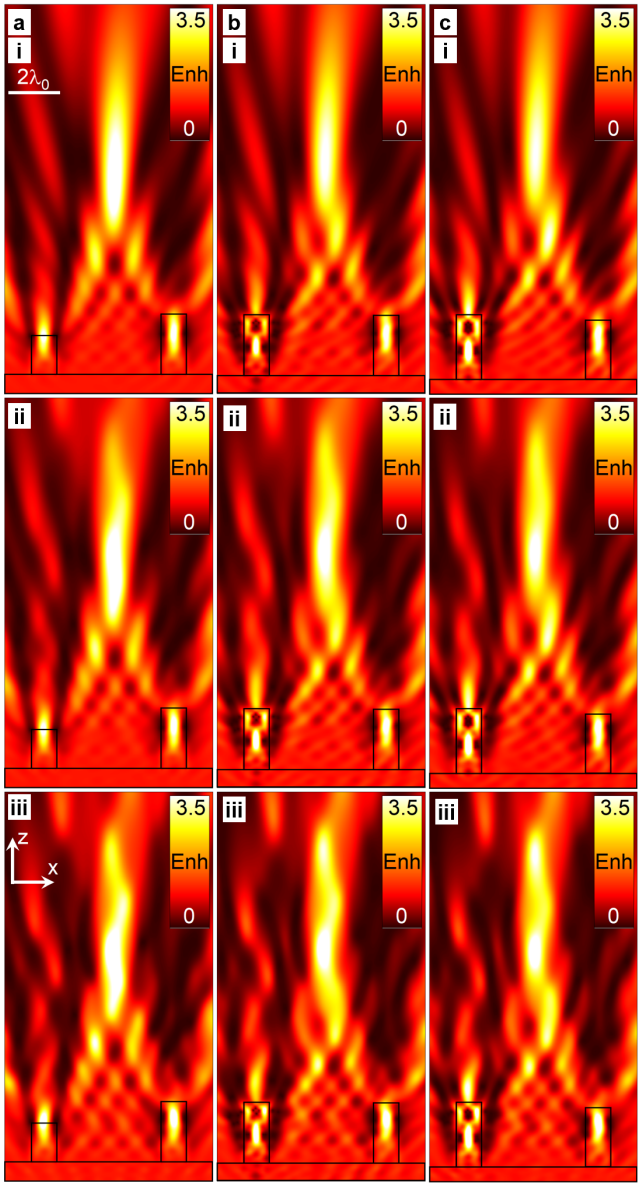

Fig. 2.18 Power enhancement on the $xz-$plane for the structures discussed in (a) Fig. 2.9a(v), (b) Fig. 2.13a(v), and (c) Fig. 2.15a(v) attached to a dielectric substrate ($L_{z,3} = \lambda_0$) on the input surface. The refractive index of the substrate is varied $n_3 =$ (i) 1, (ii) 1.2, and (iii) 1.4.

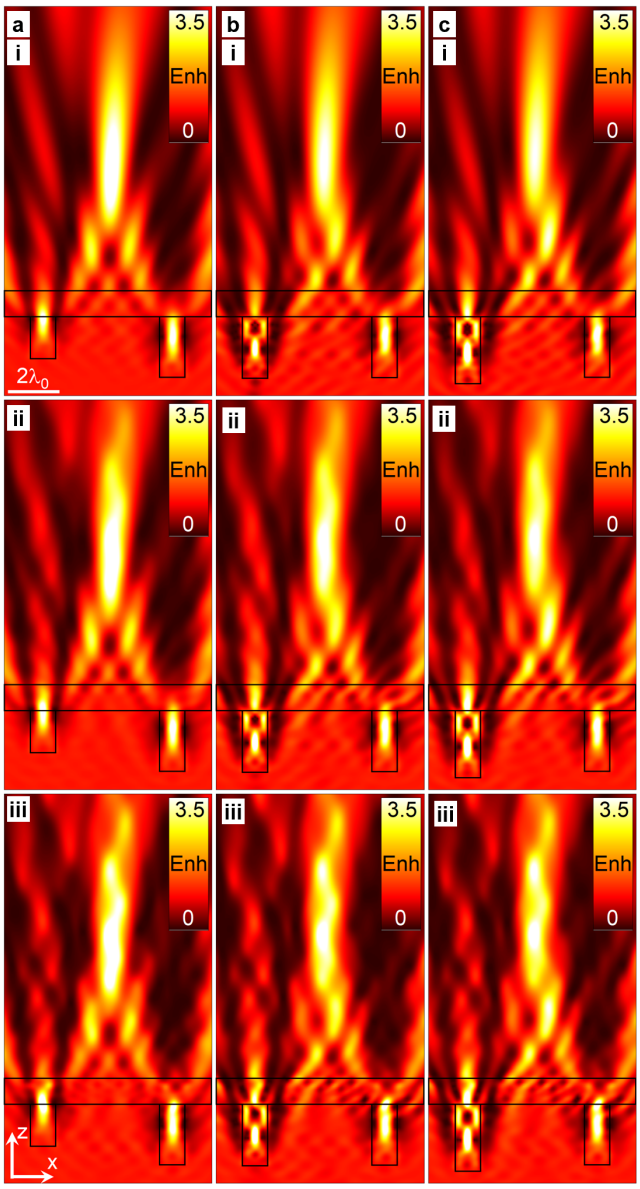

Fig. 2.19 Power enhancement on the $xz-$plane for the structures discussed in (a) Fig. 2.11a(v), (b) Fig. 2.13a(v), and (c) Fig. 2.15b(v) attached to a dielectric substrate ($L_{z,3} = \lambda_0$) on the input surface. The refractive index of the substrate is varied $n_3 =$ (i) 1, (ii) 1.2, and (iii) 1.4.

Chapter 3

Exploiting surfaces plasmons polaritons and classical electromagnetism for focusing structures.

Finding methods capable of manipulating and controlling EM waves on the nanometre scales, to improve our command and to miniaturise photonic structures, has led to the emergence of nanophotonics as a field of study. This development has given rise to the sub-field of plasmonics, which has demonstrated efficient control of EM waves at these nanoscales by exploiting the coupling between EM waves and the conduction electrons in metals at optical frequencies (see Section 1.3.1). Plasmonics encompasses two important aspects: SPPs, explored in this chapter, and LSPs, which will be the focus of Chapter 4.

SPPs are EM surface waves that propagate along the interface between a dielectric and a metal [84, 167]. When photons at optical frequencies couple with the conduction electrons within a metal SPPs are excited, producing coherent collective oscillations of the electrons [113]. These oscillations enable the existence of surface waves that are strongly confined at the metal-dielectric boundary [168], decaying perpendicular to the boundary and as they propagate because at optical frequencies metals are intrinsically lossy [169]. As SPPs boast high data-carrying capacities [170] at micro/nano-meter scales [171] they have found applications in diverse fields and settings from focusing [172, 173] and sensing [174] to waveguiding [175] and optical trapping [176]. In this context, the pursuit of new and enhanced methods of controlling the propagation of SPPs is crucial to further employ them in ultra-compact structures [34, 115].

The expansion of research into plasmonic lenses has been mutually beneficial for both the field of lenses and the field of SPPs. Many different techniques have been proposed for designing plasmonic focusing devices, including the excitation of PNJs exploiting cuboid

and cylindrical structures [100, 145], and achromatic lenses for broadband SPP focusing [20, 177], among others. In this realm, to design focusing devices for SPPs, classical optics techniques can be adapted and applied to plasmonic structures [178, 168, 105]. This adaption has led to analogous plasmonic devices being demonstrated to manipulate and focus SPPs. These include plasmonic Fresnel lenses [179], double convex designs [20], as well as Eaton and Luneburg lenses [180], among others.

In this chapter, a technique commonly employed to design lenses within the realm of classical optics, the *lens maker equation*, is adapted and exploited for SPPs at visible wavelengths to produce plasmonic meniscus lenses. First, an analytical study is conducted to determine the effective refractive index of the different regions required to produce refractive elements with SPPs. The *lens maker equation* is then modified to use these effective medium concepts to design plasmonic lenses with various geometric profiles. Two geometries for the plasmonic lens, namely a convex-planar and a positive meniscus lens, are evaluated using both ideal 2D and realistic 3D numerical simulations. The performance of the two lens geometries in both 2D and 3D is assessed and compared in terms of their power enhancement and spatial resolution, in both the direction of propagation and transverse to it. The lenses are then explored in a range of wavelengths to demonstrate their broadband response. Finally, a series of studies investigate the robustness of the lenses using oblique incidence of illumination as well as the influence of potential fabrication errors, such as dielectric thickness or geometric anomalies, on lens performance.

3.1 Effective Refractive Index of SPPs

A 2D schematic representation of the proposed 3D structure on the yz-plane is shown in Fig. 3.1a. SPPs propagate along the air-Au interface in the positive z-direction in this configuration. Given that SPPs are TM waves (as explained in Appendix D), the magnetic field is aligned parallel to the x-axis, and the electric field has y- and z-components. In the study shown here, The structure consists of a 250 nm thick gold (Au) film, characterised by a dispersive refractive index modelled using experimental complex refractive index data from Johnson and Christie [1]. The surrounding medium is free space ($n_0 = 1$), and a 3D dielectric particle with a designed height is positioned on the Au surface, creating two distinct regions on the $yz-$plane where the SPPs will propagate. The first region is the air-gold (IM) interface (labelled *i* in Fig. 3.1, and the second region (IIM, labelled *ii*) is where the shaped dielectric is positioned on the Au. Silicon nitride (Si_3N_4) is selected as the dielectric material for this study, with a refractive index of approximately 2.01. As Si_3N_4 is slightly dispersive at optical, visible wavelengths, it will be modelled in the numerical studies using the experimental data

from ref [181]. It is important to note that different dielectrics could be implemented instead of Si_3N_4, such as poly(methyl methacrylate) (PMMA) as shown in Eq. (1.15). However, in the study shown in this chapter, Si_3N_4 is used due to its relatively high refractive index, which allows the design of compact plasmonic devices, making it a widely used material within the realm of plasmonics.

Before moving on to studying the proposed focusing structures, an important approximation can be made to simplify the analytic complexity of the problem. When the thickness of a metal film is significantly larger than its skin depth ($\delta = \frac{2}{\alpha} = \frac{c}{\kappa\omega}$ [182]) then the film can be considered to be semi-infinite [100, 183, 184]. Hence, using the visible wavelength λ_0 =633 nm, where gold will have a skin depth $\delta \approx$30 nm, is a good approximation for a semi-infinite slab. Therefore, all further analytical work in this section will use this approximation to simplify solutions.

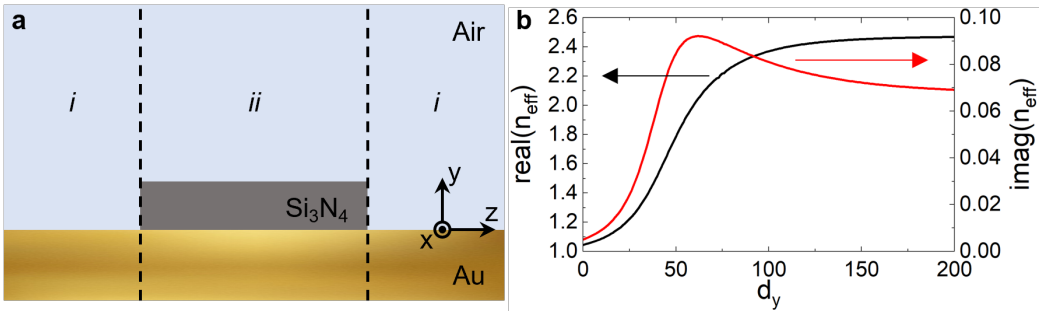

Fig. 3.1 (a) 2D schematic representation of the proposed 3D structure on the yz-plane. SPPs propagate along the air-Au interface in the positive z-direction. The structure consists of a 250nm thick gold (Au) film, with a dispersive refractive index, and a 3D dielectric (Si_3N_4) shape positioned on the Au surface, creating two regions for SPP propagation.(b) The effective refractive index of Au-Si_3N_4-air as the thickness of the Si_3N_4 increases. Both the real(black) and imaginary (red) components are shown.

To evaluate the SPP properties in the two district regions, the refractive index is calculated from their respective effective propagation constants using Eq. (1.15) and 1.17. The effective refractive index is then found using the ratio:

$$n_{eff} = \frac{\beta_{eff}}{k_0} \tag{3.1}$$

where $k_0 = \frac{\lambda_0}{2\pi}$. By doing this, the effective refractive index in region i at λ_0 =633 nm will be $n_{SPP,i} = 1.045 + i0.0005$, and the effective refractive index of region ii, $n_{SPP,ii}$ will vary with the height of the Si_3N_4 slab, as shown in Fig. 3.1b.

3.2 Plasmonic Lens Maker Equation

The *lens makers equation*, as explored in Section 1.1.2, has been a powerful tool in the design of refractive elements. It has been applied to produce many different diverging and converging lens profiles, such as planar-concave/convex, bi-concave/convex and both positive and negative meniscus lenses, operating across different wavelength regimes from microwaves [33] to optical wavelengths [28, 185]. However, despite its success in classical optics, the *lens makers equation* has not been adapted for use with SPPs. Therefore, as the propagation properties of SPPs in the region *i* and *ii*, shown in Fig. 3.1a, are determined or can be obtained through the selection of a dielectric thickness, respectively, the *lens makers equation* can be reformulated to account for the effective media in SPP structures. A schematic representation of the adapted *lens maker equation* is shown in Fig. 3.2a. The SPP adapted *lens maker equation* [34] is mathematically defined as follows:

$$\frac{1}{EFL} = (\phi - 1)\left(\frac{1}{R_1} - \frac{1}{R_2} + \frac{(\phi - 1)d}{\mathbb{R}e\{n_{SPP,ii}\}R_1R_2}\right) \tag{3.2}$$

where EFL represents the effective focal length (the distance between the maximum of the power enchantment and the principle plane of the lens), $\Phi = \frac{\mathbb{R}e\{n_{SPP,ii}\}}{\mathbb{R}e\{n_{SPP,i}\}}$ denotes the ratio between the real part of the effective refractive index of SPPs travelling in region *ii* (IIM) and region *i* (IM), R_1 and R_2 are the radii of curvature of the input (left) and output (right) surfaces of the lens in Fig. 3.2, respectively, and d is the thickness of the lens at the middle of the lens on the surface of the metal ($x = y = 0$) along the direction of propagation (z) . As discussed in Section 1.1.2, simplified versions of the *lens maker equation* exist when the lens is in free space and cannot be considered as a *thin* lens [32]. However, in the cases discussed here, outside the plasmonic lens is an IM region so the refractive index of the region *i*, $\mathrm{Re}(n_{\mathrm{SPP},i}) \neq 1$. Hence, the full ratio $\phi = \frac{\mathrm{Re}(n_{\mathrm{SPP},2})}{\mathrm{Re}(n_{\mathrm{SPP},1})}$ is considered in Fig. 3.2. Then as meniscus profiles usually have R_1 and R_2 values of the same order as the lens thickness the full adapted *lens maker equation* is used.

For this study, a fixed value for the EFL of $2\lambda_0$ will be considered, and therefore the parameters R_1, R_2, t, and $n_{SPP,ii}$ will need to be defined, as for this plasmonic configuration $n_{SPP,i}$ is already known. This study seeks to evaluate the performance of a converging plasmonic positive meniscus lens so that both R_1 and R_2 need to be positive. By rearranging Eq. (3.2) for R_2 these conditions can be explored, as follows [34]:

$$R_2 = \frac{-\mathbb{R}e\{n_{SPP,ii}\}\Phi\mathrm{EFL}R_1 + \mathbb{R}e\{n_{SPP,ii}\}\Phi\mathrm{EFL}R_1 + \Phi^2 t\mathrm{EFL} - 2\Phi t\mathrm{EFL} + t\mathrm{EFL}R_1}{\mathbb{R}e\{n_{SPP,ii}\}(\mathrm{EFL} + R_1 - \Phi\mathrm{EFL})} \tag{3.3}$$

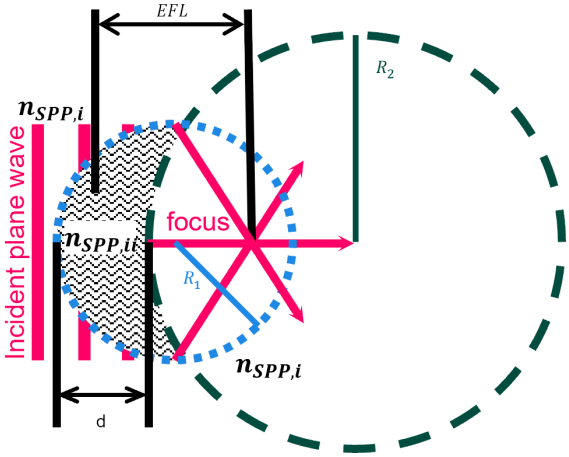

Fig. 3.2 Schematic representation of the *lens maker equation* adapted for plasmonics

When R_1 is varied with mesoscale values and the values of $\mathbb{R}e\{n_{SPP,ii}\}$ are chosen from Fig. 3.1b the different converging lens profiles can be seen as R_2 changes. This is shown in Fig. 3.3a, where an $EFL = 2\lambda_0$ and $t \approx 0.95\lambda_0$ (600 nm are considered fixed, and $\mathbb{R}e\{n_{SPP,i}\} = 1.045$, calculated as outlined in 3.1. In Fig. 3.3a, three distinct regions can be observed while only considering positive values of R_1, representing three possible geometries that can be designed utilising the adapted *lens maker equation*, a with the classical *lens maker equation* discussed in Section 1.1.2. When R_2 is negative, represented in Fig. 3.3a as the blue regions, the adapted *lens maker equation* will produce a bi-convex lens. Meanwhile, when R_2 is positive, the red regions in Fig. 3.3a, then a positive meniscus lens will be produced, which will be the focus of this study. A third and final profile, convex-planar, occurs when the magnitude of R_2 is no longer on the scale of R_1, with the sign convention being of little consequence. This transition of R_2 from negative values to positive values can be exploited to ascertain the minimum $\mathbb{R}e\{n_{SPP,ii}\}$ required to design a positive meniscus lens with the desired $EFL = 2\lambda_0$ for each R_1. Consider when a value of $R_1 = 2\lambda_0$ is used, extracted from the dashed line in Fig. 3.3a, shown in Fig. 3.3b. When $\mathbb{R}e\{n_{SPP,ii}\} < 2.09$ then the lens will have a negative R_2 i.e. a double convex. If $\mathbb{R}e\{n_{SPP,ii}\} \approx 2.09$ then $\pm R_2 \approx \pm\infty$ as the denominator of Eq. (3.3) approaches zero producing a convex-planar lens. Finally, to design a positive meniscus lens ($R_2 > 0$) with these parameters, a minimum value of $\mathbb{R}e\{n_{SPP,ii}\} > 2.09$ will be required.

In the next section, the adapted lens maker equation is exploited to design plasmonic lenses by selecting different values of the real effective refractive index in the region *ii* $\mathbb{R}e\{n_{SPP,ii}\}$ to produce focusing structures with different profiles. The main focus will be to study the efficacy of plasmonic positive meniscus lenses, demonstrating them as an

alternative plasmonic lens profile within the current array of plasmonic focusing geometries. To do this, the performance of the plasmonic positive meniscus lenses will be compared to a similarly sized plasmonic convex-planar lens. This comparison will be done by analysing the response of the two different profiled plasmonic lenses to comprehensively study the impact of changing the geometry, including d, of the plasmonic lenses on the focal spot generated. This will be done by evaluating the power enhancement of the generated focus, its depth of focus, and transversal spatial resolution. Furthermore, evaluation of the plasmonic meniscus lens performance will be conducted using a broadband plane wave incident on the structure, by taking the value of EFL calculated from the theoretical formulation of the adapted *lens maker equation* and comparing it to the numerically obtained value of the EFL.

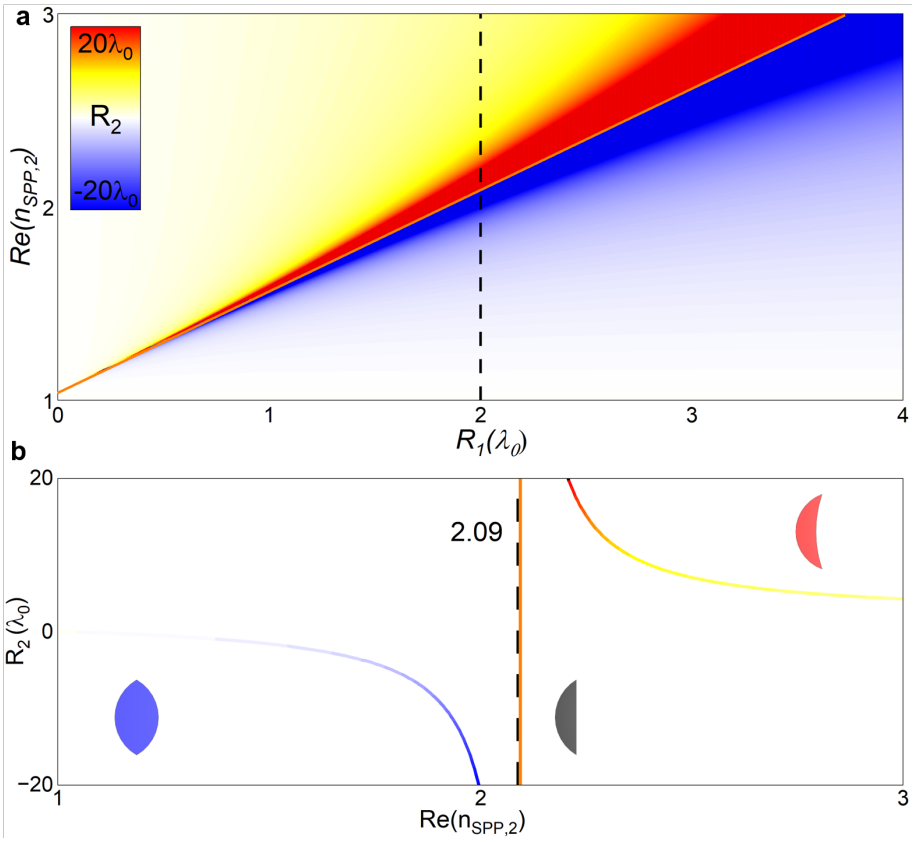

Fig. 3.3 (a) Analytically calculated values of R_2. The transition of the values from negative (blue), biconvex lens, to $\pm\infty$ (orange line), convex-planar, to positive (red), positive meniscus, as R_1 and $\mathbb{R}e\{n_{SPP,ii}\}$ vary. The black dashed line shows when $R_1 = 2\lambda_0$. (b) Value of R2 along the dashed black line in (a) considering $R_1 = 2\lambda_0$ showing the transition from negative to positive when $\mathbb{R}e\{n_{SPP,ii}\} = 2.09$, shown by the dashed orange line.

3.3 Positive meniscus vs. Convex-planar Plasmonic Lenses

Following the methodology described in Section 3.2, two different lens profiles are designed with an $EFL = 2\lambda_0$, operating at the visible wavelength of $\lambda_0 = 633$ nm. The value for R_1 is chosen to be the same as EFL, from the dashed line in Fig. 3.3a, making the maximum width of the lenses transverse to the direction of propagation of the SPPs ($x-$direction) twice the EFL. Therefore, when using these parameters $R_1 = 2\lambda_0$, the minimum $\mathbb{R}e\{n_{SPP,ii}\}$ to design a positive meniscus lens will be $\mathbb{R}e\{n_{SPP,ii}\} = 2.09$, which is marked in Fig. 3.3b as the black and orange dashed lines. However, increasing $\mathbb{R}e\{n_{SPP,ii}\}$ above this minimum will make the profile of the lens change significantly, as values of $\mathbb{R}e\{n_{SPP,ii}\}$ close to the inflection point in Fig. 3.3a,b, will require a quasi flat output surface to achieve the desired EFL due to $|R_2| >> R_1$, closely resembling a convex-planar lens rather than the positive meniscus lens desired. Meanwhile, having a value of $\mathbb{R}e\{n_{SPP,ii}\}$ that is greater than the minimum of $\mathbb{R}e\{n_{SPP,ii}\} = 2.09$ will mean the calculated values for R_2 to design the lens will become in the same order of magnitude as R_1 so it will have a significantly more curved output surface, i.e. a plasmonic positive meniscus lens.

Positive meniscus lenses have been exploited for microwave/millimeter frequencies due to their potential to have improved performance, in terms of spatial resolution and reduced aberrations, compared to similarly sized lenses [33, 186, 187]. To demonstrate if this holds in plasmonics, the different plasmonic lens profiles that have been designed using the adapted *lens maker equation* in Section 3.2, plasmonic positive meniscus lenses and plasmonic convex-planar lenses, are compared to one another. Then a further analysis of the plasmonic lenses will be done to validate the adapted *lens maker equation* in plasmonics, by using it to predict the EFL of plasmonic lenses with different properties, such as operating wavelength and $n_{SPP,ii}$. To do this the plasmonic lens profiles are implemented both as infinitely long in the out-of-plane (y) direction illuminated by a plane wave representing idealised 2D lenses, and compared with full 3D plasmonic designs illuminated by excited SPPs. Plasmonic lenses operating with SPPs exhibit similar responses to ideal 2D lenses, demonstrating that the adapted *lens maker equation* can serve as a reliable approximation for the design of plasmonic lenses. s. A 2D and 3D schematic representation of the proposed positive meniscus lenses is shown in Fig. 3.4a,b, respectively, and the proposed convex-planar lenses are shown in Fig. 3.4c,d, respectively.

Therefore, to design the two lens profiles, two complex $n_{SPP,ii}$ values need to be chosen. For the first profile, to design a positive meniscus lens in plasmonics a value of $R_2 \approx R_1$ is required meaning $n_{\mathrm{SPP},2}$ must be far away from where R_2 is close to infinity, marked by the orange line in Fig. 3.3b, so $n_{SPP,ii}$ will have to be significantly more than the minimum $\mathbb{R}e\{n_{SPP,ii}\} = 2.09$. However, as shown in Eq. (1.17) and Fig. 3.1b, the maximum value of

$\mathrm{Re}(n_{\mathrm{SPP},2})$ in a SPP device will depend on the materials used in region *ii*. In this work, using Au and Si_3N_4, the value of $\mathbb{R}e\{n_{SPP,ii}\}$ saturates as d_y approaches 200 nm with a maximum value of $\mathrm{Re}(n_{SPP,ii,sat}) \approx 2.47$. Therefore, to work below the saturation value, the Si_3N_4 dielectric height is selected to be $d_y = 126$ nm which equates to $n_{SPP,ii} = 2.43 + i0.075$. To design the second lens, a convex-planar lens, a value of $\mathrm{Re}(n_{\mathrm{SPP},2})$ close to the limit where R_2 is infinite, the orange line in Fig. 3.3b, is required. Therefore, a height of the Si_3N_4 dielectric for region *ii* is selected as $d_y = 65$ nm corresponding to $n_{\mathrm{SPP},2} = 2.09 + i0.092$. As explained previously, a lens with a perfect convex-planar profile will have a value of $R_2 = \infty$, from Eq. (3.3) and Fig. 3.3. However, in the cases presented here, R_2 will have a value which is positive and large, although not exactly infinite. Therefore, the lens is actually quasi-convex-planar, but, as R_2 is several orders of magnitude larger than R_1, from now on this design will be referred to as a convex-planar lens.

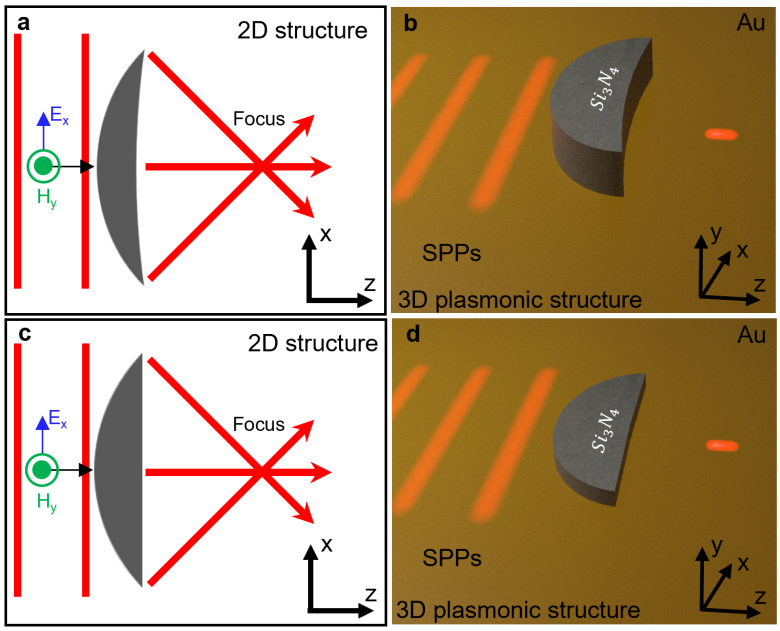

Fig. 3.4 (a) 2D and (b) 3D schematic representation of the proposed plasmonic meniscus lens. (c,d) same as (a,b) but for a plasmonic convex-planar lens.

The following sections will use these two values of $n_{\mathrm{SPP},2}$ ($n_{\mathrm{SPP},2} = 2.43 + i0.075$ and $n_{\mathrm{SPP},2} = 2.09 + i0.092$) to design positive meniscus and convex-planar lenses using Eq. (3.3) to calculate the value of the radius of curvature of the output surface, R_2, for each case. To more comprehensively study the performance of each lens, and to find the optimal configuration for both profiles, the R_2 will be calculated for different values of the centre thickness of the lenses d varying from $0.474\lambda_0$ (300 nm) to $1.264\lambda_0$ (800 nm) in steps of $0.074\lambda_0$ (50 nm), using the full adapted *lens maker equation* in Eq. (3.2) and Eq. (3.3). To evaluate the 2D and

3D plasmonic positive meniscus and convex-planar lenses designed in this way, they were numerically studied using the RF module frequency domain solver of the commercial software COMSOL Multiphysics®, for full-wave simulations (additional information is provided in Section E.2). For the 2D structures, the lenses were implemented in a rectangular box with dimensions $14.7\lambda_0 \times 49.0\lambda_0$. They were then illuminated by an incident plane wave with an out-of-plane magnetic field (polarised in the $y-$direction) by a scattering boundary condition position at the back of the lens ($-z-$direction). Scattering boundary conditions are then used in the $+z-$direction and $\pm x-$direction to reduce undesirable reflections. A fine triangular mesh is then implemented on the structure to ensure accurate results with a minimum and maximum cell size of $2.93 \times 10-4\lambda_0$ and $0.30\lambda_0$. For the 3D plasmonic simulations, a metallic cuboid slab modelled using [1] was implemented in free space with dimensions $18.4\lambda_0 \times 9.8\lambda_0 \times 0.4\lambda_0$. To excite SPPs on the metal-dielectric interface, propagating in the $z-$direction and polarised in the $x-$direction, an incident field was applied by scattering boundary conditions under 4 slits in the slab. The slits ($0.18\lambda_0$) span the width of the slab and are placed periodically in the $z-$direction every $0.61\lambda_0$.To avoid undesirable reflections scattering boundary conditions are implemented on the $\pm x-, y-, z-$boundaries. Finally, a triangular mesh with a minimum and maximum cell size of $2.22 \times 10-2\lambda_0$ and $0.47\lambda_0$, respectively, was implemented to ensure accurate results.

3.3.1 Performance evaluation in terms of power enhancement

The two lenses designed in the previous section are considered in two configurations. The first uses the lenses in a 2D scenario illuminated with a plane wave, with the electric field polarised along the $x-$axis and propagating along the $z-$axis. Then the second scenario is a full 3D study with SPPs propagating along the $z-$axis incident on the plasmonic lenses. In the latter 3D scenario, the SPPs will propagate through the two regions shown in Fig. 3.1a; the background medium in region *i*, air-Au region, will have $n_{SPP,i} = 1.045 + i0.005$ while the plasmonic lens in region *ii*, air-Si_3N_4-Au, will have $n_{SPP,ii} = 2.43 + i0.075$ and $n_{SPP,ii} = 2.09 + i0.092$ for the positive meniscus and convex-planar designs, respectively. A 3D schematic representation of the positive meniscus and convex-planar plasmonic lenses are shown in Fig. 3.4b,d. To compare the 2D cases illuminated with a plane wave to the 3D plasmonic lenses the background and lens regions will be assigned the same values as $n_{SPP,i}$ and $n_{SPP,ii}$, respectively. Schematic representation of the 2D positive meniscus and convex-planar lenses is shown in Fig. 3.4a,c, respectively.

Using these 2D and 3D configurations for the two lens profiles, the power enhancement on the surface of the metal ($y = 0$) at the centre of the lens ($x = 0$) along the direction of propagation ($z - axis$) is calculated and shown in Fig. 3.5 as a function of d. The blue lines

in Fig. 3.5 represent the input and output surfaces at $z = 0$ and $z = d$, respectively, when $x = y = 0$, for all the designed lenses to guide the eye. The ideal 2D lenses are shown in Fig. 3.5a,c and the 3D plasmonic lenses are shown in Fig. 3.5b,d, with the positive meniscus profile and planar-convex lenses in Fig. 3.5a,b and Fig. 3.5c,d respectively. As d is changing for each of the lenses, the value of R2 is recalculated using Eq. (3.3) for every value of d.

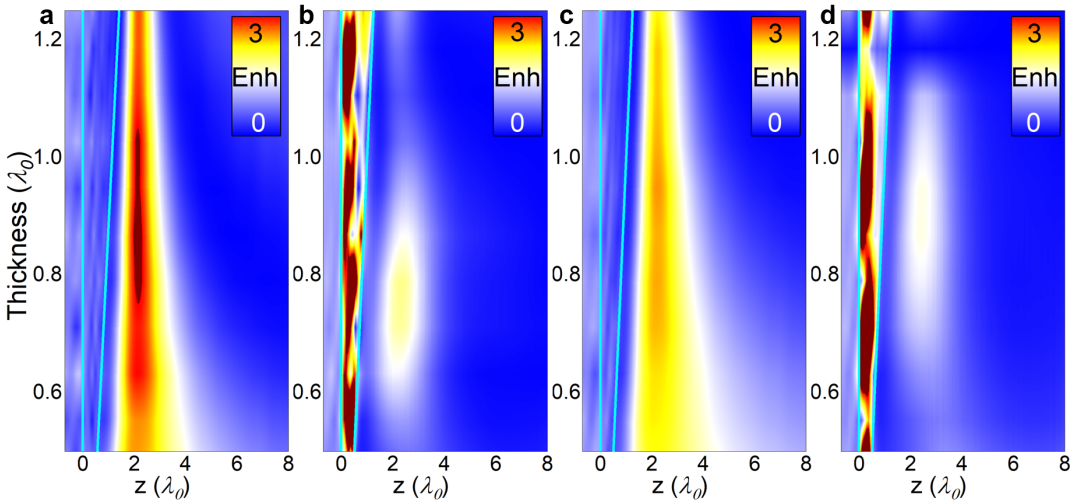

Fig. 3.5 Power enhancement at the centre of (x = 0) of a positive meniscus lens on the metal surface ($y = 0$) (a) in 2D idealised and (b) 3D plasmonic configurations. (g),(h) The same as (a),(b) but for a positive convex-planar lens. A range of thicknesses (d) at the centre of the lenses is shown. Please not that the aspect ratio for the scales in the $x-$ and $y-$directions shown in (a)-(d) do not spatially match to better show the performance of the lenses as d is varied.

In Fig. 3.5, a clear focus (red/yellow/white regions on the right of the diagonal cyan lines) is observed for both the meniscus and convex-planer lenses in the 2D and 3D configurations, although the properties of focus are dependent on the thickness of the lens. When considering the 3D plasmonic cases as d varies as shown Fig. 3.5b,d a clear focus is only observed for particular values of $0.6\lambda_0 < d < 1.1\lambda_0$. There is likely no clear focus that occurs outside of these values as above this region the lenses are too thick, suffering greater losses due to the extended spatial propagation within the lens, or they are too thin to properly redirect the incident SPPs to the focal spot, mainly working via diffraction. However, for both the positive meniscus and convex-planar lenses in the 2D configuration, shown in Fig. 3.5a,c, a focus is generated regardless of the lens thickness. However, when the thickness of the lens is $d < 0.75\lambda_0$ the power enhancement of the focus is reduced as it becomes elongated. This elongation of the focus may be a result of the thickness of the lens not being great enough,

causing the generated focus to arise due to diffraction at the edges of the lens rather than refraction through the lens, similar to the thin ($d < 0.6\lambda_0$) 3D plasmonic lenses.

The performance of the positive meniscus lenses and the convex-planar lenses can then be compared to one another in terms of their power enhancement. In both the 2D idealised cases, shown in Fig. 3.6a,c, and the realistic 3D plasmonic simulations, Fig. 3.6b,d, the power enhancement is improved when using a positive meniscus profile (Fig. 3.6a,b) rather than a convex-planar lens (Fig. 3.6c,d). Direct comparisons of the power enhancement on the focal plane, which for the cases shown in this work is the $xz-$plane at $y = 0$, for each geometry with thicknesses of 500 nm, 600 nm and 700 nm, are shown in Fig. 3.6(i-ii), respectively. From this, the best-performing thicknesses for each profile can be observed where the positive meniscus had its highest power enhancement of 3.14 and 1.83 when $d \approx 0.79\lambda_0$ (500 nm) for the 2D and 3D plasmonic configurations, shown in Fig. 3.6a,b(i), respectively. Meanwhile, the convex-planar lenses achieved maximum power enhancement of 2.57 and 1.57 when $d \approx 0.95\lambda_0$ for the 2D and 3D plasmonic configurations, shown in Fig. 3.6c,d(ii), respectively. The improved performance of the positive meniscus lenses compared to the convex-planar lenses is a result of the output surface of the lens having significant curvature allowing more output angles of the SPPs to be refracted toward the focus.

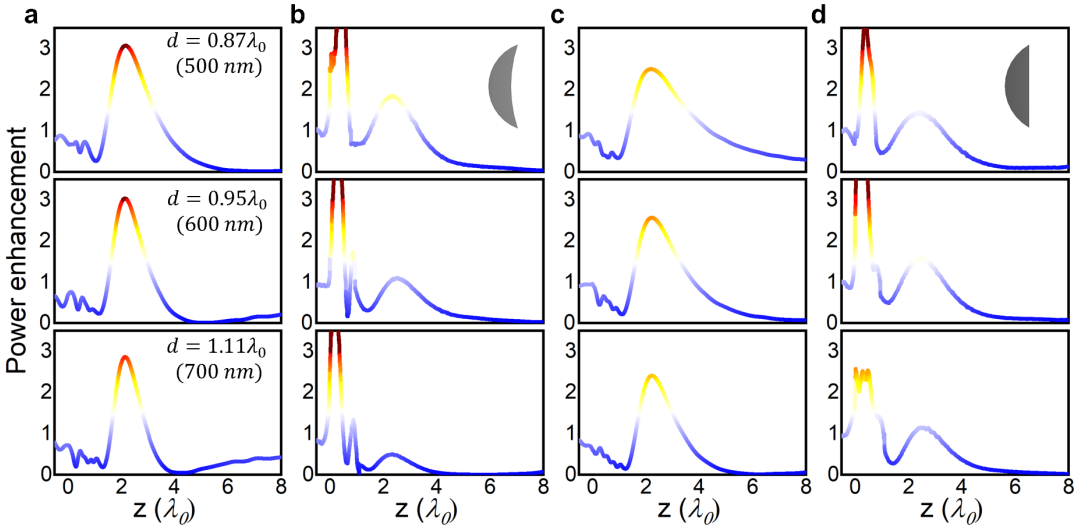

Fig. 3.6 Power enhancement at the centre of ($x = 0$) a positive meniscus lens (a) in 2D and (b) 3D plasmonic configurations and convex-planar lens (c) in 2D and (d) 3D plasmonic configurations at the surface of the metal ($y = 0$) for thicknesses $0.87\lambda_0$, $0.95\lambda_0$ and $1.11\lambda_0$.

Another interesting observation is that the positive meniscus lenses in both 2D and 3D configurations perform better with a reduced thickness at the centre of the lens compared to the convex-planar lenses, offering the possibility to design more compact devices. Next, the

position of the focus is evaluated to determine if it agrees with the designed value which in the case of the designed lenses here is of $EFL = 2\lambda_0$.

3.3.2 Evaluation of the EFL and DoF

Using the power enhancements along the $z-$axis at $x = y = 0$, shown in Fig. 3.6, the EFL for the positive meniscus lens and the convex-planar lens are calculated and shown in Fig. 3.7a,b, respectively, for the 2D structures illuminated by a plane wave (red) and the 3D case using SPPs (blue). From Fig. 3.7a,b, the similarities between the EFL of the ideal 2D cases and the plasmonic structures, illuminated by a plane wave and SPPs, can be seen. For instance, the positive meniscus, shown in Fig. 3.7a, has an EFL of $1.75\lambda_0$ and $2.13\lambda_0$ for the 2D case using a plane wave and the 3D plasmonic case, respectively, when $d \approx 0.95\lambda_0$ (600 nm), while the 2D and 3D configurations for the convex-planar lenses haves values of $1.75\lambda_0$ and $1.97\lambda_0$, respectively. The focuses generated by the lenses are likely slightly closer to the lens due to the effect of losses which are not considered in the adapted *lens maker equation*.

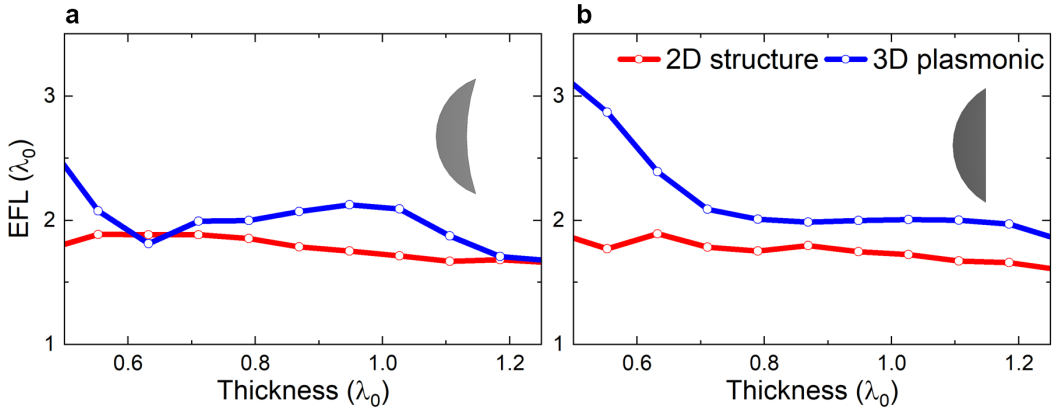

Fig. 3.7 EFL of the (a) positive meniscus lens and (b) convex-planar lens in 2D idealised (red) and 3D plasmonic (blue) configurations.

Another indicator of the performance of a generated focus is the depth of focus (DoF) (distance for the maximum power enhancement at the EFL to decayed to half in the propagation direction along the $z-$axis [18]). The DoF of the meniscus lenses and the convex-planar lenses from Fig. 3.5 are shown in Fig. 3.8a,b, respectively, for the 2D structures illuminated by a plane wave (red) and the 3D case using SPPs (blue). The results from Fig. 3.7 and Fig. 3.8 demonstrate that the expected results from the ideal 2D lenses illuminated with a plane wave agree well with the results using 3D plasmonic lenses. From Fig. 3.8, one can quantifiably observe the elongation described in Fig. 3.5. As thicker lenses are better at redirecting SPPs towards the desired focal point from more extreme positions along the $x-$axis

(larger output angles) the Dof is observed to decrease as d gets thicker, as the focal spot is reduced in the direction of propagation. This trend is observed for the two lens geometries in both the 2D and 3D configurations. When d has values between $0.5\lambda_0$ and $0.95\lambda_0$, the positive meniscus lenses in both 3D plasmonic and 2D configurations have values of the DoF that vary from $\approx 3.5\lambda_0$ to $\approx 1.3\lambda_0$ and $\approx 3\lambda_0$ to $\approx 1.82\lambda_0$, respectively. Meanwhile, in the same range of d the convex-planar lenses in 3D and 2D configurations have values of Dof that vary from $\approx 4.5\lambda_0$ to $\approx 2.03\lambda_0$ and $\approx 5.3\lambda_0$ to $\approx 1.9\lambda_0$, respectively.

Again, from these results, the meniscus lenses show an improved performance compared to the convex-planar lenses under 2D plane wave illumination and 3D structures using SPPs in terms of DoF. For example, the meniscus lens has a DoF $= 1.72\lambda_0$ and DoF $= 1.13\lambda_0$ for the 3D and 2D configurations, respectively, whereas the convex-planar lenses have DoF $= 1.92\lambda_0$ and DoF $= 1.54\lambda_0$, respectively, showing that the focal spot produced by meniscus lenses is smaller in the direction of propagation than the focus produced by a convex-planar lens. The results shown here are expected due to the curvature of the output surface (R_2), as described in Section 3.3.1.

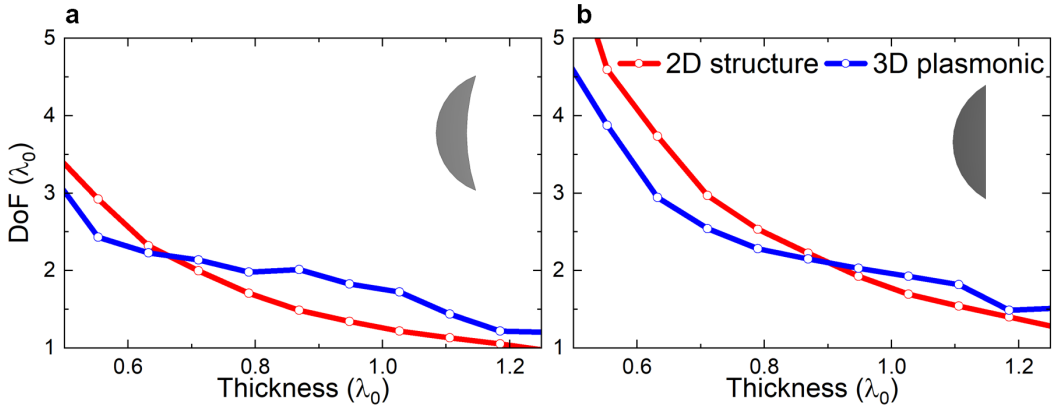

Fig. 3.8 DoF of the (a) positive meniscus lens and (b) convex-planar lens in 2D idealised (red) and 3D plasmonic (blue) configurations.

3.3.3 Comparison of the transverse spatial resolution

When evaluating the performance of focusing structures one of the most important properties to consider is the transversal spatial resolution of the focus by calculating the FWHM on the focal plane. To ensure a fair comparison between the two geometries, the lenses are designed with the thickness that corresponds to the maximum power enhancement at their EFL from Fig. 3.5. Therefore, $d = 0.79\lambda_0$ (500 nm) will be used for the meniscus lens profiles while for the convex-planar lens profile will have $d = 0.95\lambda_0$ (600 nm). These two values of d

for the meniscus and convex-planar geometries also produce a focus at a similar position, $EFL = 1.99916\lambda_0$ and $EFL = 1.99905\lambda_0$, respectively, avoiding misleading comparisons of the transversal spatial resolution as one would expect the properties of the focal spot to vary for significant differences in the EFL [146].

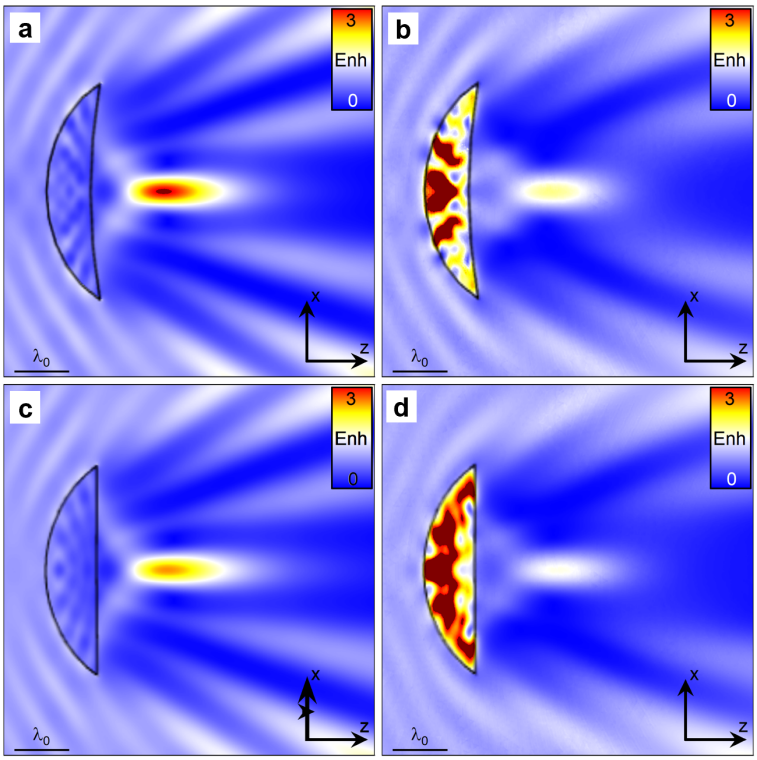

Fig. 3.9 Power enhancement on the $xz-$plane at $y = 0$ of (a,b) a positive meniscus and (c,d) convex-planar lenses in (a,c) a 2D idealised and (b,d) a 3D plasmonic configuration

Using these thicknesses to design the lens profiles, the numerical results of the power enhancement on the focal plane produced the positive meniscus lens profile, with $n_{SPP,ii} = 2.43 + i0.075$, considering the 2D idealised structures and the 3D plasmonic lens is shown in Fig. 3.9a,b, respectively, while the power enhancement results for the convex-planar lenses, where $n_{SPP,ii} = 2.09 + i0.092$ are shown in Fig. 3.9c,d, respectively. From Fig. 3.9, it can be observed that comparing the focal spots produced by the 2D idealised lenses and the 3D plasmonic lenses are similar, as one would expect. However, the 3D realistic plasmonic lenses have a clear reduction in the power enhancement of the focus compared to the 2D idealised lens, as seen in Fig. 3.5.

Several factors will cause this reduction in the power enhancement, but the primary reason is the different illumination types used. This is due to the increased losses expected when using realistic 3D models using SPPs rather than a plane wave in the 2D idealised cases. Other

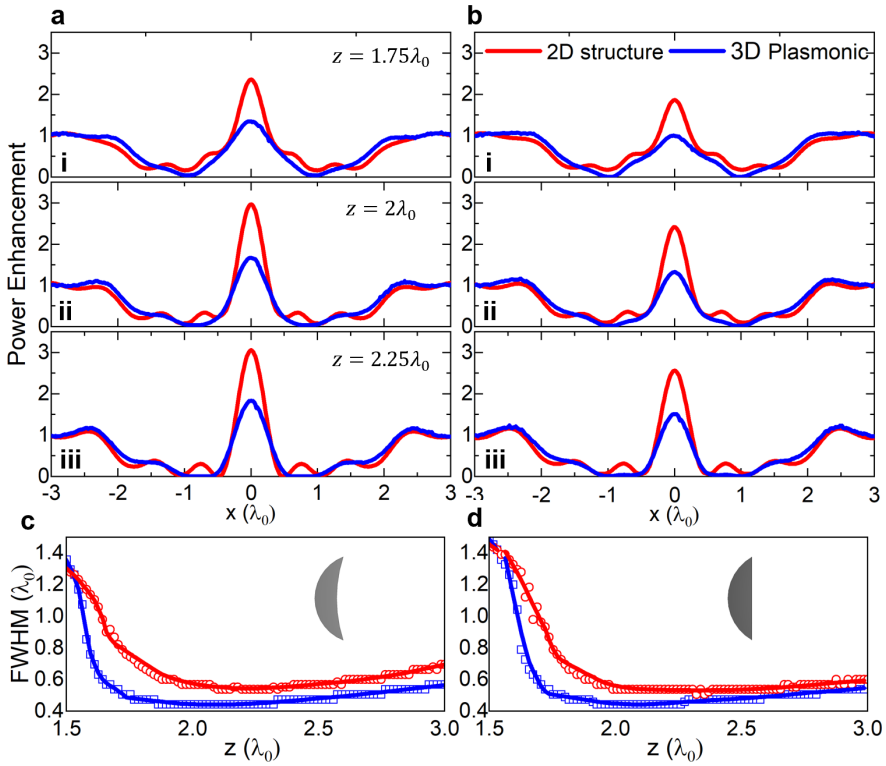

Fig. 3.10 Power enhancement generated by a (a) positive meniscus lens and (b) a convex-planar lens along the $x-$axis at three potions along the $z-$axis: (i) $z = 1.75\lambda_0$, (ii) $z = 2\lambda_0$, and (iii) $z = 2.25\lambda_0$. FWHM of the focus produced by a (c) positive meniscus lens and (d) a convex-planar lens for positions along the $z-$axis. The power enhancement and FWHM are determined for both 2D (red) and 3D plasmonic (blue) numerical simulations.

possible improvements could be made to the focusing structures as there is scattering for all of the lens geometries reducing the maximum potential power enhancement. This is a result of the abrupt change of the refractive index as the plane wave or SPPs go from propagating in the background medium ($n_{SPP,i} = 1.045 + i0.005$) into the lens ($n_{SPP,ii} = 2.09 + i0.092$ and $n_{SPP,ii} = 2.43 + i0.075$). This could be reduced by exploiting concepts of gradient index materials [188, 189]. To implement these concepts in the 2D case different materials with increasing real values of refractive index would need to be added to the back of the lens to make a step refractive index between the background media and the lens. In the 3D plasmonic case though, Fig. 3.1b can be exploited by making a stepped refractive index at the back of the lens by using different values of the height of Si_3N_4.

Using the power enhancement on the focal plane, shown in Fig. 3.9, the spatial resolution along the transverse axis of the positive meniscus and the convex-planar lenses can be compared. The power enhancement along the $x-$axis for positive meniscus and the convex-planar geometries at three unique positions along the direction of propagation, $z = 1.75\lambda_0$, $z = 2\lambda_0$ and $z = 2.25\lambda_0$ are shown in Fig. 3.10a,b, respectively, in both the 2D ideal (red) and 3D plasmonic (blue) configurations. As expected from Fig. 3.5, the 2D idealised cases have higher power enhancement compared to the 3D plasmonic configurations. It is clear when comparing the power enhancement along the $x-$axis at each position in the direction of propagation the power enhancement at $x = 0$ produced by the meniscus lens profile for both the 2D idealised and 3D plasmonic configurations is increased compared to the convex-planar geometries.

Further analysis of the spatial resolution of the focal spot is conducted by obtaining the FWHM of the power enhancement along the $x-$axis, shown in Fig. 3.9, at positions along the $z-$axis from $z = 1.5\lambda_0$ to $z = 2.5\lambda_0$ in steps of $0.0158\lambda_0$ for the meniscus and convex-planar geometries are shown in Fig. 3.10c,d, respectively, for the 2D ideal (red) and 3D plasmonic (blue) configurations. From this, the transversal spatial resolution is observed to be similar between the two designs in both configurations. For the 2D and 3D plasmonic structures the positive meniscus lens, shown in Fig. 3.10c, and the convex-planar lens, shown in Fig. 3.10d, each have a FWHM at their respective focal point of $0.44\lambda_0$ and $0.54\lambda_0$, respectively. This is likely a result of the adapted *lens maker equation* being a classical optics method. Therefore, the lenses produced in this way will be diffraction-limited, so as the spatial resolution of these lenses approaches this limit they have the same FWHM although the meniscus lens generates a higher power enhancement.

3.3.4 Broadband response

The next study was conducted to evaluate the broadband performance of the plasmonic meniscus lens designed and evaluated in previous sections. As it is known, both Au and Si_3N_3 are dispersive at the frequency range under study. Therefore, the effective refractive index ($n_{SPP,i}$ and $n_{SPP,ii}$) in the two regions where the SPPs propagate (Au-air region *i* and the Au-Si_3N_3-air region *ii*) will change too, according to Eq. (1.17). This will cause the focal spot generated by a plasmonic meniscus lens to shift and change. This is a phenomenon, known as chromatic aberration [190], due to the dispersive nature of materials. Therefore, this is often observed when working with structures, such as lenses designed using the *lens maker equation*, and broadband/polychromatic EM waves. However, if the parameters of a plasmonic meniscus lens designed using Eq. (3.2) are known, then the position of the focal spot at a different wavelength can be predicted, using newly calculated values of $n_{SPP,i}$, $n_{SPP,ii}$ and Eq. (3.2). A comprehensive study of the lens can then be done by comparing these predicted analytically calculated positions to the obtained EFL from the same numerically simulated lenses. Therefore, an initial plasmonic meniscus lens is designed at the same visible wavelength $\lambda_0 = 633\,\text{nm}$ as the previous sections with the same parameters. The $EFL = 2\lambda_0 = 1266\,\text{nm}$ was chosen at this wavelength, with $R_1 = EFL = 1266\,\text{nm}$. The effective refractive index in the Au-air region *i* and the Au-Si_3N_3-air region *ii* will be the same as in Section 3.3, $n_{SPP,i} = 1.045 + i0.005$ and $n_{SPP,ii} = 2.43 + i0.075$, respectively, which can then be used to calculate the ratio ϕ in Eq. (3.2). As these are the same parameters as in Section 3.3.1, the best performing lens thickness $d = 500\,\text{nm}$ was chosen which resulting in an $R_2 = 4046\,\text{nm}$ when using Eq. (3.3). The profile of a plasmonic meniscus lens was then generated using these parameters and its broadband response is evaluated both analytically, using Eq. (3.2), and numerically within the spectral range of 550 nm to 750 nm.

The value of the EFL of the plasmonic meniscus lens, obtained from analytical calculations (red) and numerical simulations (blue), as the wavelength changes within this spectral range are shown in Fig. 3.11. As observed, there are three distinct regions of the broadband response when comparing the analytical and numerical results. When the operational wavelength is below 600 nm, in the range 550 nm to 600 nm, marked as the green region in Fig. 3.11, the EFL obtained from the numerical simulations are larger than the analytically calculated values. This is a result of more losses experienced by the SPPs when the operational wavelength is reduced, as expected from [100, 188]. This is expected, as the *lens maker equation* only considers materials without losses, so as the effect of losses increases the deviation between the EFL from the numerical simulations and the analytical calculations also increases. This could be addressed by developing a further adapted *lens maker equation* to consider a complex refractive index in the regions *i* and *ii* in the future.

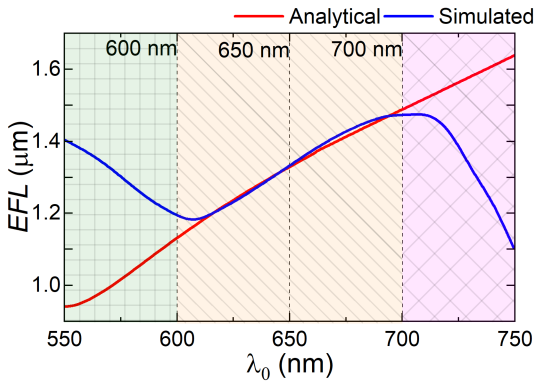

Fig. 3.11 EFL calculated analytically (red) and numerically (blue) as the incident wavelength used to illuminate a 3D plasmonic meniscus lens varies designed with parameters: $R_1 = 1266\,\text{nm}$, $R_2 = 4046\,\text{nm}$, $d = 500\,\text{nm}$, and an $EFL = 1266\,\text{nm}$. Green region ($500\,\text{nm} < \lambda < 600\,\text{nm}$) represents a wavelength band where the plasmonic meniscus lens experiences high losses, the orange region ($600\,\text{nm} < \lambda < 700\,\text{nm}$) represents when the plasmonic meniscus lens behaves as expected, and the purple region ($700\,\text{nm} < \lambda < 750\,\text{nm}$) represents where the SPPs focused by the plasmonic meniscus lens are weakly coupled to the metal-dielectric interface.

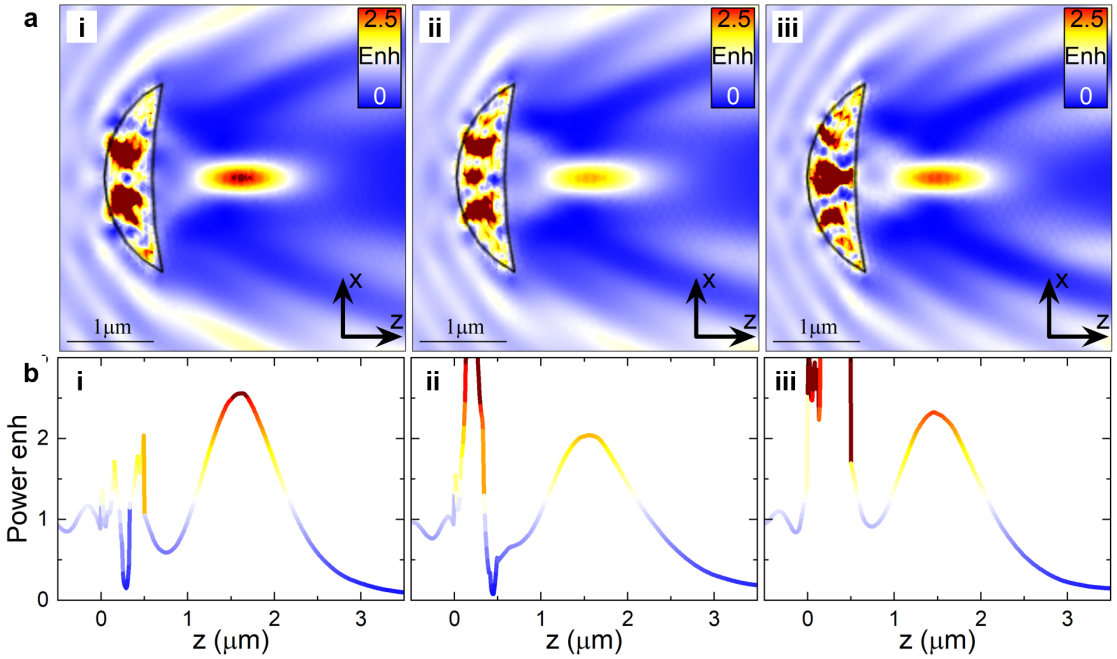

Fig. 3.12 (a) Power enhancement focal plane for the plasmonic meniscus lens described previously when illuminated by a wavelength of (i) 600 nm (ii) 650 nm and (ii) 700 nm. (b) Power enhancement on the focal plane at the centre of the lens ($x = 0$) for a wavelength of (i) 600 nm (ii) 650 nm and (ii) 700 nm along the z-direction.

Then in the range of wavelengths between 600 nm and 700 nm, marked as the orange region in Fig. 3.11, there is a good agreement between the numerical and the theoretically calculated EFL as the plasmonic meniscus lens behaves as predicted by the adapted *lens maker equation*. Above this, in the wavelength range between 700 nm to 750 nm, marked as the purple region in Fig. 3.11, the values of the EFL obtained from the numerical simulations are smaller than the analytically calculated values, with greater deviation as the wavelength increases. This deviation is a result of the adapted *lens maker equation* considering the perfect coupling of the SPPs to the dielectric-metal interface, whereas the evanescent confinement of SPPs will be reduced as the operational wavelength increases [191, 113].

To corroborate the results shown in Fig. 3.11, the power enhancement on the focal plane of the plasmonic positive meniscus lenses when they are illuminated by 3 wavelengths, $\lambda_0 =$ 600 nm, 650 nm and 700 nm, marked by dashed lines in Fig. 3.11, are shown in Fig. 3.12a(i-iii), respectively, with the power enhancement in the direction of propagation at the centre of the lens ($x = 0$) extracted in Fig. 3.12b(i-iii), respectively. From this, the EFL for these three wavelengths was found to be 1.19 µm, 1.33 µm and 1.47 µm, respectively, for the numerical simulations while the analytical EFL had value of 1.13 µm, 1.33 µm and 1.49 µm. Therefore, from these results, the plasmonic meniscus lenses behave as expected within a broadband spectral region of 600 nm to 700 nm leads to the conclusion that modifying the *lens maker equation* to be used in SPPs to design plasmonic lenses is effective as long as the intrinsic losses of the plasmonic structure are not too high and the SPPs are strongly confined to the metal-dielectric interface.

3.3.5 Plasmonic meniscus lens under Oblique Illumination

In this study, the plasmonic meniscus lens designed and discussed in Section 3.3.4 ($\lambda_0 =$ 633 nm, $EFL = 2\lambda_0 = 1266$ nm, $R_1 = EFL = 1266$ nm, $n_{SPP,i} = 1.045 + i0.005$, $n_{SPP,ii} =$ $2.43 + i0.075$, $d = 500$ nm and $R_2 = 4046$ nm) is evaluated when illuminated under oblique incidence. To do this, the plasmonic lens was rotated from the middle of its output surface from 0° (the lens position for all the other studies) to 30° in steps of 3°. A schematic presentation of this rotation of the plasmonic meniscus in steps of 6° is shown in Fig. 3.13a(i-vi) with the power enhancement on the focal plane at the position of the focus is shown in Fig. 3.13b(i-vi). From this, the focus produced by the rotating plasmonic meniscus lens can be seen to shift in both the $x-$ and $z-axis$ while the power enhancement decreases as the angle the lens is rotated by increases. This is corroborated in Fig. 3.13c,d which show the shift in the focus in both the $x-$ and $z-$directions and the change in the power enhancement of the focus as a function of the angle, respectively. When the rotating angle is less 15° there is a small impact on the power enhancement of the focus, as shown in Fig. 3.13c,

however above 15° the power enhancement is significantly reduced to values of ≈ 1.2. Then in Fig. 3.13d, the position of the focus shows an almost linear shift in the position of the focus along both the $x-$ and $z-$axis as the angle increases from 0° to 30° with a change of $\Delta_x = 0.35\lambda_0$ and $\Delta_z = 0.4\lambda_0$, respectively. Therefore, plasmonic meniscus lenses are shown to be robust when illuminated by oblique incidence when the angle is less than 15°.

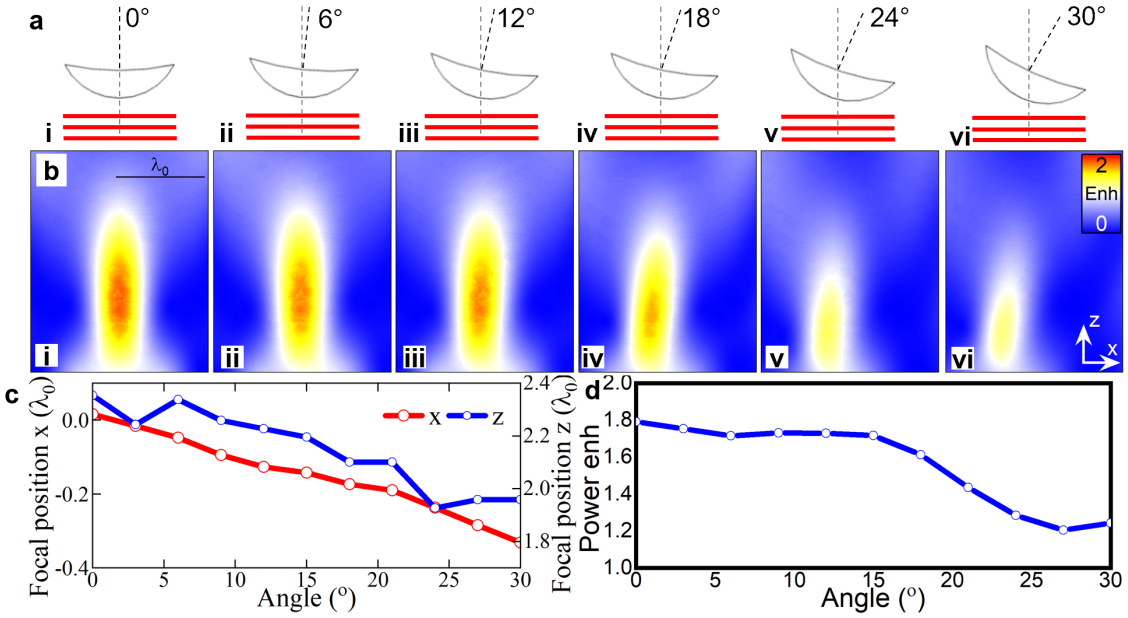

Fig. 3.13 (a) Schematic representation of the rotated plasmonic meniscus lens with angles from 0° to 30° with a step of 6°. (b) Power enhancement on the focal plane for a plasmonic meniscus lens as they are rotated with the angles in (a). (c) Focal position in x (red) and z (blue) coordinates and (d) maximum power enhancement of the plasmonic meniscus lens as the rotation angle increases from 0° to 30° in steps of 3°.

3.3.6 Effect of Fabrication Errors on plasmonic meniscus lenses

Fabrication techniques have made improvements in recent decades, showing the capabilities to reliably fabricate features in the scale of tens of nanometers [192, 64, 193]. However, despite these improvements, there are still possible fabrication errors that can occur when working at the limits of current technology. In this context, in this section, potential fabrication errors, such as "vanishing" edges or uncertainty in the dielectric dimensions, are introduced to the concept of a plasmonic meniscus lens to show their robustness despite potential errors. The studies in the following section use the same plasmonic meniscus lens as used in Section 3.3.4 and Section 3.3.5 with the parameters: $\lambda_0 = 633$ nm, $EFL = 2\lambda_0 = 1266$ nm,

$R_1 = EFL = 1266\,\text{nm}$, $n_{SPP,i} = 1.045 + i0.005$, $n_{SPP,ii} = 2.43 + i0.075$, $d = 500\,\text{nm}$and $R_2 = 4046\,\text{nm}$).

Effect of Fabrication Errors in d_y

As discussed in Section 3.3, to achieve an effective refractive index of $n_{SPP,ii} = 2.43 + i0.075$ for the plasmonic meniscus lens, the Si_3N_4 layer should have a height of 126 nm, from Fig. 3.1b. However, limitations of the fabrication techniques used to potentially fabricate a plasmonic meniscus lens may cause this dielectric layer to be slightly thinner or thicker. Therefore, the EFL is obtained using numerical simulations and analytical values from Eq. (3.2) as the height of the Si_3N_4 layer is varied from 50 nm to 200 nm in steps of 10 nm, are shown in Fig. 3.14a. In these results, a good agreement is observed between the numerically obtained and analytically calculated EFL demonstrating the robustness of the plasmonic meniscus lens to behave as predicted even with fabrication errors. For completeness, examples of the power enhancement on the focal plane when the height of the Si_3N_4 layer is $d_y = 100\,\text{nm}$, 150 nm and 200 nm are shown in Fig. 3.14b(i-iii) respectively, demonstrating that a focus is still produced even if the height of the dielectric has some minor experimental fabrication errors.

Effect of Fabrication Errors in lens thickness

Next, the impact of potential fabrication errors on the centre ($x = 0$) thickness of the lens (d) is investigated for the plasmonic meniscus lens, when the radius of curvature of the input and output surfaces are kept constant. The EFL of the plasmonic meniscus lens is calculated analytically using Eq. (3.2), and obtained from the power enhancement of numerical simulations as d varies from 300 nm ($0.47\lambda_0$) to 800 nm ($1.26\lambda_0$) in steps of 50 nm ($0.08\lambda_0$), is shown in Fig. 3.15a. A good agreement is observed between the analytical and the numerically obtained values of EFL for the cases when a focus (power enhancement > 1) is formed. The power enhancement on the focal plane is shown in Fig. 3.15b(i-iii) when the thickness of the lens is $d = 500\,\text{nm}$, 600 nm and 700 nm, respectively. From the results shown in Fig. 3.15, a focus with a power enhancement greater than 1 will be produced by the plasmonic meniscus lens at a position that can be predicted by Eq. (3.2), as long as the fabrication errors are not too significant, making the lens too thin or too thick (as explored in Section 3.3.1). Again these results show the plasmonic meniscus lens is robust to overcome potential experimental errors within reason.

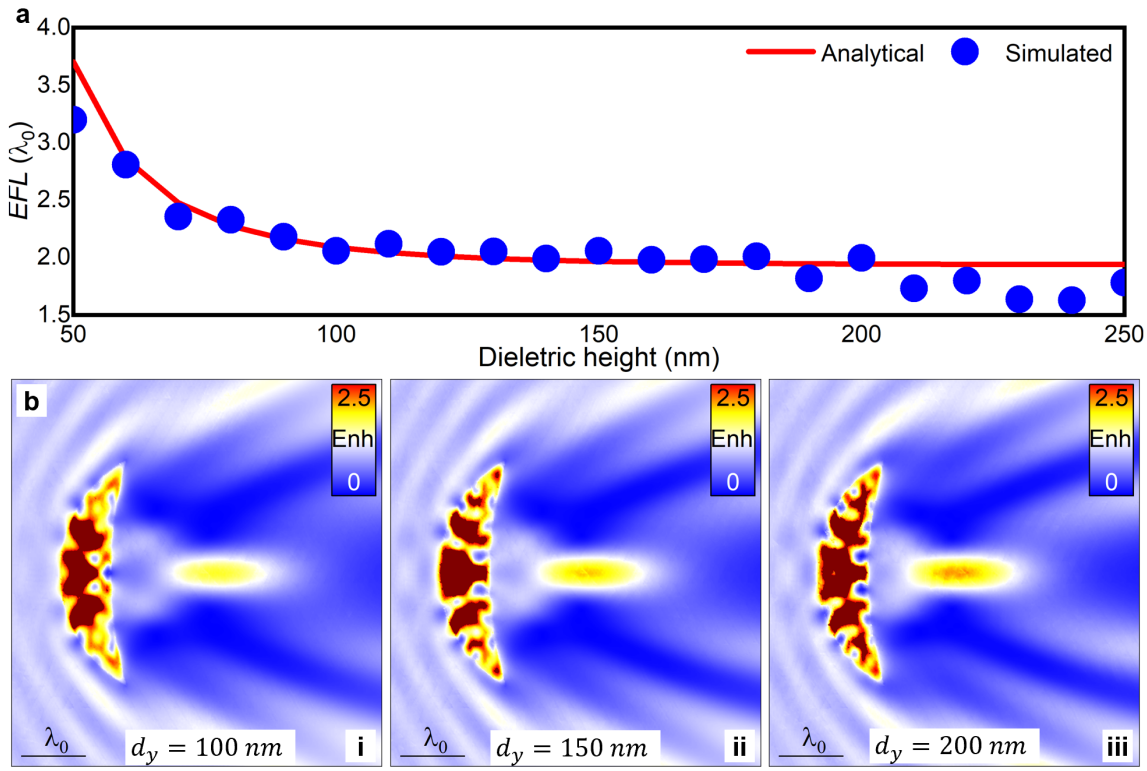

Fig. 3.14 (a) Theoretical (red) and numerical (blue) results of the EFL as a function of d_y used for the 3D plasmonic meniscus lens with parameters defined in 3.3.4, designed with a height of the Si_3N_4 layer of 126 nm to have an EFL at 1266 nm ($2\lambda_0$). Power enhancement on the focal plane for the plasmonic meniscus lenses with a dielectric height of (b) 100 nm (c) 150 nm and (d) 200 nm.

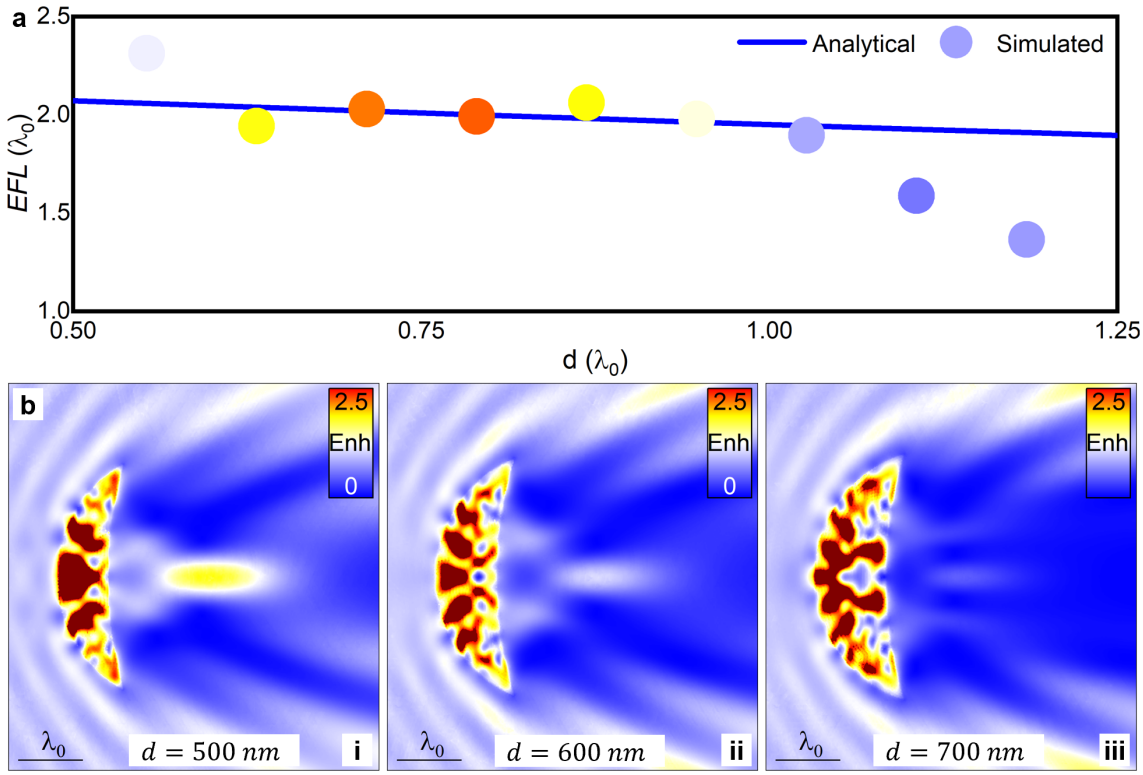

Fig. 3.15 (a) Analytically calculated (blue) and numerical (colour scaled to the power engagement of each lens thickness using the same scale bars as seen in (b-d)) results of the EFL as a function of d of the plasmonic meniscus lens at $x = 0$, designed with parameters from 3.3.4. (b) Power enhancement on the focal plane for the plasmonic meniscus lenses with (i) $d = 500$ nm, (ii) $d = 600$ nm and (iii) $d = 700$ nm

Effect of Fabrication Errors in Edge Sharpness

In this final study, the impact of fabrication errors on the sharpness of the plasmonic meniscus lens edges is explored. As the the current constraints on nanofabrication methods limit the smallest feature that can be reliably fabricated in the tens of nanometers this may cause the sharp edges at the corner of the plasmonic meniscus lens to "vanish" [194], changing the shape of the lens. Here the imperfect edges of a potential plasmonic meniscus lens are implemented replacing the sharp edges with rounded corners so there are no features smaller than 100 nm. The power enhancement on the focal plane for plasmonic meniscus lenses with rounded corners for thicknesses of 400 nm to 700 nm in steps of 100 nm, are shown in Fig. 3.16a(i-iv), respectively. In all of these cases, a clear focus is observed, even with rounded edges, although the thick lenses (700 nm) have a low power enhancement as expected from Section 3.3.1. To examine the effect of the rounded edges compared to sharp edges, the power enhancement in the direction of propagation at the centre of the lenses ($x = 0$), are shown in Fig. 3.16b(i-iv). From this, there is good agreement even when the corners are rounded, although there is a slight power enhancement reduction for smaller values of d as the rounded edges become comparable to the magnitude of d. Therefore, the results shown here and in the previous section show that plasmonic meniscus lenses are robust to many different potential fabrication errors.

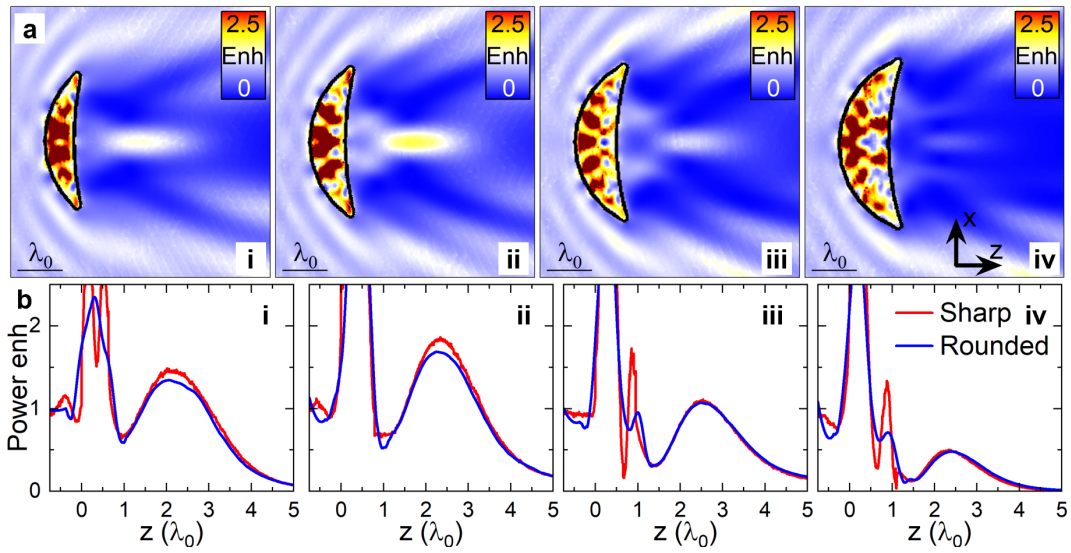

Fig. 3.16 (a) Power enhancement on the focal plane for four plasmonic meniscus lenses with no features less than 100nm thick and a thickness (i) $d = 400$ nm, (ii) $d = 500$ nm, (iii) $d = 600$ nm and (iii) $d = 700$ nm. (b) Power enhancement at the centre of a lens (x = 0) on the surface of the metal (y = 0) with sharp corners (red) and rounded edges (blue) for plasmonic meniscus lenses from panels (i-iv), respectively.

Chapter 4

From classical concepts into plasmonics: Localised surface plasmons

This chapter will concentrate on work using another important aspect of plasmonics: LSPs. LSPs arise when oscillating EM waves at optical frequencies couple with the conduction electrons within metallic nano-/micro-structures and produce non-propagating excitations, which can generate localised field hotspots (regions of high field concentration) due to resonances of the LSPs [90, 83, 195, 40, 196, 197]. A consequence of this ability to confine EM waves and produce field hotspots has led to LSPs emerging in many applications such as photocatalysis [198, 199], and optical data storage [200]. In this context, pursuing new and enhanced methods to design plasmonic nanoparticles capable of sustaining LSPs and their resonances is required to improve their performance in these many applications [43].

One area where research on LSPs in plasmonic nanostructures has demonstrated to be particularly beneficial is sensing. This has been demonstrated for surface-enhanced Raman spectroscopy [201, 202], gas and ion detection [203, 204], single particle detection [205, 101], biosensors [206, 207], in addition to the ability to calculate the EM and geometric properties of proximate dielectrics (such as the thickness of a film or its refractive index) [208, 97]. This is possible because the properties of the LSP resonances within a plasmonic structure, such as the power enhancement and spectral position [40], will be dictated by and, therefore, can be controlled through the engineering of different parameters, such as the materials used in and around the nanoparticles [93, 209–211], as well as the geometry of the particles themselves, in terms of their size and shape [212–215]. An interesting method used to exploit LSP resonances and their field hotspots has been to combine the individual resonances of nanoparticles in a method known as mode hybridisation [216–220]. This has been used in two-particle systems [221–223], see Fig. 1.11, up to entire arrays of particles [224, 101, 201]. To assist in the understanding and design of LSP nanostructures for sensing

classical antenna engineering techniques can be applied to the realm of plasmonics, such as conformal mapping [178, 225].

In this chapter, a comprehensive study of complementary plasmonic nanostructures designed using a different classical technique, the Babinet principle, is carried out using numerical studies to show how complementary responses in plasmonic nanostructures due to the Babinet principle, which confine an incident EM field at nanoscales, are exploited for sensing variations of a nearby dielectric. First, two configurations of the plasmonic nanostructures are designed: gold cylindrical particle-dimers and their complementary counterpart, plasmonic aperture-dimers in a gold film. While there is a notable lack of studies in the context of the Babinet principle, these structures offer several benefits: their plasmonic properties are well-known, they are relatively easy to fabricate without sharp edges, and their rotational symmetry aids in identifying fabrication imperfections, thereby facilitating comparisons between numerical simulations and fabricated samples. These nanostructures will be numerically evaluated to determine the complementary spectral location (using reflection and transmission spectra) and electric and magnetic field distributions of the LSP resonances of the two plasmonic nanostructures. To validate these results, experimental results from an external collaboration, employing Electron Energy Loss Spectroscopy (EELS) the distribution of the LSP modes are experimentally mapped and compared to the numerical results. After this, both complementary plasmonic nanostructures are studied to evaluate their performance when they are used as dielectric sensing devices. A dielectric is used as the analyte, and it will vary in terms of its refractive index and geometry with different configurations of the analyte, such as thin films and particles, considered. The sensing performance of the two complementary nanostructures is compared to assess the role of the Babinet principle. The interchangeable EM responses due to being complementary enable the selection of the best-performing configuration depending on the desired application. Both complementary nanostructures, demonstrate values of sensitivity in the order of hundreds of nm/RIU.

4.1 Design

The 3D schematic representation of the proposed complementary plasmonic nanostructures, consisting of cylindrical particle-dimers and cylindrical apertures-dimer in a metallic film, is shown in Fig. 4.1a,b, respectively. These nanostructures, referred to as plasmonic nanoparticles and plasmonic nanoapertures hereafter, are illuminated normally to the nanostructures by a plane wave, represented by the red arrow in Fig. 4.1. In this study, the plane wave propagates parallel to the $z-$axis, with linear polarisation along either of the $x-$ or $y-$direction of

the **E**−field, to investigate the validity of the Babinet principle. The incident plane wave has a spectrum of frequencies (f_0)/wavelengths (λ_0)/energies (E_0) in free space, ranging from $f_0/\lambda_0/E_0 = 150\,\text{THz}$ to $310\,\text{THz}$ / $2000\,\text{nm}$ to $967\,\text{nm}$ / $0.62\,\text{eV}$ to $1.28\,\text{eV}$. Changing the polarisation of the incident plane wave on the plasmonic nanostructures results in the excitation of distinct yet complementary LSP resonant modes in the plasmonic nanostructures. To observe and determine the spectral position of these LSP resonances, reflection (R) and transmission (T) values will be calculated for each plane wave, represented by the green and purple arrows labelled as R and T in Fig. 4.1, respectively.

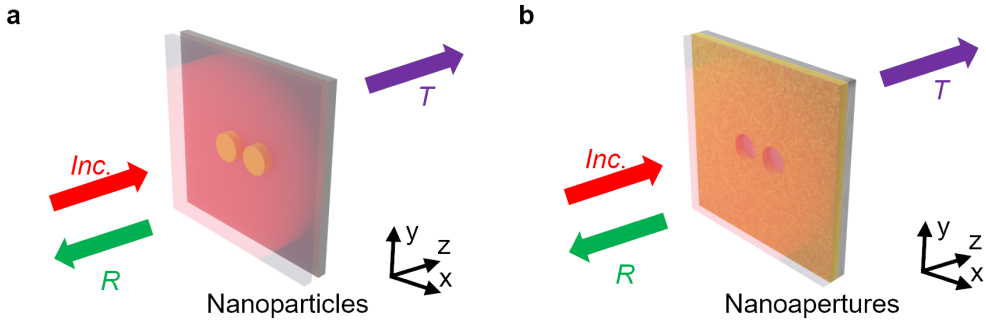

Fig. 4.1 3D Schematic representation of complementary cylindrical plasmonic (a) Au nanoparticles and (b) nanoapertures in an Au sheet, each on a Si_3N_4 substrate. Red, green and purple arrows represent the incident, reflected and transmitted plane wave, respectively

The 2D schematic representation showing the $yz-$ and $xy-$ cross-sections of the proposed complementary plasmonic nanostructures are shown in Fig. 4.2a,b for the plasmonic nanoparticles and Fig. 4.2c,d for the plasmonic nanoapertures. To adhere to the Babinet principle, which considers the complementary nanoparticles and screen where the nanoapertures are to be infinitely thin, the gold nanoparticles and film are designed to have a thickness in the direction of propagation ($z-$direction), shown in Fig. 4.2a,c, of $d_m = 30\,\text{nm}$. Thus, even at the shortest wavelength in the spectrum (967 nm-2000 nm), the layer thickness remains significantly smaller than the incident wavelength, approximately satisfying the requirement of the Babinet principle. The two complementary nanostructures are positioned on a dielectric substrate made from Si_3N_4, with the same thickness in the direction of propagation as the metal nanostructures, $d_s = 30\,\text{nm}$. As in Fig. 4.1, the incident plane wave propagates along the $z-$axis (shown as the red arrow labelled *Inc.*), polarised along the $x-$ or $y-$axis and interacts with the plasmonic nanostructures to excite LSP resonant modes, the spectral position of which will be determined by retrieving the R (green arrow) and T (purple) radiation.

To evaluate these plasmonic nanostructures as dielectric sensors, a dielectric, which will be considered as the analyte in this study, is introduced into them. In this study, the dielectric analytes considered are non-dispersive with real values of refractive index (n_a). A schematic

representation with the analyte introduced into the nanostructures is shown in Fig. 4.1 and Fig. 4.2a,c, with the analyte presented as a thin film positioned atop the gold nanostructures with a thickness along the $z-$axis of d_a. However, in this study, several configurations of the analyte will be considered, including when it is immersed into the nanostructures or presented as small particles. The geometry of the plasmonic nanoparticles and nanoapertures considered in these studies is characterised by the diameter of each dimer and the separation between the nanoparticles/nanoapertures, denoted as D and L, respectively, in Fig. 4.2b,d. As mentioned in the previous section, the spectral location of the LSP resonances will be dictated by the size and shape of the plasmonic nanostructures. Therefore, variations in the value of D and/or L will cause the frequency/wavelength of the LSP resonant mode to shift, as expected. Based on this, to ensure fair comparisons of the performance of the plasmonic nanostructures discussed in the numerical studies within the following sections, constant values of these parameters are selected as $D = 200\,\text{nm}$ and $L = 20\,\text{nm}$.

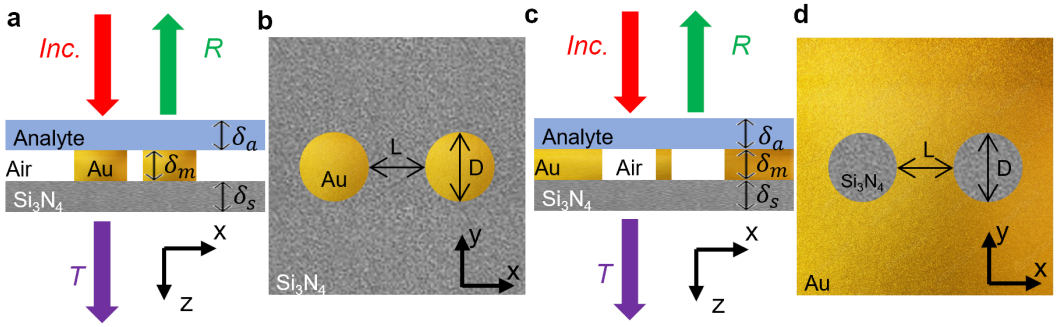

Fig. 4.2 Schematic representation of the yz- and xy-cross-sections of the proposed complementary plasmonic nanostructures: (a,b) plasmonic nanoparticles and (c,d) plasmonic nanoapertures. Red, green and purple arrows present in (a,c) represent the incident, reflected and transmitted plane wave, respectively. D and L shown in panels (b) and (d) denote the diameter of the individual cylindrical dimers and the separation between them, respectively

4.2 Complementary Plasmonic nanostructures

To evaluate the plasmonic nanostructures to validate the Babinet principle in plasmonics and their performance as dielectric sensors, they were numerically studied using the frequency domain solver of the RF module from the commercial software COMSOL Multiphysics®, for full-wave simulations (additional information is provided in Section E.2). These structures, consisting of gold nanostructures on a Si_3N_4 substrate (Fig. 4.1,4.2), were implemented into the simulations with material properties based on experimental data [1, 181], respectively. The square nanostructures have periodic boundary conditions on the $\pm x-$ and

$\pm y-$boundaries (infinitely repeating along the $z-$ and $y-$axis) with large enough lateral dimensions 950 nm $\times$ 950 nm as to minimise lattice resonances. A port is then positioned 3000 nm from the front (plasmonic nanostructure) of the structure to apply the incident plane wave [with E_x or E_y polarisation (parallel or transverse to the long axis of the plasmonic nanostructures, respectively, see Fig. 4.1,4.2] and record the reflected signal and then 3000 nm from the back (Si_3N_4 substrate) of the nanostructures to record the signal transmitted through the nanostructures. The magnitude of the signal reflected and transmitted through the plasmonic nanostructures is calculated as a function of frequency using the definition of scattering parameters (S-parameters) at the input and output ports from COMSOL Multiphysics®. The spectral position of the plasmonic nanostructures can be determined from these R and T spectra. Finally, an extremely fine tetrahedral mesh is applied to the plasmonic nanostructures with minimum and maximum element sizes of 9.38 nm and 219 nm, respectively. The mesh was further improved by applying two additional automatic refinements of the plasmonic nanostructures.

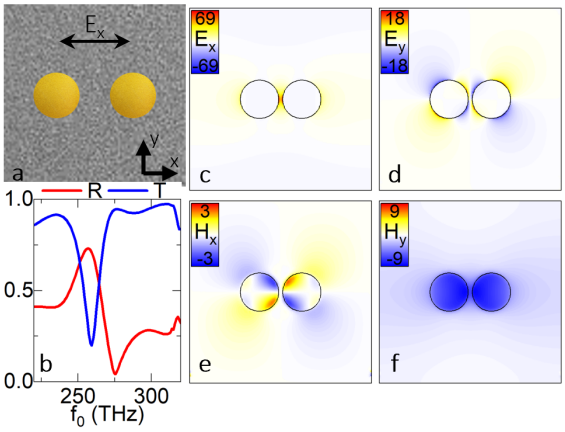

Fig. 4.3 (a) 2D schematic representation ($xy-$plane) of the proposed plasmonic nanoparticles with the direction of the linearly E_x polarised incident plane wave illuminating it shown as an arrow, (b) R (red line) and T (blue line) spectra, (c) E_x, (d) E_y, (e) H_x, and (f) H_y field enhancements of the LSP resonances. To calculate the field enhancements the ratio of the full electric or magnetic field spatial distributions and the incident excitation field is used. The sign convention of the field enhancement is obtained using the direction of the specific vectorial component.

A top view at the surface of the schematic representation of the plasmonic nanoparticles illuminated by E_x polarised plane wave and nanoapertures illuminated by E_y polarised plane wave is shown in Fig. 4.3a and Fig. 4.4a, respectively, with the direction of the linear polarisation represented by a horizontal (E_x) or vertical (E_y) arrow. The calculated R and T spectra for the plasmonic nanostructures in Fig. 4.3a and Fig. 4.4a, are shown in

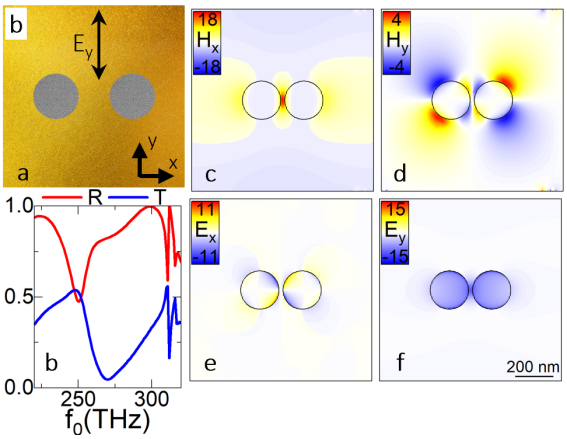

Fig. 4.4 R and T spectra and Field distributions of the plasmonic nanoapertures illuminated by an incident plane wave with E_y polarisation, respectively. (a) 2D schematic representation on the $xy-$plane with an arrow showing the direction of the linearly polarised incident plane wave illuminating them, (b) R (red line) and T (blue line) spectra, (c) H_x, (d) H_y, (e) E_x, and (f) E_y field enhancements of the LSP resonances.

Fig. 4.3b and Fig. 4.4b as red and blue lines, respectively. From these spectra, a minimum in the T spectrum of the plasmonic nanoparticles and a minimum in the R spectrum of the plasmonic nanoapertures is observed, indicating that an LSP resonant mode has been excited in the plasmonic nanostructure. As the plasmonic nanostructures are complementary and under orthogonally polarised plane wave illumination, the spectral positions of these LSP resonances are similar but not exactly the same. This slight discrepancy is a demonstration of the approximate and not complete validity of the Babinet principle in the realm of plasmonics [41, 40]. This is expected, as although d_m is significantly smaller than the incident wavelength they are not infinitely thin as required for the Babinet principle to hold. Another difference is that unlike metals at microwave frequencies (which is why the Babinet principle is frequently used in microwave antenna design) at optical frequencies metals, such as gold, can no longer be considered PEC causing results to deviate from the expected value using the Babinet principle.

The difference between the spectral properties of the LSP resonance, in terms of their spectral position and spectral profile, can be quantitatively evaluated by calculating the quality factor (Q-factor), a useful measure for evaluating the performance of sensors, defined as [226, 227]:

$$Q = \frac{\lambda_{LSP}}{FWHM_{LSP}} \tag{4.1}$$

where λ_{LSP} and $FWHM_{LSP}$ are the wavelength of the LSP and its corresponding FWHM, respectively. Therefore, the minimum in T (blue) for plasmonic nanoparticles illuminated by a plane wave polarised along the $x-$axis from Fig. 4.3b occurs at $f_0 \approx 259$ THz / $\lambda_0 \approx 1160$ nm / $E_0 \approx 1.07$ eV. The minimum in the T spectrum has a FWHM = 51.55 nm and therefore, has a Q-factor ≈ 22.5. The LSP resonant mode of the complementary nanostructure, a plane wave with E_y polarisation incident on the plasmonic nanoapertures, is excited when $f_0 \approx 250$ THz / $\lambda_0 \approx 1200$ nm / $E_0 \approx 1.03$ eV with a Q-factor = 16.4 ($FWHM_{LSP} = 73.17$ nm), indicated by the minimum in the R (red) spectrum. Here, the quantitative differences between the spectral positions and Q-factors of the excited resonant modes can be seen due to considering realistic plasmonic nanostructures for these studies, rather than the idealised infinitely thin PEC layers required to satisfy the Babinet principle.

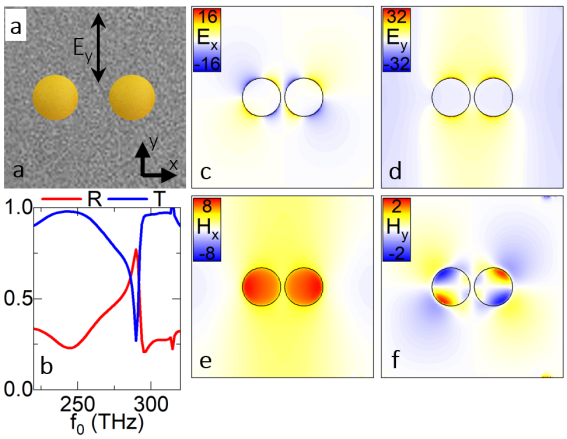

Fig. 4.5 R and T spectra and Field distributions of the plasmonic nanoparticles illuminated by an incident plane wave with E_y polarisation. (a) 2D schematic representation on the $xy-$plane with the polarisation of the incident plane wave represented by an arrow, (b) R (red solid line) and T (blue solid line) spectra, (c) E_x, (d) E_y, (e) H_x, and (f) H_y field enhancements of the LSP resonances.

Now, the spectral location has been determined for the excited LSP resonant modes in the plasmonic nanoparticles and nanoapertures, their nature and comparable properties in terms of field enhancement distribution (the ratio of the full electric or magnetic field spatial distributions and the spatial distributions of the incident excitation field with the direction of the specific vectorial component used to the enhancement dictating the sign convention determined [41], referred to hereafter as field distributions), can be discussed. The plasmonic nanostructures being studied consist of two plasmonic features, therefore, the LSP modes produced in them will be a result of the individual LSP modes excited in each plasmonic dimer being hybridised. The nature of the hybridised modes is different for the two complementary nanostructures, discussed in [228], however, due to the Babinet principle their

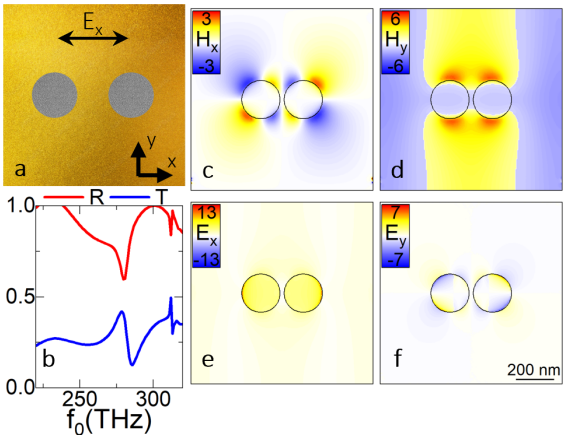

Fig. 4.6 R and T spectra and Field distributions of the plasmonic nanoapertures illuminated by an incident plane wave with E_x polarisation. (a) 2D schematic representation on the $xy-$plane showing the direction of the E_x polarised incident plane wave illuminating it, (b) R (red solid line) and T (blue solid line) spectra, (c) H_x, (d) H_y, (e) E_x, and (f) E_y field enhancements of the LSP resonances.

$\mathbf{E}-$ and $\mathbf{H}-$ field distributions will be complementary. The $\mathbf{E}-$ and $\mathbf{H}-$ field distributions calculated at the surface of the plasmonic nanoparticles illuminated by a E_x polarised plane wave and nanoapertures illuminated by a E_y polarised plane wave are shown in Fig. 4.3c-f and Fig. 4.4c-f, respectively, at the frequency of their LSP resonant mode. By qualitatively comparing the horizontal and vertical components of the $\mathbf{E}-$field, E_x (Fig. 4.3c) and E_y (Fig. 4.3d), respectively, generated in the plasmonic nanoparticles under E_x polarisation of the incident plane wave, resemble the H_x (Fig. 4.4c) and H_y (Fig. 4.4d) components of the complementary LSP resonant mode generated in the plasmonic nanoapertures under E_y polarisation of the incident plane wave. This resemblance extends to the other field distribution components of the plasmonic nanostructures as the H_x and H_y components of the plasmonic nanoparticles shown in Fig. 4.3e,f is similar to the E_x and E_y field distributions of the plasmonic nanoapertures shown in Fig. 4.4e,f. However, it should be noted the two excited LSP resonant modes shown here have different field distribution magnitudes, as expected from ref [41]. The field distributions of the plasmonic nanoparticles and nanoapertures correspond to longitudinal dipole bonding (LDB) and complementary LDB (cLDB) LSP resonant modes (the method of interpreting the type of LSP resonant mode will be explored in-depth in Section 4.2.1).

For completeness, the orthogonal polarisation of the plane wave was used to illuminate each of the plasmonic nanostructures, with the plasmonic nanoparticles under Ey polarised illumination and the plasmonic nanoapertures under E_x polarised illumination, with a schematic representation shown in Fig. 4.5a and Fig. 4.6a, respectively. The plasmonic

nanoparticles in this scenario will have a minimum of T, and therefore, a LSP resonant mode, when $f_0 \approx 290\,\text{THz}$ / $\lambda_0 \approx 1030\,\text{nm}$ / $E_0 \approx 1.20\,\text{eV}$ with a FWHM of 21.4 nm therefore, Q-factor ≈ 48.1. Meanwhile, the complementary LSP resonant mode in the plasmonic apertures is excited at $f_0 \approx 280\,\text{THz}$ / $\lambda_0 \approx 1070\,\text{nm}$ / $E_0 \approx 1.16\,\text{eV}$ with a FWHM of 70.86 nm therefore, Q-factor ≈ 15.1, when R is at its minimum. Again, these results demonstrate that the Babinet principle approximately holds for plasmonics with the complementary LSP resonant modes being excited at similar but not the same spectral positions. Finally, the qualitative comparison of the $\mathbf{E}-$ and $\mathbf{H}-$ field component distributions of the two complementary plasmonic nanostructures shown in Fig. 4.5c-f and Fig. 4.6c-f again shows good agreement between the complementary field components as expected from the Babinet principle [41, 40]. These field distributions of the plasmonic nanoparticles and nanoapertures correspond to transverse dipole antibonding (TDA) and complementary TDA (cTDA) LSP resonant modes. When comparing the LSP resonant modes from Fig. 4.3, 4.4, 4.5 and 4.6, the excited LSP resonant mods are observed at different spectral locations as different LSP modes have been excited. Also, the plasmonic nanoparticles demonstrate a higher value of Q-factor is higher compared to the plasmonic nanoapertures, which has implications when these nanostructures are exploited as dielectric sensors. In the next section, the complementary field distributions excited in the LSP resonant modes for both plasmonic nanostructures will be labelled including a comprehensive discussion regarding the distribution of charge mapping that occurs in the different hybridised LSP modes using experimental results.

4.2.1 Experimental comparison

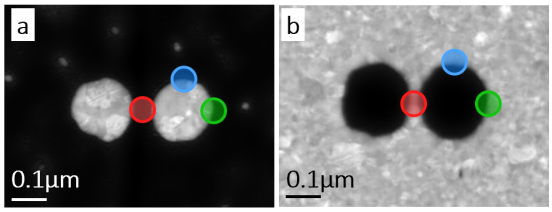

Fig. 4.7 Fabricated plasmonic (a) nanoparticles and (b) nanoapertures shown using Annular dark-field (ADF) STEM images. The coloured circles mark the location where a beam of probing electrons is transmitted to calculate EELS spectra

To corroborate the numerical results from Section 4.2, experimental work was conducted by external collaborators Dr Krapek and Dr Horak of Brno University, Czech Republic. The plasmonic nanoparticles and nanoapertures were fabricated using a standard focused ion beam lithography milling process on a 30 nm thick gold layer deposited on a Si_3N_4 membrane ($250\,\mu\text{m} \times 250\,\mu\text{m} \times 30\,\text{nm}$. The morphology and optical properties, including the LSP

modes of the plasmonic nanostructures, were characterised by analysing the nanostructures using a combination of a scanning transmission electron microscopy (STEM) and electron energy loss spectroscopy (EELS) by a transmission electron microscope in monochromated scanning regime (electron energy of 300 keV, beam current 100 pA, convergence semi-angle of 10 mrad, and collection semi-angle of 56 mrad. The FWHM of the zero-loss peak = 0.14 eV, and this value roughly represents the spectral accuracy of EELS). Annular dark-field (ADF) STEM images of the fabricated plasmonic nanoparticles and nanoapertures are shown in Fig. 4.7a,b, respectively. The dimensions of the plasmonic nanostructures determined using ADF-STEM images differ slightly from the desired dimensions ($D = 200$ nm and $L = 20$ nm). For the plasmonic particles (Fig. 4.7a), $D_{L,R} = 172$ nm for the left and right nanoparticles and $L = 50$ nm was obtained. The plasmonic nanoapertures, shown in Fig. 4.7b, $D_L = 210$ nm, $D_R = 200$ nm and $L = 20$ nm. These differences are due to nanofabrication tolerances.

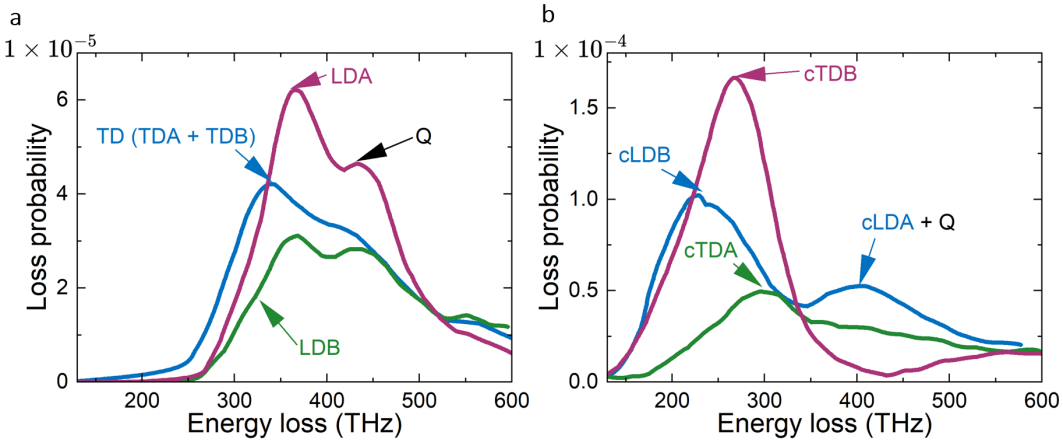

Fig. 4.8 Loss probability (per the spectral range of 0.01 eV) for the plasmonic (a) nanoparticles and (b) nanoapertures, respectively, measured at the positions of the smaller circles in Fig. 4.7.

EELS was used to characterise the LSP modes supported within the plasmonic nanostructures. This is done by transmitting a beam of probing electrons through the plasmonic nanostructures. From this, an energy spectrum is recorded from a combination of inelastically scattered electrons and contributions by electrons that have decreased in energy due to exciting an LSP mode in a plasmonic nanostructure. This excitation of LSP resonant modes in plasmonic nanostructures can be presented within the theory of classical EM. The EM field induced by the LSP mode interacts with the probing electrons [229, 230], leading to the loss probability as follows [41]:

$$\Gamma_{EELS}(\omega) = \frac{e}{\pi\hbar\omega}\int dt\mathbb{R}e\{e^{-i\omega t}\mathbf{v}\cdot\mathbf{E}_{ind}[\mathbf{r}_e(t),\omega]\} \tag{4.2}$$

where e denotes the charge of an electron, ω represents the working angular frequency, t is time, $\hbar$ is the reduced Planck constant, and $\mathbf{E}_{ind}[\mathbf{r}_e(t),\omega]$ is the induced $\mathbf{E}-$field by an electron at the electron position $\mathbf{r}_e(t)$ moving with a velocity $\mathbf{v}$. For instance, when an electron is considered to be moving along the $z-$axis, normal to the plasmonic nanostructures, the only component that will interact with the probing electrons will be the out-of-plane component of the electric field (E_z) of the plasmonic nanostructures. Therefore, EELS will be insensitive to in-plane E-fields (E_x and E_y) so any losses related to the excited LSP mode are proportional to the E_z field of the excited LSP resonance, although bulk losses related to the material and therefore will be proportional to its thickness will contribute so a subtraction of the zero-loss peak and background was performed to isolate the LSP-related losses, and the spectra were normalized.

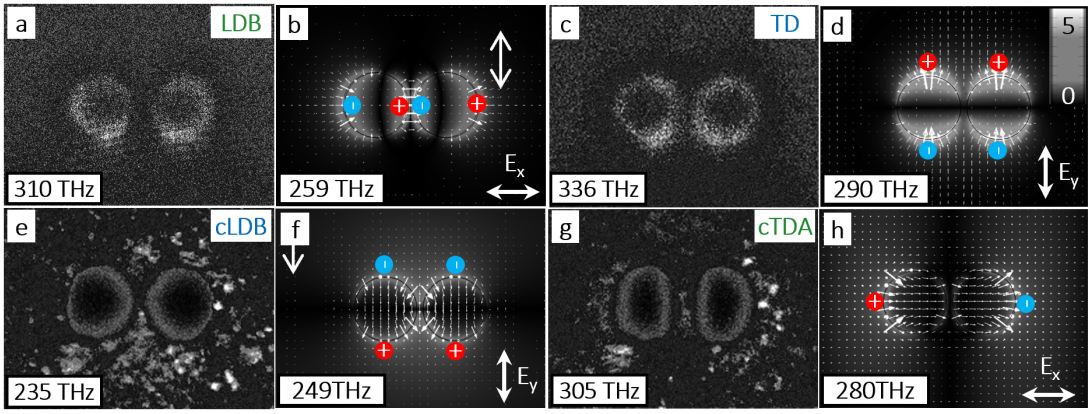

Fig. 4.9 Spatial maps of the EELS loss probability for the plasmonic nanoparticles and nanoapertures at the frequency to excite (a) LDB, (c) TD modes, (a) cLDB, and (c) cTDA modes, respectively. $|E_z|$ field distributions from numerical simulations at the plasmonic nanoparticles surface ($D_L = D_R = D = 200$nm, $L = 20$nm) when an incident plane wave with (b) E_x polarisation is incident at a frequency of the LDB mode and (d) E_y polarisation at a frequency of TDA mode, respectively, and nanoapertures ($D_L = D_R = D = 200$nm, $L = 20$nm) when they are illuminated by an incident plane wave with (b) E_y polarisation at a frequency of the cLDB mode and (d) E_x polarisation at a frequency of cTDA mode, respectively. Each numerical study includes the corresponding electric field lines. The "(+)" (red) and "(-)" (blue) symbols shown in these panels denote the location of positive and negative surface charge distributions, respectively.

Experimental EEL spectra for the plasmonic nanoparticles and nanoapertures, shown in Fig. 4.8a,b, respectively, were taken with the probe beam of electrons at three positions on the top nanostructure, the top, side and bottom, demonstrated in Fig. 4.7 as the green, blue and red

circles. As can be seen in these spectra, there are peaks and shoulders in the loss probability where LSPs have been excited in the plasmonic nanostructures. To identify the LSP resonant modes excited in the plasmonic nanostructures a combination of the procedure described in [228] and electric–magnetic Babinet complementarity to interpret the modes in the plasmonic nanoapertures. Each of the hybridised dipole modes excited in the plasmonic nanoparticles [LDB, TDA, transverse dipole bonding (TDB), and longitudinal dipole antibonding (LDA)] and complementary modes (due to the Babinet principle) in plasmonic nanoapertures [cLDB, cTDB, cTDA, and cLDA] have their spectral location indicated by arrows in Fig. 4.8a,b. The arrow labelled TD is a result of the TDB and TDA supported in the plasmonic nanoparticles being unresolved. There are also higher-order plasmonic modes, such as contributions from the quadruple mode (disregarding its hybridisation) labelled as Q. Still, these fare beyond the scope of this study.

Compared to the numerical R and T spectra, there are more LSP modes observed in the experimental loss probability spectra. This is a result of the numerical studies using plane waves, as they can only couple with LSP plasmonic modes with non-zero dipole electric moments known as bright modes. The other LSP dipole modes are known as *dark* modes and do not manifest in the R and T spectra, but can be observed using EELS [217, 231, 201, 232]. These dark LSP modes are not considered in this study as the bright plasmonic dipole modes will be exploited for dielectric sensing. Fig. 4.9a,c and Fig. 4.9e,g show experimental loss probability spatial maps (integrated over a spectral range of 0.1 eV centred on the mode energy to reduce the noise) at the energy of the LDB and TDA LSP modes in the plasmonic nanoparticles and cLDB and cTDA LSP modes in the plasmonic nanoapertures. The spectral position of the plasmonic resonant modes is shown in Table 4.1.

The spectral position of the LSP resonant modes extracted from the EELS spectra again approximately follow the Babinet principle, as expected, and they agree with the spectral positions obtained from the numerical simulations. There are some small differences between the experimental and numerical spectral locations of the LSP resonant modes which can be attributed to differences in the plasmonic nanostructures, introduced in the fabrication process due to nanofabrication tolerances[193]. For example, the plasmonic nanostructures are not perfectly cylindrical or there could be variations in the thickness of the Si_3N_4 substrate. The effect of potential imperfections may have on the resonance of the nanostructures is studied in Section 4.4. From Table 4.1, the spectral position of the LSP resonant modes in the plasmonic nanoparticles obtained from the EELS characterisation is at noticeably higher frequencies/energies (lower wavelengths) compared to the numerical studies. This is likely a result of the diameters of the fabricated cylinders being approximately 14% smaller than intended. There are also differences for the plasmonic nanoaperture cases as well, however,

the diameter was only around 2.5% larger than intended so the variations are less significant. Corrected values of the spectral position can be obtained by exploiting the approximately linear dispersion relation between the reciprocal diameter of a cylindrical antenna and the LSP resonant mode energy, which are shown in Table 4.1. These values are generally closer to the ones calculated in the numerical simulations. Further, deviations may also occur as the two methods, R and T spectra and EELS, are far- and near-field-based calculations, respectively [233].

To compare the LSP resonant modes from the numerical studies to the experimental EELS loss probability maps for the plasmonic nanoparticles and nanoapertures, shown in Fig. 4.9a,c,e,g, the calculated out-of-plane electric field ($|E_z|$) distributions (due to Eq. (4.2)) are shown in Fig. 4.9b,d,f,h, respectively, with corresponding electric field lines. When comparing the EELS maps and the $|E_z|$ field distractions of the plasmonic nanoparticles in Fig. 4.9, there is a qualitative agreement between the two, although the visual comparison is quite challenging. This is a result of a smaller energy difference between all of the hybridised dipole modes causing a strong spectral overlap. This is caused by the fabricated particles, shown in Fig. 4.7a, having a separation between the plasmonic nanoparticles $L \approx 50\,\text{nm}$ rather than the intended 20 nm, used in the numerical simulations. Red "+" symbols and blue "-" symbols schematically show the accumulation of charge carriers of the LSP resonant modes in the plasmonic nanoparticles. These charge distributions are indicators of the type of LSP resonant mode, enabling the differentiation of longitudinal and transverse bonding and anti-bonding modes [228, 41]. In the plasmonic nanoparticles illuminated by an E_y or E_x polarised plane wave, shown in Fig. 4.9b,d, respectively, Have accumulations of charge aligned along the $x-$axis and $y-$axis, respectively, in the direction of the respective plane wave polarisation and therefore, they are LD and TD, with them being determined as bonding and anti-bonding by how the charge accumulations are positioned and therefore, how the electric field lines flow. The comparison of the EELS maps and the numerical results of the plasmonic nanoapertures are then shown in Fig. 4.9e,f and Fig. 4.9g,h. Here the field distributions of the two qualitatively agree with each other as expected. Again, the charge accumulations are shown. As these are complementary nanostructures to the plasmonic nanoparticles shown in Fig. 4.9, the $|Ez|$ and therefore, the charge accumulations are also complimentary. Therefore, now the charge accumulations are aligned orthogonally to the polarisation of the illuminating plane wave representing the cLDB and cTDA LSP resonant modes.

Table 4.1 The spectral location of excited bright LSP resonant dipole modes in experimental and numerically calculated plasmonic nanoparticles and plasmonic nanometres

LSP resonant modes						
LSP mode	EELS			Numerical		
	Direct (corrected)					
	f_0 (THz)	E_0 (eV)	λ_0 (μm)	f_0 (THz)	E_0 (eV)	λ_0 (μm)
Particles						
LDB	310 (267)	0.967 (1.10)	1.28 (1.12)	259	1.07	1.16
TDA	336 (289)	1.39 (1.20)	0.892 (1.04)	290	1.20	1.03
Aperture						
cLDB	235 (241)	0.972 (1.00)	1.28 (1.24)	250	1.03	1.12
cTDA	305 (312)	1.26 (1.29)	0.983 (0.961)	280	1.16	1.07

4.3 Dielectric Sensing

In this section, the LSP resonant modes excited in complementary plasmonic nanoparticles and nanoapertures explored previously are exploited to sense variations of a dielectric analyte near the plasmonic nanostructures. This can be done as these changes will cause the spectral position of the LSP resonant mode in the R and T spectra of the nanostructure to shift which can be observed and measured. Different configurations of the analyte will be considered as the size, shape and refractive index (n_a) of the dielectric changes with the shift for each variation calculated. To evaluate the sensing performance of the plasmonic nanostructures, the sensitivity will be calculated for each case. The sensitivity is defined as the ratio between the variation in the wavelength of the LSP resonant mode (λ_{LSP}) and the change in the n_a:

$$S = \frac{\Delta\lambda_{LSP}}{\Delta n_a}, [\frac{\text{nm}}{RIU}] \tag{4.3}$$

where RIU is the refractive index unit [234].

4.3.1 Thin Film

The first study considered was with the analyte as a thin dielectric film positioned on top of the plasmonic nanostructures. The schematic representation of this sensing configuration for the plasmonic nanoparticles and nanoapertures is shown in Fig. 4.2a,c, respectively. To make the spectral position of the LSP resonant mode shift, the n_a is varied between 1.5 and 3 in steps of 0.25 as the thickness (δ_a) of the thin film dielectric analyte (δ_a) changes. Using the R and T spectra for the plasmonic nanoparticles and nanoapertures the spectral location

of the LSP resonant modes as the properties of the thin film analyte changes are mapped in Fig. 4.10a,b, respectively. This spectral shift is shown for both E_x (solid) and E_y polarisation of the plane wave as the δ_a has values of 50 nm (blue), 100 nm (green), 150 nm (purple) and 200 nm (pink). As observed, a greater shift of the spectral location of the LSP resonant mode in the plasmonic nanoparticles, shown in Fig. 4.10a, occurs when the plane wave has E_x polarisation (solid) compared to the orthogonal E_y polarisation (dashed). Meanwhile the opposite is true for the plasmonic nanoapertures, shown in Fig. 4.10b, with the larger shift being observed when using E_y polarisation of the plane wave. These increased shifts of the spectral location of the LSP resonant mode are a result of the increased interaction of the excited field distribution with the analyte, as these LSP resonant modes correspond to a high field concentration near the plasmonic nanostructures.

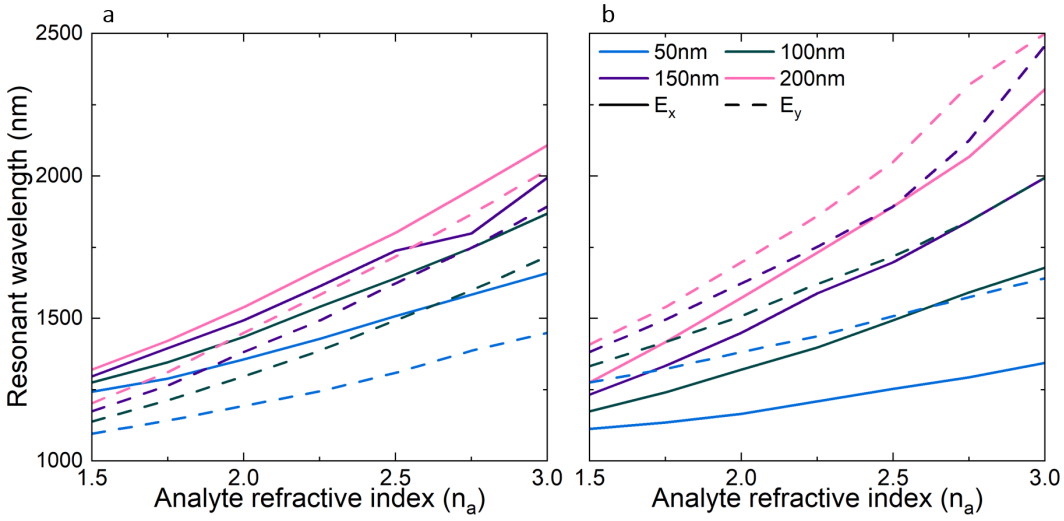

Fig. 4.10 Resonant wavelengths of the LSP resonant modes generated in the (a) plasmonic nanoparticles, and (b) the plasmonic nanoapertures a range of 1.5 to 3 in steps of 0.25 is used for n_a, when a plane wave with E_x (solid line) and E_y (dashed line) polarisation is incident upon them. Thicknesses of the analyte are chosen to be: $\delta_a = 50$ nm (blue), 100 nm (green), 150 nm (purple) and 200 nm (pink)

Using these shifts in the spectral location of the LSP resonant modes in the plasmonic nanoparticles and nanoapertures the sensitivity can be calculated, as shown in Fig. 4.11a,b, respectively. As expected from Fig. 4.10, the sensitivity of the two plasmonic nanostructures increases as both n_a and δ_a increase, regardless of the polarisation of the plane wave. As observed, when the thin dielectric film is $\delta = 50$ nm with $n_a = 1.5$ the sensitivity of both the plasmonic nanoparticles and nanoapertures can be as low as $S \approx 100\,\text{nm}RIU^{-1}$ with maximum values of $S \approx 450\,\text{nm}RIU^{-1}$ and $S \approx 650\,\text{nm}RIU^{-1}$, respectively, when the thin dielectric analyte film has properties of $\delta = 200$ nm with $n_a = 3.0$. As with the spectral

location of the LSP resonant mode, the sensitivity of the plasmonic nanostructures also depends on the polarisation of the plane wave used to illuminate them. When the plasmonic nanoparticles are illuminated by a plane wave with E_x polarisation (solid) they generally show a higher sensitivity than when they are illuminated by an incident plane wave with E_y polarisation (dashed). The plasmonic nanoapertures again show the opposite behaviour with higher sensitivities demonstrated with E_y polarised plane waves.

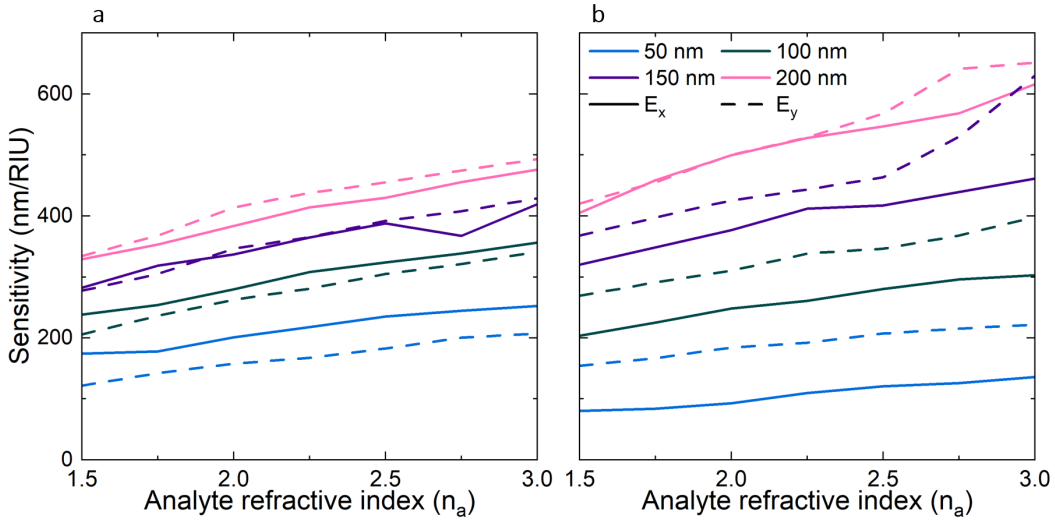

Fig. 4.11 Sensitivity of the (c) plasmonic nanoparticles and (f) nanoapertures when illuminated by an E_x (solid) and E_y (dashed) polarised incident plane wave. The analyte thicknesses are chosen as $\delta_a = 50\,\text{nm}$ (blue), 100 nm (green), 150 nm (purple) and 200 nm (pink)

This increase of the sensitivity again can be attributed to the excitation of a LSP resonant mode in the plasmonic nanoparticles and nanoaperture with a high field concentration in the field distribution. For the plasmonic nanoparticles, this will be a $\mathbf{E}-$field hotspot in between the two dimers when the polarisation of the plane wave is E_x, whereas there will be a complimentary $\mathbf{H}-$field hotspot on the metal bridge between the plasmonic nanoapertures when the polarisation of the plane wave is E_y due to the Babinet principle. These field hotspots cause the LSP resonant mode to interact more with the analyte, causing a higher sensitivity. When comparing the plasmonic nanoparticles and nanoapertures with a field hotspot, the plasmonic nanoapertures have a higher sensitivity when the dielectric analyte is a thin film positioned on top of the nanostructures. This is a result of the field hotspot being excited on the metal bridge where the dielectric analyte film is positioned rather than between the nanoparticles, causing an enhanced interaction and therefore, greater sensitivity. Finally, when the dielectrics are thicker ($\delta_a > 100\,\text{nm}$) the sensitivity values calculated for either polarisation of the plane wave incident on the plasmonic nanostructures are similar. This change to be independent of polarisation is likely caused by multiple reflections within

the dielectric rather than the LSP resonant mode interacting with the dielectric. The values of sensitivity calculated for the plasmonic nanostructures are in line with values found in the literature for similar nanostructures [235, 236].

4.3.2 Analyte within plasmonic structures

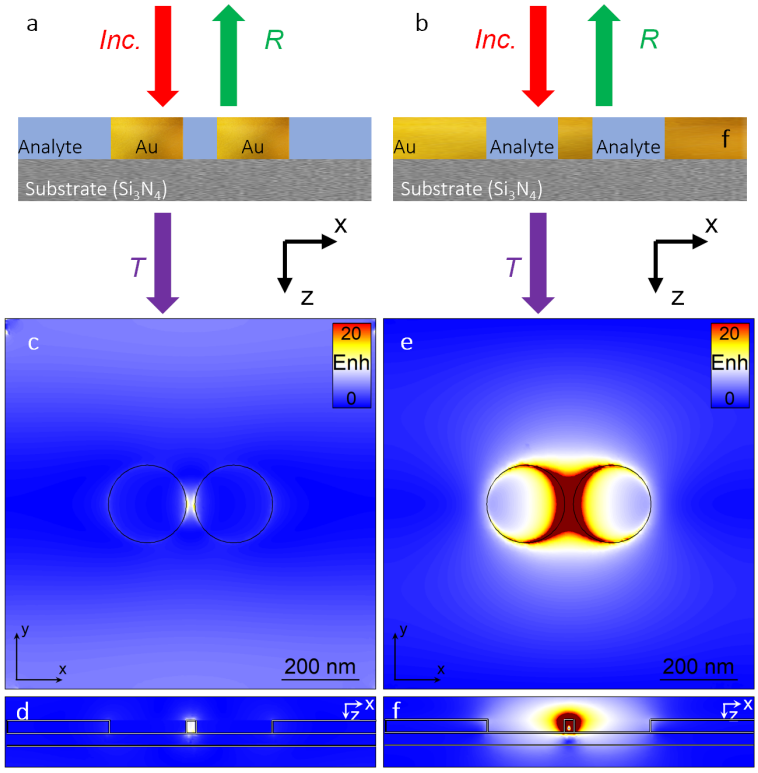

Fig. 4.12 2D cross-section of a dielectric analyte (a) surrounding plasmonic nanoparticles and (b) filling nanoapertures. Power enhancement on the (b,e) $xy-$plane and (d,f) $yz-$plane for the plasmonic nanoparticles and nanoapertures shown in (a,b), respectively, considering an analyte ($n_a = 1.5$). A plane wave with E_x or E_y polarisation, respectively, is incident on the plasmonic nanostructures. Note that the power enhancement in (e,f) uses the same scale as (c,d) to saturate their power enhancement so the difference can be more easily observed.

The dielectric analyte in the previous section would likely be challenging to find or fabricate an analyte that is flat on both sides [237]. Therefore, an alternate configuration for the dielectric analyte is considered here, with the sensing performance of the plasmonic nanostructures evaluated with the dielectric analyte used within the complementary plasmonic nanoparticles and nanoapertures. A 2D schematic representation showing a cross-section of the plasmonic nanoparticles immersed within the dielectric analyte, not air as in the previous studies, is shown in Fig. 4.12a, where the nanoparticles and dieletric analyte have the same

thickness (30 nm) in the direction of propagation ($z-$axis). A schematic representation of the complementary plasmonic nanoapertures filled with the dielectric analyte is shown in Fig. 4.12d.

Using the plasmonic nanoparticles illuminated by an E_x polarised plane wave immersed with a dielectric analyte ($n_a = 1.5$), numerical results showing the power enhancement on the $xy-$ and $zy-$planes are shown in Fig. 4.12b,c, respectively, at $f_0 =$ 239 THz / $\lambda_0 \approx 1250$ nm / $E0 \approx 0.99$ eV. Between the two plasmonic nanoparticles, a field hotspot is observed, with a power enhancement of around 20 in the gap. Meanwhile, the power enhancement in the complementary plasmonic nanoaperture illuminated by a E_y polarised plane wave filled with dielectric analyte is shown on the $xy-$ and $zy-$planes in Fig. 4.12e,f, respectively, at $f_0 =$ 241 THz / $\lambda_0 \approx 1240$ nm / $E0 \approx 1.00$ eV. In this configuration, the field hotspot is tightly bound to the gold bridge between the plasmonic nanoapertures with a power enhancement of 60. Although the magnitude of the power enhancement differs between these two complementary plasmonic nanostructures, the power enhancement distributions between them are qualitatively similar, as expected due to the Babinet principle.

The sensing performance of the plasmonic nanoparticles and nanoapertures immersed in or filled with the dielectric analyte, respectively, as the refractive index (n_a) varies is evaluated. The T spectrum of the plasmonic nanoparticles and the R spectrum of the plasmonic nanoapertures are shown in Fig. 4.13a,b, for both E_x (red) and E_y (blue) polarisation of the incident plane wave. The minima of the respective spectra indicate the spectral location of the LSP resonant mode, where dashed lines have been added to guide the eye. As expected from Fig. 4.10, the spectral location of the LSP resonant modes red shift as n_a increases.

These shifts in the spectral location of the LSP resonant modes are used to calculate the sensitivity, shown in Fig. 4.14a,b, of the plasmonic nanoparticles (red) and nanoapertures (blue), respectively, for both orthogonal plane wave polarisations: E_x (solid) and E_y (dashed). As the n_a of the dielectric increases the sensitivity of the plasmonic nanostructures increases as expected with the plasmonic nanoparticles when illuminated by an E_x or an E_y polarised plane wave have values of sensitivity of 196 to 253 nm/RIU and 90 to 150 nm/RIU, respectively, while the complementary plasmonic nanoapertures have sensitivities of 91 to 133 nm/RIU and 15 nm/RIU to 50 nm/RIU, respectively. However, as observed, the values of the sensitivities for all of the nanostructures are significantly decreased. This is a result of the volume of the dielectric used in the nanostructures being significantly reduced with only a thickness of 30 nm which is why the sensitivities are in the same order of magnitude as the case shown in Fig. 4.11 with a $\delta_a = 50$ nm. A comprehensive study taking into account the volume of the dielectric analyte is considered in Section 4.3.4. When using this configuration of the dielectric, the plasmonic nanoparticles are shown to have higher sensitivities when they are

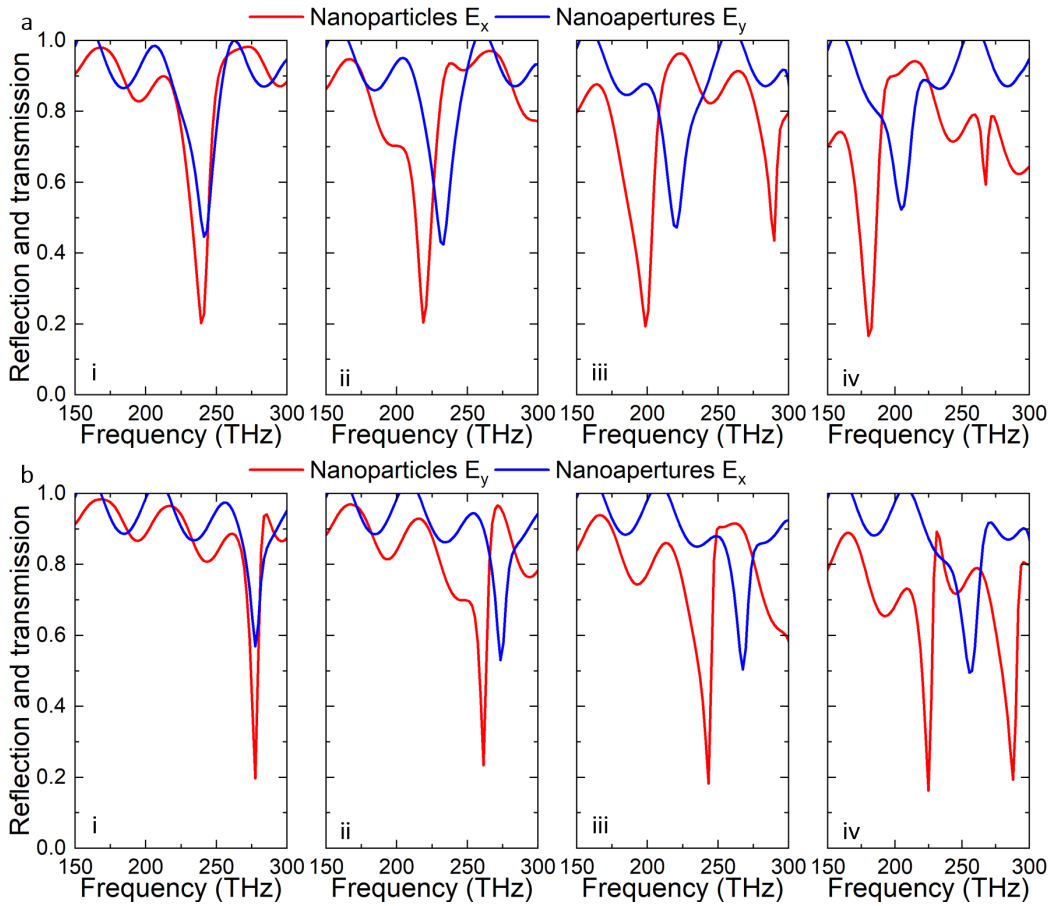

Fig. 4.13 T/R spectra produced by plasmonic nanoparticles (red) / nanoapertures (blue) when they are illuminated by an (a) E_x/E_y and (b) E_y/E_x polarised plane wave as the dielectric within the structures varies with values of $n_a =$ (i) 1.5, (ii) 2, (iii) 2.5, and (iv) 3.

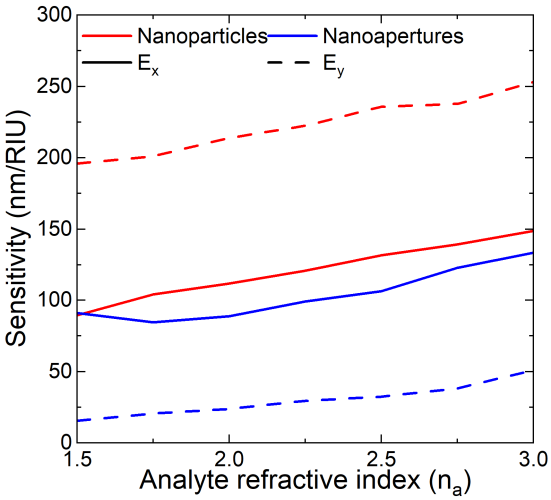

Fig. 4.14 Sensitivity of the plasmonic nanoparticles (red) and nanoapertures (blue) illuminated by an incident plane wave with l E_x (red) and E_y (black) polarisations as the dielectric has values of n_a that range from 1.5 to 3 in steps of 0.25.

immersed in the dielectric compared to when the thin dielectric analyte film is positioned on top with $\delta_a = 50$ nm whereas the opposite is true for the plasmonic nanoapertures. This is due to the majority of the excited hotspot for each of these higher sensitivity cases being contained in the dielectric analyte increasing the amount of interaction. This shows the complementary nature of the plasmonic nanostructures being beneficial for different applications.

4.3.3 Small Dielectric particle

The next study considers a case using a small dielectric particle positioned on top of the plasmonic nanostructures. A schematic representation of this configuration is shown for the plasmonic nanoparticles on the $yz-$ and $xy-$planes is shown in Fig. 4.15a,b, respectively, and the schematic representation on the same planes are shown in Fig. 4.15c,d. Here a particle of dielectric analyte of dimensions 200 nm along the $x-$axis, 100 nm along the $y-$axis and a thickness of 50 nm along the $z-$axis is positioned on top of the plasmonic nanostructures between the dimers.

The sensitivity of the plasmonic nanoparticles (red) and nanoapertures (blue) illuminated by a E_x (solid) and E_y (dashed) polarised plane wave is calculated and shown in Fig. 4.16. As observed when the LSP resonant mode of the plasmonic nanostructures do not have an associated field hotspot, such as when the plasmonic nanoparticles and nano apertures are illuminated by E_y and E_x polarised plane waves respectively, there is very little interaction with the dielectric analyte in this configuration so it does not affect the spectral location of the LSP resonant mode, demonstrated by low sensitivity values. However, in the opposite

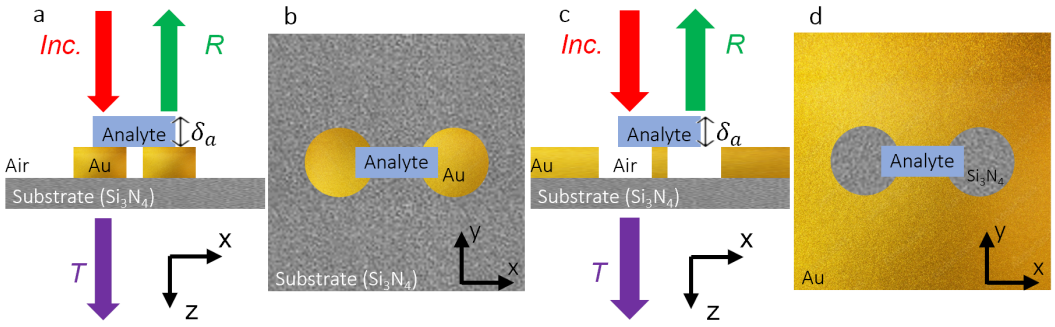

Fig. 4.15 2D Schematic representation of the cross-section on the (a,c) $yz-$ and (b,d) $xy-$plane for plasmonic nanoparticles and nanoapertures, respectively, used to determine changes of a nearby block of analyte with a thickness of δ_a 50 nm.

case, plasmonic nanoparticles and nano apertures illuminated by E_y and E_x polarised plane waves, respectively, there is an increased sensitivity. However, the value of this sensitivity is still small compared to the values shown in previous analyte configurations, due to the relatively small amount of analyte. However, in the next section, this will be explored in terms of the sensitivity per unit volume.

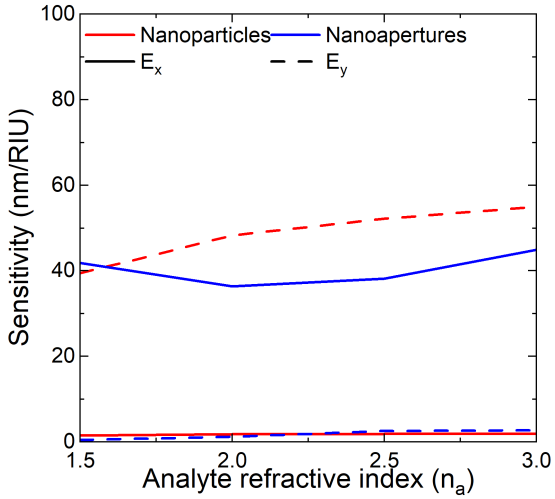

Fig. 4.16 Sensitivity of plasmonic nanoparticles (red) and plasmonic nanoapertures (blue) as δ_a has values of 1.5 to 3 in steps of 0.5 when considering E_x (solid line) and E_y (dashed line) polarisation of the incident plane wave

4.3.4 Volume Sensing

In this section, the different dielectric analyte configurations, thin film, immersed and particle, will be considered in terms of their relative volume. In the configuration from Section 4.3.1,

when the dielectric is a thin film positioned atop the whole plasmonic structure the thin analyte film will have a volume (defined as $V = h_x \times h_y \times \delta_a$) dictated by the thickness of the analyte, $\delta_a = 50$ nm, 100 nm, 150 nm, and 200 nm. The volumes for each thickness are shown in Table 4.2. These V can then be used to normalise the values of sensitivity shown in Fig. 4.11:

$$S_V = \frac{S}{V}, \left[\frac{nm}{RIU\,nm^3}\right] \tag{4.4}$$

These values of normalised sensitivity of the plasmonic nanoparticles and nanoapertures are shown in Fig. 4.17a,b, respectively when illuminated by an E_x (solid) and E_y (dashed) polarised plane wave. The S_V can be observed to decrease as δ_a and V increase, as expected, as when comparing the sensitivity of the δ_a =50 nm and the δ_a =200 nm cases in Fig. 4.2, the sensitivity is around $\times 2$ greater for the thicker film but the $V \times 4$ larger. As in Section 4.3.1, the cases with a field hotspot generally have higher values of sensitivity, when the plasmonic nanoparticles and nanoapertures are illuminated by an E_x or E_y polarised plane wave, respectively, compared to the LSP resonant modes without a field hotspot.

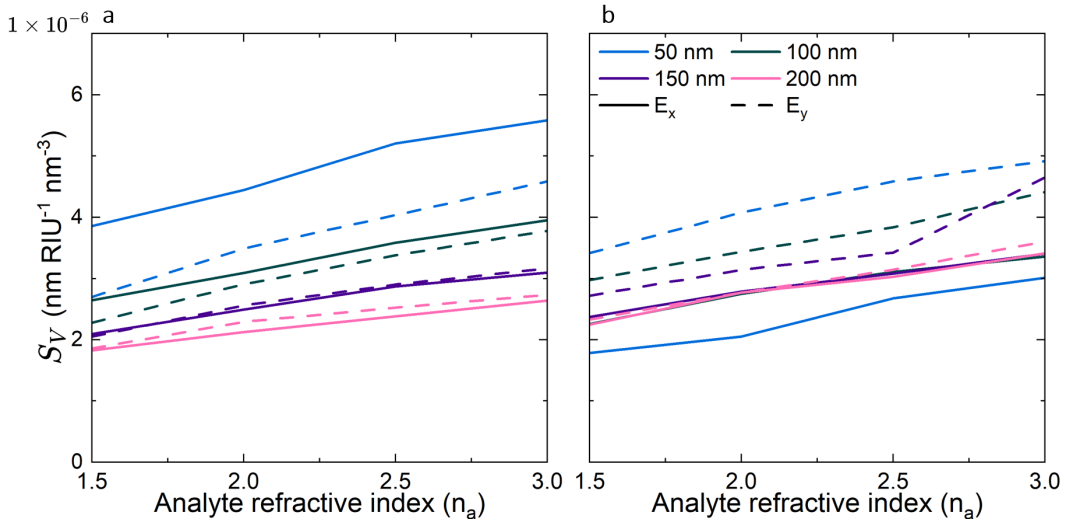

Fig. 4.17 Volume sensitivity of the (a) plasmonic particles and (b) apertures for analyte thicknesses of δ_a = 50 nm (blue), δ_a = 100 nm (green), δ_a = 150 nm (purple) and δ_a = 200 nm (pink). The dashed and solid lines correspond to the results using E_x or E_y polarisation of the incident plane wave.

The next case considered was when the plasmonic nanoparticles and nanoapertures were immersed or filled with the dielectric analyte, shown in Section 4.3.2. To calculate the volume of the analyte the volume of the plasmonic nanoparticles is required. From this the volume of the dielectric analyte that immerses the plasmonic nanoparticles will

Table 4.2 Analyte volume for each analyte film thickness

δ_a (nm)	V (1×10^8 nm^3)
50	4.5125
100	9.025
150	1.35375
200	18.05

be $V_p = (h_x \times h_y \times \delta_a) - 2 \times (\pi r^2 \delta_a)$ and the volume of the dielectric analyte filling the plasmonic nanoapertures will be $V_{ap} = 2 \times (\pi r^2 \delta_a)$. Therefore, when using $\delta_a = 30$ nm and $r = 100$ nm, the analyte volume in these configurations will be $V_p = 2.519 \times 10^7$ nm^3 and $V_{ap} = 1.885 \times 10^6$ nm^3. Then by using the sensitivities from Fig. 4.14, the volume normalised sensitivity for this analyte configuration is shown in Fig. 4.18 for the plasmonic nanoparticles (red) and nanoapertures (blue) when illuminated by an E_x (solid) and E_y (dashed) polarised plane wave. As observed, the S_V is improved compared to the thin film values shown in Fig. 4.17. This is explained by a combination of increased interaction of the field distribution of the LSP resonant mode with reduced analyte volume, with a significantly large increase for the nanoaperture configuration due to the volume being around two orders of magnitude less than the volume of the thin film. Again, when a field hotspot is excited the plasmonic nanostructures have higher S_V.

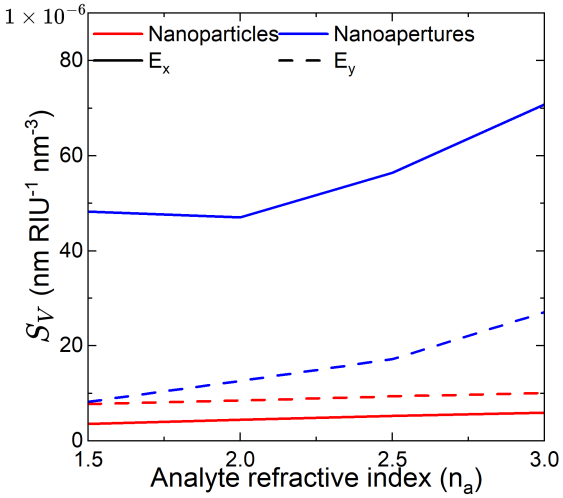

Fig. 4.18 Volume sensitivity of the plasmonic nanoparticles surrounded by (red) and nanoapertures filled with (blue) when the analyte. The structures are illuminated by a plane wave polarised in the E_x (solid) and E_y (dashed) direction.

The final dielectric analyte configuration is as a particle shown in Section 4.3.3. As the dielectric analyte particle has dimensions 200 nm × 100 nm × 50 nm the volume will be $V = 1 \times 10^6$ nm^3. The volume normalised sensitivity of the analyte particle is then calculated using Fig. 4.16 and is shown in Fig. 4.19. Comparing these values of S_V to those shown in Fig. 4.17 and Fig. 4.19, the values have a comparable magnitude for the cases when a hotspot is excited.

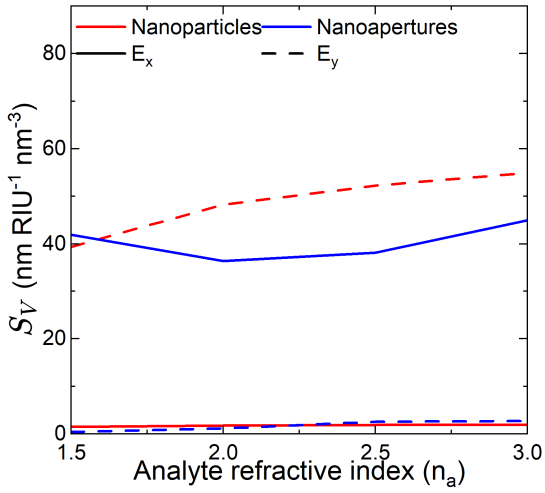

Fig. 4.19 Volume sensitivity of plasmonic nanoparticles (red) and plasmonic nanoapertures (blue) when δ_a is changed from 1.5 to 3 in steps of 0.5 considering an incident plane wave with E_x (solid line) and E_y (dashed line) polarisation.

4.4 Considerations of tolerances

As has been shown previously, small deviations between the dimensions of the experimentally fabricated plasmonic nanostructures and the plasmonic nanostructures used in the numerical simulations have the potential to affect the response of the LSP spectral location. These will be a result of the tolerance of current nanofabrication methods and techniques as even nanometer differences will be reflected in the calculated R and T spectra, and therefore the spectral location of the LSP resonant modes. To explore this, a study is conducted to observe the effect of small changes in the thickness of the Si_3N_4 used as the substrate for the nanostructures in the previous section. When the substrate thickness is changed from 30 nm to 20 nm, the change of spectral location of the LSP resonant modes of the numerical plasmonic nanostructures are shown in Table 4.3 and compare to the spectral location when using experimental EELS. Here, a decrease in the thickness of the substrate causes an observable shift to lower frequencies. Therefore, for the cases considered here,

fabrication tolerances at nanometre scales of the desired dimensions of the nanostructures will cause variations in the spectral location of the fabricated plasmonic nanoparticles and nanoapertures however qualitative comparisons are still possible.

Table 4.3 Spectral location of LSP resonant modes of plasmonic nanostructures on a substrate with varying thickness

LSP resonant modes			
LSP mode/ plane wave polarisation	EELS	Numerical substrate thickness	
		20 nm	30 nm
	f_0 (THz)	f_0 (THz)	f_0 (THz)
Particles			
LDB	310	259	269
TDA	336	290	299
Aperture			
cLDB	235	249	259
cTDA	305	280	285

Chapter 5

Conclusions and future work

This final chapter of the thesis provides a summary of the conclusions obtained in each of the previous chapters. Moreover, even though there have been several studies for each of the structures shown in this thesis, there are still further potential investigations that can be conducted to further improve and expand them, including exploiting them in more potential applications. Therefore, a comprehensive list of potential tasks to further explore and evaluate is presented.

5.1 Conclusions

5.1.1 Chapter 2: From photonic nanojets to photonic hooks to bend light

- Truncated spheres attached to an optical fibre can produce a high-intensity, narrow beam outside of the particle even when the ratio between the particle and the surrounding media is greater than two.
- Illuminating two dielectric cuboid particles of the same refractive index and geometry with a plane wave will result in a focus being produced with the separation between the particles controlling the position of the focus, with large separation increasing the distance of the focus from the output surface of the particles.
- By introducing asymmetry to these two dielectric particles in terms of their geometry and refractive index the resulting interference can cause the focus to have curvature becoming a photonic hook.

- The properties of the photonic hooks can be controlled by changing and controlling the geometry and refractive index of the dielectric particles with the best photonic hooks being produced by using one particle with low diffraction and the other with high scattering of the incident electric field of the plane wave.
- The control of the electromagnetic and geometric properties of the particles gives different options for the dielectric particles each producing photonic hooks.
- When designing the geometry and electromagnetic properties of the particles the case choosing one particle to have the minimum possible diffraction and then the highest scattering with the same chosen geometry/refractive index generally performs best.
- When the length of the geometry is different, the best photonic hooks are produced when the output surfaces of the particles are aligned, although, for larger separations between the particles, the effect of the alignment is reduced.
- Increasing the separation between the particles causes the photonic hook to be generated further away from the output surface of the dielectric particles becoming elongated in the direction of propagation with lower transversal spatial resolutions and less curvature of the photonic hook.
- Photonic hooks should be able to be realised experimentally even when used with a non-transparent substrate although distortions occur, which increase when the substrate has a higher refractive index.

5.1.2 Chapter 3: Exploiting surfaces plasmons polaritons and classical electromagnetism for focusing structures.

- The effective properties of the different regions in a plasmonic structure where surface plasmon polaritons propagate can be solved analytically using effective medium techniques.
- The *lens maker equation* can be adapted to plasmonics by implementing effective media into the equation.
- The adapted *lens maker equation* can be exploited to design different lens profiles for surface plasmon polaritons including convex-planar and positive-meniscus lenses to produce a focus.

- Comparisons of these two geometries when used with surface plasmon polaritons show the meniscus profile can produce a diffraction-limited focus with higher power enhancement and smaller depth of focus.
- The performance of the plasmonic meniscus lens can be predicted using the adapted *lens maker equation* when used in a broadband setting.
- The plasmonic lenses are shown to produce focus even rotated by 30° with performance only decreasing significantly after a rotation of 15°.
- The robustness of the plasmonic lenses has been demonstrated with several potential fabrication errors including vanishing edges and height changes of the dielectric still generating a focus with a position which can be predicted by the adapted *lens maker equation*.

5.1.3 Chapter 4: From classical concepts into plasmonics: Localised surface plasmons

- Metallic nanostructures consisting of dimers can be designed for use in plasmonics using the classical concept of the Babinet principle.
- Comparisons of the spectral location and the electric and magnetic fields of complementary plasmonic show good agreement between one another although small discrepancies occur in the spectral locations due to deviation from the Babinet principle in terms of structure thickness and wave penetration in the materials.
- Comparisons of numerical and experimental results show the spectral location and field distributions agree validating the Babinet principle in plasmonics.
- The spectral location of LSP modes is sensitive to changes in the surrounding area near the structures.
- When a thin film is positioned on the plasmonic structures the calculated position of the LSP mode can be used to determine dynamic changes of the thin film in terms of refractive index and thickness.
- The complementary plasmonic structures can be used to sense changes in the refractive index of a dielectric used as part of the plasmonic structures themselves.
- Changes in the refractive index of a small dielectric particle can be observed in the spectral location of the excited LSP mode.

- The plasmonic apertures perform better when the dielectric analyte is on the surface of the metal while the plasmonic particles show enhanced performance when the dielectric is between the dimers.
- To normalise the sensitives of the plasmonic structures for the different geometries of the dielectric analyte the volume sensitivity for each configuration was calculated which demonstrated that the sensors are effective for small volumes when near the excited LSP hotspot
- The sensitivity of the structures discussed is comparable to other similar sensing structures in literature.
- Deviations in the fabrication process can cause small deviations in the spectral location on the LSP modes but are robust enough to overcome this.

5.2 Further work

- To experimental demonstration of photonic hooks using dielectric particles.
- To expand photonic hooks into different frequency ranges including the optical and NIR regimes.
- To produce photonic hooks using these dual-dielectric structures in plasmonics.
- To exploit photonic hooks for optical trapping/forces.
- To exploit plasmonic lenses designed using the adapted *lens maker equation* to produce optical forces for use as optical tweezers.
- To use plasmonic lenses designed using the adapted *lens maker equation* to sense small particles using back-scattering enhancement.
- To increase the effective refractive index of the meniscus lens region to increase the curvature of the output surface of the lens.
- To utilise gradient index techniques to make the plasmonic meniscus lens more compact.
- To further investigate the validity and limitation of the Babinet principle in plasmonics due to the finite thickness and finite conductivity.

- To study the effect of the substrate and fabrication imperfections on the Babinet principle in plasmonics.
- To expand the use of complementary plasmonic structures in microfluidics.
- To improve the sensing capabilities of the complementary plasmonic structures by combining them.
- To further expand the library of materials produced and characterised to include polymers such as ABS, PLA blends and PVA, to name a few.
- To characterise the polymers in a wider broadband spectrum to include an increased number of useful wavelengths such as 1310 nm.
- To use the characterised materials in more applications such as Bragg mirrors and lenses
- To fabricate the potential applications using FDM techniques.

References

[1] P. B. Johnson and R. W. Christy, "Optical Constant of the Nobel Metals," *Physica L Re View B*, vol. 6, no. 12, pp. 4370–4379, 1972.

[2] D. M. Pozar, "Electromagnetic Theory," in *Microwave Engineering*, ch. 1, pp. 1–47, IEEE, 4 ed., 2012.

[3] C. Sandorfy, R. Buchet, and G. Lachenal, "Principles of Molecular Vibrations for Near-Infrared Spectroscopy," in *Near-Infrared Spectroscopy in Food Science and Technology*, pp. 11–46, Wiley, 10 2006.

[4] M. Guarnieri, "Two Millennia of Light: The Long Path to Maxwell's Waves," *IEEE Industrial Electronics Magazine*, vol. 9, no. 2, pp. 54–60, 2015.

[5] I. Newton and G. Hemming, *Opticks: or, A treatise of the reflections, refractions, inflexions and colours of light : also two treatises of the species and magnitude of curvilinear figures*. London: Printed for Sam. Smith, and Benj. Walford, 7 1704.

[6] N. Lane, "The unseen World: Reflections on Leeuwenhoek (1677) 'Concerning little animals'," *Philosophical Transactions of the Royal Society B: Biological Sciences*, vol. 370, no. 1666, 2015.

[7] T. Ohlsson, "Maxwell's equations and quantization of the electromagnetic field," in *Relativistic Quantum Physics*, vol. 1, pp. 155–175, Cambridge University Press, 9 2011.

[8] A. L. Dávalos and D. Zanette, "Linear Material Media," in *Fundamentals of Electromagnetism*, pp. 205–225, Berlin, Heidelberg: Springer Berlin Heidelberg, 1999.

[9] G. Turnbull, "Maxwell's equations [Scanning Our Past]," *Proceedings of the IEEE*, vol. 101, pp. 1801–1805, 7 2013.

[10] N. Sultanova, S. Kasarova, and I. Nikolov, "Dispersion properties of optical polymers," *Acta Physica Polonica A*, vol. 116, no. 4, pp. 585–587, 2009.

[11] T. Mosavirik, M. Soleimani, V. Nayyeri, S. H. Mirjahanmardi, and O. M. Ramahi, "Permittivity Characterization of Dispersive Materials Using Power Measurements," *IEEE Transactions on Instrumentation and Measurement*, vol. 70, no. November, 2021.

[12] P. I. Dankov, "Dielectric Anisotropy of Modern Microwave Substrates," in *Microwave and Millimeter Wave Technologies from Photonic Bandgap Devices to Antenna and Applications*, no. August, pp. 75–102, InTech, 3 2010.

[13] Y. T. Aladadi and M. A. Alkanhal, "Classification and characterization of electromagnetic materials," *Scientific Reports*, vol. 10, no. 1, 2020.

[14] R. Janaswamy, "Geometrical optics and Fermat's principle," *Engineering Electrodynamics*, vol. 2, no. April, pp. 9–1, 2020.

[15] R. C. Rumpf, "Engineering the Dispersion and Anisotropy of Periodic Electromagnetic Structures," in *Solid State Physics - Advances in Research and Applications* (R. E. Camley and R. L. Stamps, eds.), vol. 66, pp. 213–300, Academic press, 2015.

[16] R. A. Shelby, D. R. Smith, and S. Schultz, "Experimental verification of a negative index of refraction," *Science*, vol. 292, no. 5514, pp. 77–79, 2001.

[17] B. Varghese, O. Shramkova, P. Minard, L. Blondé, V. Drazic, and V. Allié, "Experimental observation of asymmetrical microwave jets and far-field distribution generated by a dual-material system," *Scientific Reports*, vol. 11, no. 1, pp. 1–8, 2021.

[18] V. Pacheco-Peña, B. Orazbayev, V. Torres, M. Beruete, and M. Navarro-Cía, "Ultracompact planoconcave zoned metallic lens based on the fishnet metamaterial," *Applied Physics Letters*, vol. 103, no. 18, 2013.

[19] B. Orazbayev, V. Pacheco-Peña, M. Beruete, and M. Navarro-Cía, "Exploiting the dispersion of the double-negative-index fishnet metamaterial to create a broadband low-profile metallic lens," *Optics Express*, vol. 23, no. 7, p. 8555, 2015.

[20] K. Lee, S.-Y. Lee, J. Jung, and B. Lee, "Plasmonic achromatic doublet lens," *Optics Express*, vol. 23, pp. 5800–5808, 3 2015.

[21] V. Pacheco-Pena and M. Beruete, "Controlling the direction of propagation of surface plasmons via graded index effective dielectric media," *2019 13th International Congress on Artificial Materials for Novel Wave Phenomena, Metamaterials 2019*, vol. 2019, no. 1, pp. X281–X283, 2019.

[22] H. Schneidewind, M. Zeisberger, M. Plidschun, S. Weidlich, and M. A. Schmidt, "Photonic candle – focusing light using nano-bore optical fibers," *Optics Express*, vol. 26, no. 24, p. 31706, 2018.

[23] A. Kwan, J. Dudley, and E. Lantz, "Who really discovered Snell's law?," *Physics World*, vol. 15, pp. 64–64, 4 2002.

[24] S. R. Wilk, "Claudius Ptolemy's Law of Refraction," *Optics & Photonics News*, vol. 15, no. October, pp. 14–17, 2004.

[25] M. Born and E. Wolf, *Principles Of Optics*. New York: Cambridge University Press, 7th ed., 1999.

[26] M. K. Feldman, S. Katyal, and M. S. Blackwood, "US Artifacts," *RadioGraphics*, vol. 29, pp. 1179–1189, 7 2009.

[27] S. W. Harun, M. Yasin, H. Z. Yang, and H. Ahm, "Fiber Optic Displacement Sensors and Their Applications," in *Fiber Optic Sensors*, no. February, InTech, 2 2012.

[28] G. Giusfredi, "Geometrical Optics," in *Physical optics*, UNITEXT for Physics, pp. 159–309, Cham: Springer International Publishing, 2019.

[29] F. Andres Callegari, "Thick Lenses Systems between Arbitrary Index of Refraction Optical Media. A Simple Optical Model for the Human Eye," *International Journal of Physics*, vol. 9, pp. 259–268, 11 2021.

[30] O. Darrigolo, "A History of Optics: From Greek Antiquity to the Nineteenth Century," *Oxford University Press*, 6 2012.

[31] R. Rashed, "A Pioneer in Anaclastics Ibn Sahl on Burning Mirrors and Lenses," *New Perspectives on the History of Islamic Science*, vol. 81, no. 3, pp. 271–298, 2019.

[32] M. Born, E. Wolf, A. B. Bhatia, P. C. Clemmow, D. Gabor, A. R. Stokes, A. M. Taylor, P. A. Wayman, and W. L. Wilcock, "Geometrical theory of optical imaging," in *Principles of Optics: Electromagnetic Theory of Propagation, Interference and Diffraction of Light*, p. 142–227, Cambridge University Press, 7 ed., 1999.

[33] P. S. Kildal, K. Jakobsen, and K. S. Rao, "Meniscus-Lens-Corrected Corrugated Horn: a Compact Feed for a Cassegrain Antenna.," *IEE Proceedings H: Microwaves Optics and Antennas*, vol. 131, no. 6 pt H, pp. 390–394, 1984.

[34] J. A. Riley, N. Healy, and V. Pacheco-Peña, "Plasmonic meniscus lenses," *Scientific Reports*, vol. 12, no. 1, p. 894, 2022.

[35] J. M. Babinet, "Mémoires d'optique météorologique," *Comptes Rendus Hebdomadaires des Séances de l'Académie des Sciences*, vol. 4, no. 18, p. 638–648, 1837.

[36] M. E. Brezinski, "Interference, Coherence, Diffraction, and Transfer functions," in *Optical Coherence Tomography*, pp. 71–94, Elsevier, 2006.

[37] H. Booker, "Slot aerials and their relation to complementary wire aerials (Babinet's principle)," *Journal of the Institution of Electrical Engineers - Part IIIA: Radiolocation*, vol. 93, no. 4, pp. 620–626, 1946.

[38] R. Janaswamy, "Duality principle and Babinet's principle," in *Engineering Electrodynamics*, pp. 6–1, IOP Publishing, 12 2020.

[39] T. Zentgraf, T. P. Meyrath, A. Seidel, S. Kaiser, H. Giessen, C. Rockstuhl, and F. Lederer, "Babinet's principle for optical frequency metamaterials and nanoantennas," *Physical Review B - Condensed Matter and Materials Physics*, vol. 76, no. 3, pp. 4–7, 2007.

[40] M. Hrtoň, A. Konečná, M. Horák, T. Šikola, and V. Křápek, "Plasmonic Antennas with Electric, Magnetic, and Electromagnetic Hot Spots Based on Babinet's Principle," *Physical Review Applied*, vol. 13, p. 054045, 5 2020.

[41] M. Horák, V. Křápek, M. Hrtoň, A. Konečná, F. Ligmajer, M. Stöger-Pollach, T. Šamořil, A. Paták, Z. Édes, O. Metelka, J. Babocký, and T. Šikola, "Limits of Babinet's principle for solid and hollow plasmonic antennas," *Scientific Reports*, vol. 9, no. 1, pp. 1–11, 2019.

[42] J. D. Ortiz, J. P. del Risco, J. D. Baena, and R. Marqués, "Extension of Babinet's principle for plasmonic metasurfaces," *Applied Physics Letters*, vol. 119, p. 161103, 10 2021.

[43] J. A. Riley, M. Horák, V. Křápek, N. Healy, and V. Pacheco-Peña, "Plasmonic sensing using Babinet's principle," *Nanophotonics*, vol. 12, pp. 3895–3909, 10 2023.

[44] W. E. Kock, "Metal-Lens Antennas," *IEEE*, vol. 34, no. 11, pp. 828–836, 1946.

[45] V. G. Veselago, "The Electrodynamics of Substances with Simultaneously Negative Values of ϵ and μ," *Soviet Physics Uspekhi*, vol. 10, pp. 509–514, 4 1968.

[46] D. R. Smith, W. J. Padilla, D. C. Vier, S. C. Nemat-Nasser, and S. Schultz, "Composite Medium with Simultaneously Negative Permeability and Permittivity," *Physical Review Letters*, vol. 84, pp. 4184–4187, 5 2000.

[47] R. Kshetrimayum, "A brief intro to metamaterials," *IEEE Potentials*, vol. 23, pp. 44–46, 1 2005.

[48] M. G. Silveirinha and N. Engheta, "Theory of supercoupling, squeezing wave energy, and field confinement in narrow channels and tight bends using ε near-zero metamaterials," *Physical Review B - Condensed Matter and Materials Physics*, vol. 76, no. 24, pp. 1–17, 2007.

[49] J. Wang and J. Du, "Plasmonic and dielectric metasurfaces: Design, Fabrication and Applications," *Applied Sciences (Switzerland)*, vol. 6, no. 9, 2016.

[50] F. Falcone, T. Lopetegi, M. A. G. Laso, J. D. Baena, J. Bonache, M. Beruete, R. Marqués, F. Martín, and M. Sorolla, "Babinet Principle Applied to the Design of Metasurfaces and Metamaterials," *Physical Review Letters*, vol. 93, p. 197401, 11 2004.

[51] M. M. Bait-Suwailam, "Electromagnetic Field Interaction with Metamaterials," in *Electromagnetic Fields and Waves*, pp. 0–19, IntechOpen, 5 2019.

[52] D. R. Smith, J. B. Pendry, and M. C. Wiltshire, "Metamaterials and negative refractive index," *Science*, vol. 305, no. 5685, pp. 788–792, 2004.

[53] G. V. Eleftheriades, M. A. Antoniades, and F. Qureshi, "Antenna applications of negative-refractive-index transmission-line structures," *IET Microwaves, Antennas and Propagation*, vol. 1, no. 1, pp. 12–22, 2007.

[54] J. B. Pendry, "Negative Refraction Makes a Perfect Lens," *Physical Review Letters*, vol. 85, pp. 3966–3969, 10 2000.

[55] J. Krupka, P. Aleshkevych, B. Salski, P. Kopyt, and A. Pacewicz, "Ferromagnetic Resonance Revised – Electrodynamic Approach," *Scientific Reports*, vol. 7, p. 5750, 7 2017.

[56] S. S. Islam, M. R. I. Faruque, M. T. Islam, and T. Alam, "A new mu-negative metamaterial," in *2015 2nd International Conference on Electrical Information and Communication Technologies (EICT)*, no. Eict, pp. 269–272, IEEE, 12 2015.

[57] L. Solymar and E. Shamonina, "A bird's-eye view of metamaterials," in *Waves in Metamaterials*, pp. 35–74, Oxford University PressOxford, 1 2009.

[58] C. R. Simovski, P. A. Belov, A. V. Atrashchenko, and Y. S. Kivshar, "Wire metamaterials: Physics and applications," *Advanced Materials*, vol. 24, no. 31, pp. 4229–4248, 2012.

[59] R. W. Ziolkowski, "Propagation in and scattering from a matched metamaterial having a zero index of refraction," *Physical Review E - Statistical Physics, Plasmas, Fluids, and Related Interdisciplinary Topics*, vol. 70, no. 4, p. 12, 2004.

[60] N. Engheta and R. W. Ziolkowski, *Metamaterials: Physics and Engineering Explorations*. Wiley-IEEE Press, 2006.

[61] S. Enoch, G. Tayeb, P. Sabouroux, N. Guérin, and P. Vincent, "A Metamaterial for Directive Emission," *Physical Review Letters*, vol. 89, no. 21, pp. 1–4, 2002.

[62] H. Hajian, E. Ozbay, and H. Caglayan, "Enhanced transmission and beaming via a zero-index photonic crystal," *Applied Physics Letters*, vol. 109, 7 2016.

[63] M. Z. Alam, I. De Leon, and R. W. Boyd, "Large optical nonlinearity of indium tin oxide in its epsilon-near-zero region," *Science*, vol. 352, no. 6287, pp. 795–797, 2016.

[64] W. Zhu, I. D. Rukhlenko, and M. Premaratne, "Application of zero-index metamaterials for surface plasmon guiding," *Applied Physics Letters*, vol. 102, no. 1, 2013.

[65] R. Maas, J. Parsons, N. Engheta, and A. Polman, "Experimental realization of an epsilon-near-zero metamaterial at visible wavelengths," *Nature Photonics*, vol. 7, no. 11, pp. 907–912, 2013.

[66] A. Alù, M. G. Silveirinha, and N. Engheta, "Transmission-line analysis of ε -near-zero-filled narrow channels," *Physical Review E - Statistical, Nonlinear, and Soft Matter Physics*, vol. 78, no. 1, pp. 1–10, 2008.

[67] D. M. Pozar, *Microwave Engineering*. Wiley, 4 ed., 1998.

[68] M. Nicolussi, J. A. Riley, and V. Pacheco-Peña, "Unidirectional transparency in epsilon-near-zero based rectangular waveguides induced by parity-time symmetry," *Applied Physics Letters*, vol. 119, p. 263507, 12 2021.

[69] D. Walls and G. J. Milburn, "Quantum Theory of the Laser," in *Quantum Optics*, pp. 231–246, Berlin, Heidelberg: Springer Berlin Heidelberg, 1994.

[70] K. Amsalu and S. Palani, "A review on photonics and its applications," *Materials Today: Proceedings*, vol. 33, pp. 3372–3377, 2020.

[71] B. Anvari, "Grand Challenges and Opportunities in Biophotonics," *Frontiers in Photonics*, vol. 2, pp. 1263–1268, 6 2021.

[72] K. Goda, "Biophotonics and beyond," *APL Photonics*, vol. 4, no. 5, 2019.

[73] N. S. Hill, M. V. Cowley, N. Gluck, M. H. Fsadni, W. Clarke, Y. Hu, M. J. Wolf, N. Healy, M. Freitag, T. J. Penfold, G. Richardson, A. B. Walker, P. J. Cameron, and P. Docampo, "Ionic Accumulation as a Diagnostic Tool in Perovskite Solar Cells: Characterizing Band Alignment with Rapid Voltage Pulses," *Advanced Materials*, vol. 35, no. 32, 2023.

[74] E. B. Neergaard and S. Harly, "Optical Data Processing," *Acta Radiologica*, vol. 12, pp. 271–277, 1972.

[75] R. G. MacDonald, A. Yakovlev, and V. Pacheco-Peña, "Amplitude-Controlled Electromagnetic Pulse Switching Using Waveguide Junctions for High-Speed Computing Processes," *Advanced Intelligent Systems*, vol. 4, 12 2022.

[76] Y. Shi, Y. Zhang, Y. Wan, Y. Yu, Y. Zhang, X. Hu, X. Xiao, H. Xu, L. Zhang, and B. Pan, "Silicon photonics for high-capacity data communications," *Photonics Research*, vol. 10, no. 9, p. A106, 2022.

[77] A. Yelon, K. N. Piyakis, and E. Sacher, "Surface plasmons in Drude metals," *Surface Science*, vol. 569, no. 1-3, pp. 47–55, 2004.

[78] M. Eldlio, F. Che, and M. Cada, "Drude-Lorentz Model of Semiconductor Optical Plasmons," in *IAENG Transactions on Engineering Sciences* (S.-I. Ao, A. H.-S. Chan, H. Katagiri, and L. Xu, eds.), pp. 41–49, CRC Press, 4 2014.

[79] S. J. Youn, T. H. Rho, B. I. Min, and K. S. Kim, "Extended Drude model analysis of noble metals," *Physica Status Solidi (B) Basic Research*, vol. 244, no. 4, pp. 1354–1362, 2007.

[80] P. Drude, "Zur Elektronentheorie der Metalle," *Annalen der Physik*, vol. 306, no. 3, pp. 566–613, 1900.

[81] P. Fulde, "The Independent-Electron Approximation," in *Electron Correlations in Molecules and Solids*, pp. 5–38, Springer Berlin Heidelberg, 1993.

[82] H. S. Sehmi, W. Langbein, and E. A. Muljarov, "Optimizing the Drude-Lorentz model for material permittivity: Method, program, and examples for gold, silver, and copper," *Physical Review B*, vol. 95, no. 11, pp. 1–8, 2017.

[83] L. Tong, H. Wei, and H. Xu, "Fundamentals of Plasmonics," in *Nanophotonics*, pp. 1–20, Jenny Stanford Publishing, 11 2017.

[84] S. A. Maier, *Plasmonics: Fundamentals and Applications*. New York, NY: Springer US, 4 2007.

[85] L. Novotny and B. Hecht, "Surface plasmons," in *Principles of Nano-Optics*, no. May, pp. 369–413, Cambridge: Cambridge University Press, 9 2012.

[86] E. Ozbay, "Plasmonics: Merging Photonics and Electronics at Nanoscale Dimensions," *Science*, vol. 311, pp. 189–193, 1 2006.

[87] G. Mie, "Contributions to the Optics of Turbid Media, Particularly of Colloidal Metal solutions," *Annalen der Physik*, vol. 330, pp. 377–445, 1 1908.

[88] F. Y. Alzoubi, A. A. Ahmad, I. A. Aljarrah, A. B. Migdadi, and Q. M. Al-Bataineh, "Localize surface plasmon resonance of silver nanoparticles using Mie theory," *Journal of Materials Science: Materials in Electronics*, vol. 34, no. 32, pp. 1–10, 2023.

[89] M. Faraday, "X. The Bakerian Lecture. —Experimental relations of gold (and other metals) to light," *Philosophical Transactions of the Royal Society of London*, vol. 147, pp. 145–181, 12 1857.

[90] S. A. Maier, "Localized Surface Plasmons," in *Plasmonics: Fundamentals and Applications*, pp. 65–88, New York, NY: Springer US, 2007.

[91] P. Dombi, Z. Pápa, J. Vogelsang, S. V. Yalunin, M. Sivis, G. Herink, S. Schäfer, P. Groß, C. Ropers, and C. Lienau, "Strong-field nano-optics," *Reviews of Modern Physics*, vol. 92, p. 025003, 6 2020.

[92] A. V. Zayats and I. I. Smolyaninov, "Near-field photonics: Surface plasmon polaritons and localized surface plasmons," *Journal of Optics A: Pure and Applied Optics*, vol. 5, no. 4, 2003.

[93] M. Horák, V. Čalkovský, J. Mach, V. Křápek, and T. Šikola, "Plasmonic Properties of Individual Gallium Nanoparticles," *Journal of Physical Chemistry Letters*, vol. 14, no. 8, pp. 2012–2019, 2023.

[94] G. V. Naik, V. M. Shalaev, and A. Boltasseva, "Alternative plasmonic materials: Beyond gold and silver," *Advanced Materials*, vol. 25, no. 24, pp. 3264–3294, 2013.

[95] U. Leonhardt, "Invisibility cup," *Nature Photonics*, vol. 1, pp. 207–208, 4 2007.

[96] D. M. Kim, J. S. Park, S.-W. Jung, J. Yeom, and S. M. Yoo, "Biosensing Applications Using Nanostructure-Based Localized Surface Plasmon Resonance Sensors," *Sensors*, vol. 21, p. 3191, 5 2021.

[97] K. A. Willets and R. P. Van Duyne, "Localized surface plasmon resonance spectroscopy and sensing," *Annual Review of Physical Chemistry*, vol. 58, pp. 267–297, 2007.

[98] W. Srituravanich, N. Fang, S. Durant, M. Ambati, C. Sun, and X. Zhang, "Sub-100 nm lithography using ultrashort wavelength of surface plasmons," *Journal of Vacuum Science & Technology B: Microelectronics and Nanometer Structures*, vol. 22, no. 6, p. 3475, 2004.

[99] J. A. Dionne, A. Baldi, B. Baum, C. S. Ho, V. Janković, G. V. Naik, T. Narayan, J. A. Scholl, and Y. Zhao, "Localized fields, global impact: Industrial applications of resonant plasmonic materials," *MRS Bulletin*, vol. 40, no. 12, pp. 1138–1145, 2015.

[100] V. Pacheco-Peña, I. V. Minin, O. V. Minin, and M. Beruete, "Comprehensive analysis of photonic nanojets in 3D dielectric cuboids excited by surface plasmons," *Annalen der Physik*, vol. 528, pp. 684–692, 10 2016.

[101] B. J. Roxworthy, K. D. Ko, A. Kumar, K. H. Fung, E. K. Chow, G. L. Liu, N. X. Fang, and K. C. Toussaint, "Application of plasmonic bowtie nanoantenna arrays for optical trapping, stacking, and sorting," *Nano Letters*, vol. 12, no. 2, pp. 796–801, 2012.

[102] B. M. Ross and L. P. Lee, "Comparison of near- and far-field measures for plasmon resonance of metallic nanoparticles," *Optics Letters*, vol. 34, no. 7, p. 896, 2009.

[103] M. Svedendahl, S. Chen, A. Dmitriev, and M. Käll, "Refractometric sensing using propagating versus localized surface plasmons: A direct comparison," *Nano Letters*, vol. 9, no. 12, pp. 4428–4433, 2009.

[104] L. Liu, B. Wang, X. Cao, X. Xu, and Y. Wang, "Comparison investigation of near- and far-field properties for plasmon resonance of silver nanosphere dimers," *Photonics and Nanostructures - Fundamentals and Applications*, vol. 10, no. 1, pp. 16–24, 2012.

[105] M. Kadic, S. Guenneau, and S. Enoch, "Transformational plasmonics: cloak, concentrator and rotator for SPPs," *Optics Express*, vol. 18, no. 11, p. 12027, 2010.

[106] G. Zhen, P. Zhou, X. Luo, J. Xie, and L. Deng, "Modes Coupling Analysis of Surface Plasmon Polaritons Based Resonance Manipulation in Infrared Metamaterial Absorber," *Scientific Reports*, vol. 7, no. April, pp. 1–8, 2017.

[107] A. Sommerfeld, "Ueber die Fortpflanzung elektrodynamischer Wellen längs eines Drahtes," *Annalen der Physik und Chemie*, vol. 303, no. 2, pp. 233–290, 1899.

[108] J. Zenneck, "Über die Fortpflanzung ebener elektromagnetischer Wellen längs einer ebenen Leiterfläche und ihre Beziehung zur drahtlosen Telegraphie," *Annalen der Physik*, vol. 328, no. 10, pp. 846–866, 1907.

[109] U. Fano, "The Theory of Anomalous Diffraction Gratings and of Quasi-Stationary Waves on Metallic Surfaces (Sommerfeld's Waves)," *Journal of the Optical Society of America*, vol. 31, p. 213, 3 1941.

[110] R. H. Ritchie, "Plasma Losses by Fast Electrons in Thin Films," *Physical Review*, vol. 106, pp. 874–881, 6 1957.

[111] R. H. Ritchie, E. T. Arakawa, J. J. Cowan, and R. N. Hamm, "Surface-plasmon resonance effect in grating diffraction," *Physical Review Letters*, vol. 21, no. 22, pp. 1530–1533, 1968.

[112] E. Kretschmann and H. Raether, "Radiative Decay of Non Radiative Surface Plasmons Excited by Light," *Zeitschrift fur Naturforschung - Section A Journal of Physical Sciences*, vol. 23, no. 12, pp. 2135–2136, 1968.

[113] S. A. Maier, "Excitation of Surface Plasmon Polaritons at Planar Interfaces," in *Plasmonics: Fundamentals and Applications*, pp. 39–52, New York, NY: Springer US, 2007.

[114] K. S. Makarenko, T. X. Hoang, T. J. Duffin, A. Radulescu, V. Kalathingal, H.-S. Chu, and C. A. Nijhuis, "Surface Plasmon Polariton Excitation and Light Emission in Metal-Insulator-Metal Tunnelling Junctions," *Advanced Science*, vol. Accepted, 2020.

[115] V. S. Volkov, J. Gosciniak, S. I. Bozhevolnyi, S. G. Rodrigo, L. Martín-Moreno, F. J. García-Vidal, E. Devaux, and T. W. Ebbesen, "Plasmonic candle: towards efficient nanofocusing with channel plasmon polaritons," *New Journal of Physics*, vol. 11, p. 113043, 11 2009.

[116] S. A. Maier, "Surface Plasmon Polaritons at Metal / Insulator Interfaces," in *Plasmonics: Fundamentals and Applications*, pp. 21–37, New York, NY: Springer US, 2007.

[117] B. R. Masters, "Concepts and Criteria of Resolution," in *Superresolution Optical Microscopy*, vol. 227, pp. 13–32, Springer Cham, 1 ed., 2020.

[118] A. L. Dávalos and D. Zanette, *Fundamentals of Electromagnetism*. Berlin, Heidelberg: Springer Berlin Heidelberg, 1999.

[119] A. Pimenov and A. Loidl, "Focusing of millimeter-wave radiation beyond the Abbe barrier," *Applied Physics Letters*, vol. 83, no. 20, pp. 4122–4124, 2003.

[120] Z. Zheng, B. F. Zhang, H. Chen, J. Ding, and H. T. Wang, "Optical trapping with focused Airy beams," *Applied Optics*, vol. 50, no. 1, pp. 43–49, 2011.

[121] I. V. Minin, Y. E. Geints, A. A. Zemlyanov, and O. V. Minin, "Specular-reflection photonic nanojet: physical basis and optical trapping application," *Optics Express*, vol. 28, no. 15, p. 22690, 2020.

[122] "Beyond the diffraction limit," *Nature Photonics*, vol. 3, pp. 361–361, 7 2009.

[123] M. Kim and J. Rho, "Metamaterials and imaging," *Nano Convergence*, vol. 2, p. 22, 12 2015.

[124] L. Solymar and E. Shamonina, "Subwavelength imaging," in *Waves in Metamaterials*, pp. 155–198, Oxford University PressOxford, 1 2009.

[125] D. Maystre and S. Enoch, "Perfect lenses made with left-handed materials: Alice's mirror?," *Journal of the Optical Society of America A*, vol. 21, p. 122, 1 2004.

[126] I. Minin and O. Minin, "SPP Diffractive Lens as One of the Basic Devices for Plasmonic Information Processing," in *Diffractive Optics and Nanophotonics*, SpringerBriefs in Physics, pp. 55–60, Cham: Springer International Publishing, 2016.

[127] D. K. Gramotnev and S. I. Bozhevolnyi, "Plasmonics beyond the diffraction limit," *Nature Photonics*, vol. 4, no. 2, pp. 83–91, 2010.

[128] B. Lee, S. Kim, H. Kim, and Y. Lim, "The use of plasmonics in light beaming and focusing," *Progress in Quantum Electronics*, vol. 34, no. 2, pp. 47–87, 2010.

[129] X. Zhang and Z. Liu, "Superlenses to overcome the diffraction limit," *Nature Materials*, vol. 7, pp. 435–441, 6 2008.

[130] N. Fang, H. Lee, C. Sun, and X. Zhang, "Sub–Diffraction-Limited Optical Imaging with a Silver Superlens," *Science*, vol. 308, no. April, pp. 534–538, 2005.

[131] G. Chen, Z.-Q. Wen, and C.-W. Qiu, "Superoscillation: from physics to optical applications," *Light: Science & Applications*, vol. 8, p. 56, 6 2019.

[132] I. Minin and O. Minin, "Subwavelength Focusing Properties of Diffractive Photonic Crystal Lens," in *Diffractive Optics and Nanophotonics*, vol. Part F847, pp. 21–30, Springer Cham, 1 ed., 2016.

[133] I. Minin and O. Minin, "3D Diffractive Lenses to Overcome the 3D Abby Diffraction Limit," in *Diffractive Optics and Nanophotonics*, vol. Part F847, pp. 7–20, Springer Cham, 2016.

[134] Z. Wang, W. Guo, L. Li, B. Luk'yanchuk, A. Khan, Z. Liu, Z. Chen, and M. Hong, "Optical virtual imaging at 50 nm lateral resolution with a white-light nanoscope," *Nature Communications*, vol. 2, p. 218, 3 2011.

[135] A. V. Maslov and V. N. Astratov, "Imaging of sub-wavelength structures radiating coherently near microspheres," *Applied Physics Letters*, vol. 108, no. 5, 2016.

[136] O. V. Minin and I. V. Minin, "Optical Phenomena in Mesoscale Dielectric Particles," *Photonics*, vol. 8, p. 591, 12 2021.

[137] X. Hao, C. Kuang, X. Liu, H. Zhang, and Y. Li, "Microsphere based microscope with optical super-resolution capability," *Applied Physics Letters*, vol. 99, 11 2011.

[138] H. E. Burton, "The Optics of Euclid," *Journal of the Optical Society of America*, vol. 35, p. 357, 5 1945.

[139] M. V. Berry and N. L. Balazs, "Nonspreading wave packets," *American Journal of Physics*, vol. 47, pp. 264–267, 3 1979.

[140] G. A. Siviloglou, J. Broky, A. Dogariu, and D. N. Christodoulides, "Observation of Accelerating Airy Beams," *Physical Review Letters*, vol. 99, p. 213901, 11 2007.

[141] N. K. Efremidis, Z. Chen, M. Segev, and D. N. Christodoulides, "Airy beams and accelerating waves: an overview of recent advances," *Optica*, vol. 6, no. 5, p. 686, 2019.

[142] Z. Chen, A. Taflove, and V. Backman, "Photonic nanojet enhancement of backscattering of light by nanoparticles: a potential novel visible-light ultramicroscopy technique," *Optics Express*, vol. 12, no. 7, p. 1214, 2004.

[143] O. V. Minin and I. V. Minin, *The Photonic Hook*. SpringerBriefs in Physics, Cham: Springer International Publishing, 2021.

[144] W. Aljuaid, J. A. Riley, N. Healy, and V. Pacheco-Peña, "On-fiber high-resolution photonic nanojets via high refractive index dielectrics," *Optics Express*, vol. 30, no. 24, p. 43678, 2022.

[145] D. Ju, H. Pei, Y. Jiang, and X. Sun, "Controllable and enhanced nanojet effects excited by surface plasmon polariton," *Applied Physics Letters*, vol. 102, p. 171109, 4 2013.

[146] M. Salhi and P. G. Evans, "Photonic nanojet as a result of a focused near-field diffraction," *Journal of the Optical Society of America B*, vol. 36, no. 4, p. 1031, 2019.

[147] C.-Y. Liu, T.-P. Yen, O. V. Minin, and I. V. Minin, "Engineering photonic nanojet by a graded-index micro-cuboid," *Physica E: Low-dimensional Systems and Nanostructures*, vol. 98, pp. 105–110, 4 2018.

[148] A. Heifetz, S.-C. Kong, A. V. Sahakian, A. Taflove, and V. Backman, "Photonic Nanojets," *Journal of Computational and Theoretical Nanoscience*, vol. 6, pp. 1979–1992, 9 2009.

[149] V. Pacheco-Peña, M. Beruete, I. V. Minin, and O. V. Minin, "Terajets produced by dielectric cuboids," *Applied Physics Letters*, vol. 105, no. 8, pp. 1–5, 2014.

[150] V. Pacheco-Peña, M. Beruete, I. V. Minin, and O. V. Minin, "Multifrequency focusing and wide angular scanning of terajets," *Optics Letters*, vol. 40, no. 2, p. 245, 2015.

[151] H. H. Nguyen Pham, S. Hisatake, O. V. Minin, T. Nagatsuma, and I. V. Minin, "Asymmetric phase anomaly of terajet generated from dielectric cube under oblique illumination," *Applied Physics Letters*, vol. 110, no. 20, 2017.

[152] A. Darafsheh, "Photonic nanojets and their applications," *JPhys Photonics*, vol. 3, no. 2, 2021.

[153] Y. E. Geints, E. K. Panina, and A. A. Zemlyanov, "Comparative analysis of spatial shapes of photonic jets from spherical dielectric microparticles," *Atmospheric and Oceanic Optics*, vol. 25, pp. 338–345, 9 2012.

[154] C.-Y. Liu, "Photonic jets produced by dielectric micro cuboids," *Applied Optics*, vol. 54, p. 8694, 10 2015.

[155] C. Liu, "ULTRA-ELONGATED PHOTONIC NANOJETS GENERATED BY A GRADED-INDEX MICROELLIPSOID," *Progress In Electromagnetics Research Letters*, vol. 37, no. January, pp. 153–165, 2013.

[156] B. S. Luk'yanchuk, R. Paniagua-Domínguez, I. Minin, O. Minin, and Z. Wang, "Refractive index less than two: photonic nanojets yesterday, today and tomorrow [Invited]," *Optical Materials Express*, vol. 7, p. 1820, 6 2017.

[157] A. Devilez, B. Stout, N. Bonod, and E. Popov, "Spectral analysis of three-dimensional photonic jets," *Optics Express*, vol. 16, p. 14200, 9 2008.

[158] V. Pacheco-Peña and M. Beruete, "Photonic nanojets with mesoscale high-index dielectric particles," *Journal of Applied Physics*, vol. 125, no. 8, 2019.

[159] V. Gašparić, T. G. Mayerhöfer, D. Zopf, D. Ristić, J. Popp, and M. Ivanda, "To generate a photonic nanojet outside a high refractive index microsphere illuminated by a Gaussian beam," *Optics Letters*, vol. 47, p. 2534, 5 2022.

[160] L. Yue, O. V. Minin, Z. Wang, J. N. Monks, A. S. Shalin, and I. V. Minin, "Photonic hook: a new curved light beam," *Optics Letters*, vol. 43, no. 4, p. 771, 2018.

[161] Y. E. Geints, I. V. Minin, and O. V. Minin, "Tailoring 'photonic hook' from Janus dielectric microbar," *Journal of Optics (United Kingdom)*, vol. 22, no. 6, 2020.

[162] I. V. Minin, O. V. Minin, D. S. Ponomarev, and I. A. Glinskiy, "Photonic Hook Plasmons: A New Curved Surface Wave," *Annalen der Physik*, vol. 530, no. 12, pp. 1–5, 2018.

[163] W. Liu, D. N. Neshev, I. V. Shadrivov, A. E. Miroshnichenko, and Y. S. Kivshar, "Plasmonic Airy beam manipulation in linear optical potentials," *Optics Letters*, vol. 36, p. 1164, 4 2011.

[164] V. Pacheco-Peña, J. A. Riley, C.-Y. Liu, O. V. Minin, and I. V. Minin, "Diffraction limited photonic hook via scattering and diffraction of dual-dielectric structures," *Scientific Reports*, vol. 11, p. 20278, 12 2021.

[165] G. Gu, P. Zhang, S. Chen, Y. Zhang, and H. Yang, "Inflection point: a perspective on photonic nanojets," *Photonics Research*, vol. 9, p. 1157, 7 2021.

[166] A. Tellal, O. Ziane, S. Jradi, O. Stephan, and P. L. Baldeck, "Quadratic phase modulation and diffraction-limited microfocusing generated by pairs of subwavelength dielectric scatterers," *Nanophotonics*, vol. 8, no. 6, pp. 1051–1061, 2019.

[167] J.-J. Greffet, "Introduction to Surface Plasmon Theory," in *Springer Series in Optical Sciences*, vol. 167, pp. 105–148, Springer, 2012.

[168] Y. Liu, T. Zentgraf, G. Bartal, and X. Zhang, "Transformational Plasmon Optics," *Nano Letters*, vol. 10, pp. 1991–1997, 6 2010.

[169] S. V. Boriskina, T. A. Cooper, L. Zeng, G. Ni, J. K. Tong, Y. Tsurimaki, Y. Huang, L. Meroueh, G. Mahan, and G. Chen, "Losses in plasmonics: from mitigating energy dissipation to embracing loss-enabled functionalities," *Advances in Optics and Photonics*, vol. 9, no. 4, p. 775, 2017.

[170] M. G. Hudedmani and B. S. Pagad, "Plasmonics: A Path to Replace Electronics and Photonics by Scalable Ultra-fast Technology," *Advanced Journal of Graduate Research*, vol. 7, no. 1, pp. 37–44, 2019.

[171] J. Zhang, L. Zhang, and W. Xu, "Surface plasmon polaritons: physics and applications," *Journal of Physics D: Applied Physics*, vol. 45, p. 113001, 3 2012.

[172] Z. Liu, J. M. Steele, W. Srituravanich, Y. Pikus, C. Sun, and X. Zhang, "Focusing surface plasmons with a plasmonic lens," *Nano Letters*, vol. 5, no. 9, pp. 1726–1729, 2005.

[173] W.-B. Shi, T.-Y. Chen, H. Jing, R.-W. Peng, and M. Wang, "Dielectric lens guides in-plane propagation of surface plasmon polaritons," *Optics Express*, vol. 25, no. 5, p. 5772, 2017.

[174] A. Demetriadou and A. A. Kornyshev, "Principles of nanoparticle imaging using surface plasmons," *New Journal of Physics*, vol. 17, p. 013041, 1 2015.

[175] S. Hayashi, D. V. Nesterenko, and Z. Sekkat, "Waveguide-coupled surface plasmon resonance sensor structures: Fano lineshape engineering for ultrahigh-resolution sensing," *Journal of Physics D: Applied Physics*, vol. 48, no. 32, 2015.

[176] Z. Fang, F. Lin, S. Huang, W. Song, and X. Zhu, "Focusing surface plasmon polariton trapping of colloidal particles," *Applied Physics Letters*, vol. 94, 2 2009.

[177] W. Liu, D. N. Neshev, A. E. Miroshnichenko, I. V. Shadrivov, and Y. S. Kivshar, "Polychromatic nanofocusing of surface plasmon polaritons," *Physical Review B - Condensed Matter and Materials Physics*, vol. 83, no. 7, pp. 2–5, 2011.

[178] V. Pacheco-Peña and M. Navarro-Cía, "Understanding quantum emitters in plasmonic nanocavities with conformal transformation: Purcell enhancement and forces," *Nanoscale*, vol. 10, no. 28, pp. 13607–13616, 2018.

[179] T. V. Teperik, A. Archambault, F. Marquier, and J. J. Greffet, "Huygens-Fresnel principle for surface plasmons," *Optics Express*, vol. 17, pp. 17483–17490, 9 2009.

[180] T. Zentgraf, Y. Liu, M. H. Mikkelsen, J. Valentine, and X. Zhang, "Plasmonic Luneburg and Eaton lenses," *Nature Nanotechnology*, vol. 6, pp. 151–155, 3 2011.

[181] H. R. Philipp, "Optical Properties of Silicon Nitride," *Journal of The Electrochemical Society*, vol. 120, no. 2, p. 295, 1973.

[182] S. A. Maier, "Electromagnetics of Metals," in *Plasmonics: Fundamentals and Applications*, pp. 5–19, New York, NY: Springer US, 2007.

[183] A. V. Krasavin and A. V. Zayats, "Silicon-based plasmonic waveguides," *Optics Express*, vol. 18, no. 11, p. 11791, 2010.

[184] J. J. Burke, G. I. Stegeman, and T. Tamir, "Surface-polariton-like waves guided by thin, lossy metal films," *Physical Review B*, vol. 33, no. 8, pp. 5186–5201, 1986.

[185] B. Vohnsen, "A short history of optics," *Physica Scripta T*, vol. T109, no. June, pp. 75–79, 2004.

[186] T. H. Jamieson, "Thick meniscus field correctors," *Applied Optics*, vol. 21, p. 2799, 8 1982.

[187] P. Kallo, "Field curvature correction by meniscus lenses," *Periodica Polytechnica Mechanical Engineering*, vol. 28, no. 1, pp. 115–118, 1984.

[188] V. Pacheco-Peña and M. Beruete, "Steering surface plasmons with a graded index dielectric medium," *Journal of Physics D: Applied Physics*, vol. 51, no. 48, p. 485101, 2018.

[189] R. Ilinsky, "Gradient-index meniscus lens free of spherical aberration," *Journal of Optics A: Pure and Applied Optics*, vol. 2, no. 5, pp. 449–451, 2000.

[190] J. L. S. Cambridge, G. Optics, G. O. Berlin, and J. L. Synge, "Geometrical theory of optical imaging," in *Principles of Optics*, pp. 142–227, Cambridge University Press, 12 2019.

[191] V. Klimov, "Surface plasmons," in *Nanoplasmonics*, pp. 25–60, Jenny Stanford Publishing, 9 2014.

[192] J. T. Fourkas, J. Gao, Z. Han, H. Liu, B. Marmiroli, M. J. Naughton, J. S. Petersen, Y. Sun, A. Vagilio Pret, and Y. Zheng, "Grand Challenges in Nanofabrication: There Remains Plenty of Room at the Bottom," *Frontiers in Nanotechnology*, vol. 3, no. October, pp. 2–5, 2021.

[193] A. Sarangan, "Nanofabrication," in *Fundamentals and Applications of Nanophotonics*, pp. 149–184, Elsevier, 2016.

[194] J. Henzie, J. Lee, M. H. Lee, W. Hasan, and T. W. Odom, "Nanofabrication of plasmonic structures," *Annual Review of Physical Chemistry*, vol. 60, pp. 147–165, 2009.

[195] H. Ammari, M. Ruiz, S. Yu, and H. Zhang, "Mathematical analysis of plasmonic resonances for nanoparticles: The full Maxwell equations," *Journal of Differential Equations*, vol. 261, pp. 3615–3669, 9 2016.

[196] L. Tian, C. Wang, H. Zhao, F. Sun, H. Dong, K. Feng, P. Wang, G. He, and G. Li, "Rational Approach to Plasmonic Dimers with Controlled Gap Distance, Symmetry, and Capability of Precisely Hosting Guest Molecules in Hotspot Regions," *Journal of the American Chemical Society*, vol. 143, no. 23, pp. 8631–8638, 2021.

[197] B. Gerislioglu, L. Dong, A. Ahmadivand, H. Hu, P. Nordlander, and N. J. Halas, "Monolithic Metal Dimer-on-Film Structure: New Plasmonic Properties Introduced by the Underlying Metal," *Nano Letters*, vol. 20, no. 3, pp. 2087–2093, 2020.

[198] E. Cortés, L. V. Besteiro, A. Alabastri, A. Baldi, G. Tagliabue, A. Demetriadou, and P. Narang, "Challenges in Plasmonic Catalysis," *ACS Nano*, vol. 14, no. 12, pp. 16202–16219, 2020.

[199] S. Alekseeva, I. I. Nedrygailov, and C. Langhammer, "Single Particle Plasmonics for Materials Science and Single Particle Catalysis," *ACS Photonics*, vol. 6, no. 6, pp. 1319–1330, 2019.

[200] H. Ditlbacher, J. R. Krenn, B. Lamprecht, A. Leitner, and F. R. Aussenegg, "Spectrally coded optical data storage by metal nanoparticles," *Optics Letters*, vol. 25, p. 563, 4 2000.

[201] F. Liu, X. Zhang, Y. Mu, J. Lin, M. Wang, and H. Ma, "Complementary Dark and Bright Plasmonic Nanocavities with Controllable Energy Exchange for SERS Sensing," *Advanced Optical Materials*, vol. 8, no. 16, pp. 1–11, 2020.

[202] A. S. Grimault, A. Vial, and M. L. De La Chapelle, "Modeling of regular gold nanostructures arrays for SERS applications using a 3D FDTD method," *Applied Physics B: Lasers and Optics*, vol. 84, no. 1-2, pp. 111–115, 2006.

[203] Y. E. Monfared and M. Qasymeh, "Graphene-assisted infrared plasmonic metamaterial absorber for gas detection," *Results in Physics*, vol. 23, no. February, p. 103986, 2021.

[204] A. Tittl, H. Giessen, and N. Liu, "Plasmonic gas and chemical sensing," *Nanophotonics*, vol. 3, no. 3, pp. 157–180, 2014.

[205] S. Celiksoy, W. Ye, K. Wandner, K. Kaefer, and C. Sönnichsen, "Intensity-Based Single Particle Plasmon Sensing," *Nano Letters*, vol. 21, no. 5, pp. 2053–2058, 2021.

[206] X. Xu, X. Liu, Y. Li, and Y. Ying, "A simple and rapid optical biosensor for detection of aflatoxin B1 based on competitive dispersion of gold nanorods," *Biosensors and Bioelectronics*, vol. 47, pp. 361–367, 2013.

[207] J. H. Lee, H. Y. Cho, H. K. Choi, J. Y. Lee, and J. W. Choi, "Application of gold nanoparticle to plasmonic biosensors," *International Journal of Molecular Sciences*, vol. 19, no. 7, 2018.

[208] H. Wang, "Plasmonic refractive index sensing using strongly coupled metal nanoantennas: Nonlocal limitations," *Scientific Reports*, vol. 8, no. 1, pp. 1–8, 2018.

[209] R. X. Zhang, L. Sun, C. L. Du, T. Y. Fu, Y. X. Chen, W. X. Rong, X. Li, and D. N. Shi, "Plasmonic properties of individual heterogeneous dimers of Au and In nanospheres," *Physics Letters, Section A: General, Atomic and Solid State Physics*, vol. 391, p. 127131, 2021.

[210] V. Amendola, R. Pilot, M. Frasconi, O. M. Maragò, and M. A. Iatì, "Surface plasmon resonance in gold nanoparticles: A review," *Journal of Physics Condensed Matter*, vol. 29, no. 20, 2017.

[211] R. Gill, L. Tian, W. R. Somerville, E. C. Le Ru, H. Van Amerongen, and V. Subramaniam, "Silver nanoparticle aggregates as highly efficient plasmonic antennas for fluorescence enhancement," *Journal of Physical Chemistry C*, vol. 116, no. 31, pp. 16687–16693, 2012.

[212] C. A. Downing and G. Weick, "Plasmonic modes in cylindrical nanoparticles and dimers," *Proceedings of the Royal Society A: Mathematical, Physical and Engineering Sciences*, vol. 476, pp. 1–20, 12 2020.

[213] X. Fan, W. Zheng, and D. J. Singh, "Light scattering and surface plasmons on small spherical particles," *Light: Science and Applications*, vol. 3, no. November 2013, pp. 1–14, 2014.

[214] N. J. Greybush, V. Pacheco-Penã, N. Engheta, C. B. Murray, and C. R. Kagan, "Plasmonic Optical and Chiroptical Response of Self-Assembled Au Nanorod Equilateral Trimers," *ACS Nano*, vol. 13, no. 2, pp. 1617–1624, 2019.

[215] K. R. Ryu and J. W. Ha, "Influence of shell thickness on the refractive index sensitivity of localized surface plasmon resonance inflection points in silver-coated gold nanorods," *RSC Advances*, vol. 10, no. 29, pp. 16827–16831, 2020.

[216] Y. Huang, L. Ma, M. Hou, J. Li, Z. Xie, and Z. Zhang, "Hybridized plasmon modes and near-field enhancement of metallic nanoparticle-dimer on a mirror," *Scientific Reports*, vol. 6, no. July, pp. 1–9, 2016.

[217] S. Panaro, F. De Angelis, and A. Toma, "Dark and bright mode hybridization: From electric to magnetic Fano resonances," *Optics and Lasers in Engineering*, vol. 76, pp. 64–69, 2016.

[218] F. Hao, P. Nordlander, M. T. Burnett, and S. A. Maier, "Enhanced tunability and linewidth sharpening of plasmon resonances in hybridized metallic ring/disk nanocavities," *Physical Review B - Condensed Matter and Materials Physics*, vol. 76, no. 24, pp. 1–6, 2007.

[219] P. Nordlander, C. Oubre, E. Prodan, K. Li, and M. I. Stockman, "Plasmon hybridization in nanoparticle dimers," *Nano Letters*, vol. 4, no. 5, pp. 899–903, 2004.

[220] C. Y. Tsai, J. W. Lin, C. Y. Wu, P. T. Lin, T. W. Lu, and P. T. Lee, "Plasmonic coupling in gold nanoring dimers: Observation of coupled bonding mode," *Nano Letters*, vol. 12, no. 3, pp. 1648–1654, 2012.

[221] H. Yang, E. O. Owiti, X. Jiang, S. Li, P. Liu, and X. Sun, "Localized Surface Plasmon Resonance Dependence on Misaligned Truncated Ag Nanoprism Dimer," *Nanoscale Research Letters*, vol. 12, 2017.

[222] Z. Shen and L. Su, "Plasmonic trapping and tuning of a gold nanoparticle dimer," *Optics Express*, vol. 24, no. 5, p. 4801, 2016.

[223] N. Zohar, L. Chuntonov, and G. Haran, "The simplest plasmonic molecules: Metal nanoparticle dimers and trimers," *Journal of Photochemistry and Photobiology C: Photochemistry Reviews*, vol. 21, pp. 26–39, 2014.

[224] T. K. Hakala, H. T. Rekola, A. I. Väkeväinen, J. P. Martikainen, M. Nečada, A. J. Moilanen, and P. Törmä, "Lasing in dark and bright modes of a finite-sized plasmonic lattice," *Nature Communications*, vol. 8, pp. 1–7, 2017.

[225] V. Pacheco-Peña, R. A. Alves, and M. Navarro-Cía, "From symmetric to asymmetric bowtie nanoantennas: Electrostatic conformal mapping perspective," *Nanophotonics*, vol. 9, no. 5, pp. 1177–1187, 2020.

[226] A. S. Saadeldin, M. F. O. Hameed, E. M. Elkaramany, and S. S. Obayya, "Highly Sensitive Terahertz Metamaterial Sensor," *IEEE Sensors Journal*, vol. 19, no. 18, pp. 7993–7999, 2019.

[227] G. Lilley, M. Messner, and K. Unterrainer, "Improving the quality factor of the localized surface plasmon resonance," *Optical Materials Express*, vol. 5, no. 10, p. 2112, 2015.

[228] M. Horák, A. Konečná, T. Šikola, and V. Křápek, "Spatio-spectral metrics in electron energy loss spectroscopy as a tool to resolve nearly degenerate plasmon modes in dimer plasmonic antennas," *Nanophotonics*, vol. 12, pp. 3089–3098, 7 2023.

[229] U. Hohenester, H. Ditlbacher, and J. R. Krenn, "Electron-Energy-Loss Spectra of Plasmonic Nanoparticles," *Physical Review Letters*, vol. 103, p. 106801, 8 2009.

[230] A. Losquin and T. T. Lummen, "Electron microscopy methods for space-, energy-, and time-resolved plasmonics," *Frontiers of Physics*, vol. 12, no. 1, pp. 1–27, 2017.

[231] W. H. Yang, C. Zhang, S. Sun, J. Jing, Q. Song, and S. Xiao, "Dark plasmonic mode based perfect absorption and refractive index sensing," *Nanoscale*, vol. 9, no. 26, pp. 8907–8912, 2017.

[232] D. E. Gómez, Z. Q. Teo, M. Altissimo, T. J. Davis, S. Earl, and A. Roberts, "The dark side of plasmonics," *Nano Letters*, vol. 13, no. 8, pp. 3722–3728, 2013.

[233] J. Zuloaga and P. Nordlander, "On the energy shift between near-field and far-field peak intensities in localized plasmon systems," *Nano Letters*, vol. 11, no. 3, pp. 1280–1283, 2011.

[234] V. Pacheco-Peña, M. Beruete, P. Rodríguez-Ulibarri, and N. Engheta, "On the performance of an ENZ-based sensor using transmission line theory and effective medium approach," *New Journal of Physics*, vol. 21, p. 043056, 5 2019.

[235] E. Martinsson, B. Sepulveda, P. Chen, A. Elfwing, B. Liedberg, and D. Aili, "Optimizing the Refractive Index Sensitivity of Plasmonically Coupled Gold Nanoparticles," *Plasmonics*, vol. 9, no. 4, pp. 773–780, 2014.

[236] M. E. Stewart, C. R. Anderton, L. B. Thompson, J. Maria, S. K. Gray, J. A. Rogers, and R. G. Nuzzo, "Nanostructured plasmonic sensors," *Chemical Reviews*, vol. 108, no. 2, pp. 494–521, 2008.

[237] D. Murakami, H. Jinnai, and A. Takahara, "Wetting transition from the cassie-baxter state to the wenzel state on textured polymer surfaces," *Langmuir*, vol. 30, no. 8, pp. 2061–2067, 2014.

[238] J. Luo, J. Li, and Y. Lai, "Electromagnetic Impurity-Immunity Induced by Parity-Time Symmetry," *Physical Review X*, vol. 8, no. 3, p. 31035, 2018.

[239] T. Weiland, "A discretization model for the solution of Maxwell's equations for six-component fields," *Archiv Elektronik und Uebertragungstechnik*, vol. 31, pp. 116–120, 1977.

Appendix A

Derivation of the lens maker equation by Snell's law

The *lens maker equation* is a derivation that originates from the concept of geometrical optics [28]. The basis of geometric optics is to find the path of light rays (energy flowing in geometric lines) and therefore uses some assumptions:

- EM light in homogeneous media will propagate as straight *beams of light*.
- The beams will be reflected and refracted.
- Each light beam will propagate without affecting the others.
- *Natural* light sources are uncorrelated, with the light beams overlapping without interfering.

As optical wavelengths are relatively short, the first and last assumptions can be proven experimentally to not hold due to EM waves diffracting with mesoscale features and interfering. However, these principles are still effective at designing lenses, devices which can control and reshape wave fronts through refraction.

Consider a lens with rotational symmetry around the axis. When the lens is thicker at the centre than the edges (delaying the wavefront more) with a value of n greater than the surrounding medium, this will be considered a converging lens. This will increase the forward bending of the beam. A diverging lens causes the opposite effect. Now, consider two surfaces with radii of curvature of R_1 and R_2, respectively, with the vertices of the surfaces separated by a distance d. The refractive index of the media which separate the surfaces are

denoted as n_1, n_2 and n_3. The focal lengths of the first surface will be:

$$f_{o1} = \frac{n_1}{P_1} \tag{A.1}$$

$$f_{i1} = \frac{n_2}{P_1} \tag{A.2}$$

where $P_1 = \frac{n_2 - n_1}{R_1}$ is the magnifying power of the surface and the focal lengths of the second surface are defined as:

$$f_{o2} = \frac{n_2}{P_2} \tag{A.3}$$

$$f_{i2} = \frac{n_3}{P_2} \tag{A.4}$$

where $P_2 = \frac{n_3 - n_2}{R_2}$. These equations are then combined to find the distance between the two focal points of the total lens:

$$d_F = d - f_{i1} - f_{o2} = d - n_2 \left(\frac{1}{P_1} + \frac{1}{P_2} \right) \tag{A.5}$$

By then defining the parameter $P = -\frac{P_1 P_2 d}{n_2}$, the two surfaces can be combined to produce the total power:

$$P = P_1 + P_2 - \frac{t}{n_2} P_1 P_2 \tag{A.6}$$

and the principle points of the lens (P_o and P_i) relative to the first surface:

$$p_1 = f_{o1} \frac{d}{d_F} = \frac{n_1}{n_2} \frac{P_2}{P} d \tag{A.7}$$

$$p_2 = f_{i2} \frac{d}{d_F} = -\frac{n_3}{n_2} \frac{P_1}{P} d \tag{A.8}$$

Then for the simplest case when the lens is immersed in a single material ($n_1 = n_3$):

$$f = \left[\frac{n_2}{n_1} \left(\frac{1}{R_1} - \frac{1}{R_2} + \frac{\frac{n_2}{n_1} - 1}{n_2} \frac{d}{R_1 R_2} \right) \right]^{-1} = \frac{1}{P} \tag{A.9}$$

Appendix B

Collaborative work

In the realm of my work, I have assisted with other projects. Here, I will briefly describe the work but more details can be found in their respective publications.

B.1 Exploiting parity-time symmetry with epsilon near zero media emulated using rectangular waveguides operating near the cutoff frequency

In this work, an ENZ material is emulated using a rectangular waveguide operating near the cutoff frequency of its dominant TE_{10} mode. However, as explained in Section 1.2.3, there is a significant impedance mismatch when an EM wave is indicated on an area emulating an ENZ material. Therefore, a technique which has been used mathematically, known as Partity-time symmetry, [238] is exploited to achieve asymmetric reflection and enhancement transmission by positioning the rectangular waveguide between balanced loss and gain blocks. A comprehensive numerical and analytical study is conducted to find exceptional points where asymmetric reflection and enhancement transmission are demonstrated while maintaining the ENZ behaviour of the waveguide [68].

B.2 Generating photonic nanojets with truncated dielectric particles on optical fibers

This work furthers the discussion of PNJs in Section 2.1, where a high-refractive index mesoscale dielectric article is used at the end of an optical fibre to produce high-spatial resolution focusing of telecommunication wavelength ($\lambda_0 = 1550\,\text{nm}$) EM waves. Here, the

PNJs are explored in both 2D and 3D with a whole dielectric particle and a truncated particle, demonstrating the improved performance of the latter by shifting the PNJ towards the output surface. The transversal resolution of the PNJ is comprehensively analysed demonstrating sub-diffraction limit values of FWHM [144].

Appendix C

Material characterisation – Implementing alternative materials for photonics structures

Photonic devices, using compact and lightweight structures, efficiently control EM waves across a wide frequency spectrum, making them essential in telecommunications, computing, biomedicine, and spectroscopy. Advances in photonics predominantly use materials like metal-oxides, silicon, and germanium for their excellent NIR and visible frequency properties, such as low losses and high refractive indices, enabling efficient and compact photonic devices. Recently, polymers like PMMA have emerged as alternative materials.

Additive manufacturing, particularly 3D printing, has evolved from rapid prototyping to a viable alternative to traditional manufacturing, benefiting many fields, including optical and photonic applications, primarily at THz frequencies but less so at NIR wavelengths crucial for telecommunications.

This appendix explores using FDM 3D printing with commercially available polymers to fabricate structures for photonic applications at telecommunication wavelengths (1520 nm to 1630 nm). Polymers like PLA, rPLA, rPET, and BVOH, chosen for their renewable, recycled, or water-soluble properties, are printed and characterised to assess their EM properties. An open-bench photonics setup is used to measure the reflection (R) and transmission (T) spectra, from which the refractive index (n) and extinction coefficient (κ) are derived.

In the 3D printing process, samples are created using a Raise3D Pro2 printer with a nozzle diameter of 0.2 mm and a glass bed for smooth surfaces. Printed samples are analysed for thickness consistency and surface quality, confirming solid structure with minimal deviations.

The experimental setup measures R and T spectra for each polymer at multiple positions. The data show that as sample thickness increases, T decreases significantly while R slightly

reduces, indicating higher absorption ($A = 1 - R - T$) for thicker samples. Calculations of n and κ are performed using normalised R and T spectra, considering the incoherence of reflected and transmitted waves due to sample surface imperfections. This methodology allows evaluating the potential of these polymers in photonic applications at telecommunication wavelengths.

Appendix D

Surface Plasmon Polariton Derivation

In this appendix, different SPP configurations will be explored. A single insulator-metal interface will be studied first. Then a more complex configuration of insulator-insulator-metal-insulator (IIMI) and the effect of the metal and dielectric layer in this configuration. These studies will use A, B, C, D, E and F constants.

D.1 Insulator-metal (IM)

First, the effective propagation constant will be expressed in an insulator-metal interface. To start, Maxwell's assumption is used that the media is free of external charges and currents:

$$\nabla \times \mathbf{E} = -\frac{\partial \mathbf{B}}{\partial t} \rightarrow -j\omega\mu H \tag{D.1}$$

$$\nabla \times \mathbf{H} = -\frac{\partial \mathbf{D}}{\partial t} \rightarrow -j\omega\varepsilon E \tag{D.2}$$

As SPPs are TM waves assuming they propagate in the z-direction then $E_x = H_y = H_z = 0$ meaning $H_x \neq 0, E_y \neq 0, E_z \neq 0$ so the electric field components can determined as:

$$E_y = \frac{j}{\omega\varepsilon}\frac{\partial H_y}{\partial z} = \begin{cases} \frac{\beta}{\omega\varepsilon_1} A e^{jk_1 y} e^{-j\beta z}; y < 0 \\ \frac{\beta}{\omega\varepsilon_2} A e^{-jk_2 y} e^{-j\beta z}; y < 0) \end{cases} \tag{D.3}$$

$$E_z = -\frac{j}{\omega\varepsilon}\frac{\partial H_x}{\partial y} = \begin{cases} -\frac{j}{\omega\varepsilon_1}(k_1) A e^{jk_1 y} e^{-j\beta z}; y < 0 \\ -\frac{j}{\omega\varepsilon_2}(-k_2) A e^{-jk_2 y} e^{-j\beta z}; y < 0 \end{cases} \tag{D.4}$$

and the magnetic field can be expressed as:

$$H = H_x = Af(y)e^{-j\beta z} \tag{D.5}$$

where $f(y)$ is the magnetic field dependence considering the interface of both materials and $\beta = k_{zr} - jk_{zi}$ which is the wave number that is parallel to the insulator-metal interface.

$$f(y) = \begin{cases} e^{k_1 y} = e^{y\sqrt{\beta^2 - \varepsilon_1 k_0^2}}; y < 0 \\ e^{-k_2 y} = e^{-y\sqrt{\beta^2 - \varepsilon_{2r} k_0^2}}; y > 0 \end{cases} \tag{D.6}$$

There is a discontinuity with the Electric field (E_y) perpendicular to the direction of propagation, z, which results in coupling to the oscillations in the free-electron density at the metal surface which present as surface waves.

If continuity is then applied on the electric field's tangential components $E_{z(1)} = E_{z(2)}$ at the interface between the insulator and metal ($y = 0$) which allows the dispersion relation to be determined as:

$$-k_1 \varepsilon_2 = k_2 \varepsilon_1 \tag{D.7}$$

Which can then be used to solve for:

$$k_1 = \frac{k_0 \varepsilon_1}{\sqrt{\varepsilon_1 + \varepsilon_2}} \tag{D.8}$$

$$k_1 = \frac{k_0 \varepsilon_2}{\sqrt{\varepsilon_1 + \varepsilon_2}} \tag{D.9}$$

$$\beta = k_0 \sqrt{\frac{\varepsilon_1 \varepsilon_2}{\varepsilon_1 + \varepsilon_2}} \tag{D.10}$$

D.2 Insulator-metal-insulator (IMI)

Next, the case of a metal surrounded by two semi-infinite dielectrics is studied where most of the same steps can be used as with an insulator-metal interface.

REGION 1: $y < -t$

$$E_y = \frac{A}{\omega \varepsilon_1} \beta e^{k_1 y} e^{(} - j\beta z) = \frac{A}{\omega \varepsilon_1} \beta e^{\sqrt{\beta^2 - \varepsilon_1 k_0^2}} e^{-j\beta z} \tag{D.11}$$

$$E_z = -\frac{j}{\omega \varepsilon_1} k_1 A e^{k_3 y} e^{-j\beta z} = -\frac{j}{\omega \varepsilon_1} k_1 A e^{\sqrt{\beta^2 - \varepsilon_1 k_0^2}} e^{-j\beta z} \tag{D.12}$$

$$H_x = A e^{k_1 y} e^{-j\beta z} = A e^{\sqrt{\beta^2 - \varepsilon_1 k_0^2}} e^{-j\beta z} \tag{D.13}$$

REGION 2: $y > t$

$$E_y = \frac{B}{\omega\varepsilon_3}\beta e^{k_3 y}e^{-j\beta z} = \frac{B}{\omega\varepsilon_3}\beta e^{\sqrt{\beta^2-\varepsilon_1 k_0^2}}e^{-j\beta z} \tag{D.14}$$

$$E_z = -\frac{j}{\omega\varepsilon_3}k_3 B e^{-k_3 y}e^{-j\beta z} = -\frac{j}{\omega\varepsilon_3}k_3 B e^{\sqrt{\beta^2-\varepsilon_3 k_0^2}}e^{-j\beta z} \tag{D.15}$$

$$H_x = B e^{-k_3 y}e^{-j\beta z} = B e^{\sqrt{\beta^2-\varepsilon_3 k_0^2}}e^{-j\beta z} \tag{D.16}$$

REGION 3: $t < y < -t$

$$E_y = \frac{\beta}{\omega\varepsilon_2}e^{-j\beta z}(Ce^{k_2 y} + De^{k_2 y})$$
$$= \frac{\beta}{\omega\varepsilon_2}e^{-j\beta z}(Ce^{\sqrt{\beta^2-\varepsilon_2 k_0^2}} + De^{-\sqrt{\beta^2-\varepsilon_2 k_0^2}}) \tag{D.17}$$

$$E_z = -\frac{j}{\omega\varepsilon_2}k_2 e^{-j\beta z}(De^{-k_2 y} - Ce^{k_2 y})$$
$$= -\frac{j}{\omega\varepsilon_2}k_2 e^{-j\beta z}(De^{-\sqrt{\beta^2-\varepsilon_2 k_0^2}} - Ce^{\sqrt{\beta^2-\varepsilon_2 k_0^2}}) \tag{D.18}$$

$$H_x = Ce^{k_2 y}e^{-j\beta z} + De^{-k_2 y}e^{-j\beta z}$$
$$= Ce^{\sqrt{\beta^2-\varepsilon_2 k_0^2}}e^{-j\beta z} + De^{-\sqrt{\beta^2-\varepsilon_2 k_0^2}}e^{-j\beta z} \tag{D.19}$$

So if the boundary conditions are applied for the insulator-metal interface at the 2 interfaces:

$$Ae^{-k_1 t} = Ce^{-k_2 t} + De^{k_2 t} \tag{D.20}$$

$$\frac{-k_1}{\varepsilon_1}Ae^{-k_1 t} = -\frac{k_2}{\varepsilon_2}Ce^{-k_2 t} + \frac{k_2}{\varepsilon_2}De^{k_2 t} \tag{D.21}$$

$$Be^{-k_3 t} = Ce^{k_2 t} + De^{-k_2 t} \tag{D.22}$$

$$\frac{k_3}{\varepsilon_3}Be^{-k_3 t} = -\frac{k_2}{\varepsilon_2}Ce^{k_2 t} + \frac{k_2}{\varepsilon_2}De^{-k_2 t} \tag{D.23}$$

These 4 coupled equations still require H_x to fulfil the wave equation in the three regions by:

$$k_i^2 = \beta^2 - k_0^2\varepsilon_i \tag{D.24}$$

where i = 1,2,3 of the dielectric, metal and dielectric layers, respectively. By combining this system of equations through algebra which can be solved, then a transcendental equation is produced:

$$e^{2k_2 t}\left[\frac{\left(\frac{k_2}{\varepsilon_2}+\frac{k_1}{\varepsilon_1}\right)\left(\frac{k_2}{\varepsilon_2}+\frac{k_3}{\varepsilon_3}\right)}{\left(\frac{k_2}{\varepsilon_2}-\frac{k_1}{\varepsilon_1}\right)\left(\frac{k_2}{\varepsilon_2}-\frac{k_3}{\varepsilon_3}\right)}\right]=1 \tag{D.25}$$

Which can be numerically solved to determine the propagation constant and thus the complex effective refractive index:

$$n_{eff}=\beta k_0 \tag{D.26}$$

D.3 Insulator-insulator-metal-insulator (IIMI) & Insulator-Insulator-metal (IIM)

Next, the case of a metal surrounded by two semi-infinite dielectrics with an additional finite dielectric sandwiched between them is considered, using similar steps to the insulator-metal case.

REGION 1: $y<-t/2$

$$E_y=\frac{A}{\omega\varepsilon_1}\beta e^{k_1 y}e^{(}-j\beta z)=\frac{A}{\omega\varepsilon_1}\beta e^{\sqrt{\beta^2-\varepsilon_1 k_0^2}}e^{-j\beta z} \tag{D.27}$$

$$E_z=-\frac{j}{\omega\varepsilon_1}k_1 A e^{k_3 y}e^{-j\beta z}=-\frac{j}{\omega\varepsilon_1}k_1 e^{\sqrt{\beta^2-\varepsilon_1 k_0^2}}e^{-j\beta z} \tag{D.28}$$

$$H_x=Ae^{k_1 y}e^{-j\beta z}=Ae^{\sqrt{\beta^2-\varepsilon_1 k_0^2}}e^{-j\beta z} \tag{D.29}$$

REGION 2: $-t/2 < y < t/2$

$$E_y = \frac{\beta}{\omega\varepsilon_2} e^{-j\beta z}(Be^{k_2 y} + Ce^{-k_2 y})$$
$$= \frac{\beta}{\omega\varepsilon_2} e^{-j\beta z}(Be^{\sqrt{\beta^2-\varepsilon_2 k_0^2}} + Ce^{-\sqrt{\beta^2-\varepsilon_2 k_0^2}}) \tag{D.30}$$

$$E_z = -\frac{j}{\omega\varepsilon_2} k_2 e^{-j\beta z}(Ce^{-k_2 y} - Be^{k_2 y})$$
$$= -\frac{j}{\omega\varepsilon_2} k_2 e^{-j\beta z}(De^{-\sqrt{\beta^2-\varepsilon_2 k_0^2}} - Ce^{\sqrt{\beta^2-\varepsilon_2 k_0^2}}) \tag{D.31}$$

$$H_x = Be^{k_2 y}e^{-j\beta z} + Ce^{-k_2 y}e^{-j\beta z}$$
$$= Ce^{\sqrt{\beta^2-\varepsilon_2 k_0^2}}e^{-j\beta z} + De^{-\sqrt{\beta^2-\varepsilon_2 k_0^2}}e^{-j\beta z} \tag{D.32}$$

REGION 3: $t/2 < y < l_y$

$$E_y = \frac{\beta}{\omega\varepsilon_3} e^{-j\beta z}(Ce^{k_3 y} + De^{-k_3 y})$$
$$= \frac{\beta}{\omega\varepsilon_3} e^{-j\beta z}(De^{\sqrt{\beta^2-\varepsilon_3 k_0^2}} + Ee^{-\sqrt{\beta^2-\varepsilon_3 k_0^2}}) \tag{D.33}$$

$$E_z = -\frac{j}{\omega\varepsilon_3} k_3 e^{-j\beta z}(Ee^{-k_3 y} - De^{k_3 y})$$
$$= -\frac{j}{\omega\varepsilon_3} k_3 e^{-j\beta z}(Ee^{-\sqrt{\beta^2-\varepsilon_3 k_0^2}} - De^{\sqrt{\beta^2-\varepsilon_3 k_0^2}}) \tag{D.34}$$

$$H_x = De^{k_3 y}e^{-j\beta z} + Ee^{-k_3 y}e^{-j\beta z}$$
$$= De^{\sqrt{\beta^2-\varepsilon_3 k_0^2}}e^{-j\beta z} + De^{-\sqrt{\beta^2-\varepsilon_3 k_0^2}}e^{-j\beta z} \tag{D.35}$$

Again applying the boundary conditions for the insulator-metal interface at the 2 interfaces:

$$Ae^{-\frac{1}{2}k_1 t} = Be^{-\frac{1}{2}k_2 t} + Ce^{\frac{1}{2}k_2 t} \tag{D.36}$$

$$-\frac{k_1}{\varepsilon_1} Ae^{-\frac{1}{2}k_1 t} = -\frac{k_2}{\varepsilon_2} Be^{-\frac{1}{2}k_2 t} + \frac{k_2}{\varepsilon_2} Ce^{\frac{1}{2}k_2 t} \tag{D.37}$$

$$Ae^{\frac{1}{2}k_2 t} + Be^{-\frac{1}{2}k_2 t} = Ce^{\frac{1}{2}k_3 t} + De^{-\frac{1}{2}k_3 t} \tag{D.38}$$

$$-\frac{k_2}{\varepsilon_2} Be^{-\frac{1}{2}k_2 t} + \frac{k_2}{\varepsilon_2} Ce^{-\frac{1}{2}k_2 t} = -\frac{k_3}{\varepsilon_3} De^{\frac{1}{2}k_3 t} + \frac{k_3}{\varepsilon_3} Ee^{-\frac{1}{2}k_3 t} \tag{D.39}$$

Then finally using the boundary conditions at the surface of the dielectric:

$$De^{k_3(\frac{1}{2}t+l_y)} + Ee^{-k_3(\frac{1}{2}t+l_y)} = Fe^{-k_4(\frac{1}{2}t+l_y)} \tag{D.40}$$

$$-\frac{k_3}{\varepsilon_3}Ae^{k_3(\frac{1}{2}t+l_y)} + \frac{k_3}{\varepsilon_3}Be^{-k_3(\frac{1}{2}t+l_y)} = \frac{k_4}{\varepsilon_4}Ce^{-k_4(\frac{1}{2}t+l_y)} \tag{D.41}$$

Again these two equations can be reduced and rearranged into matrix form which can be reduced into another transcendental expression:

$$Be^{-\frac{1}{2}k_2t}\left(\frac{k_2}{\varepsilon_2} - \frac{k_1}{\varepsilon_1}\right) - Ce^{\frac{1}{2}k_2t}\left(\frac{k_2}{\varepsilon_2} + \frac{k_1}{\varepsilon_1}\right) = 0 \tag{D.42}$$

$$De^{k_3(\frac{1}{2}t+l_y)}\left(\frac{k_4}{\varepsilon_4} - \frac{k_3}{\varepsilon_3}\right) + Ee^{-k_3(\frac{1}{2}t+l_y)}\left(\frac{k_4}{\varepsilon_4} - \frac{k_3}{\varepsilon_3}\right) = 0 \tag{D.43}$$

$$\begin{pmatrix} e^{\frac{1}{2}k_2t} & e^{-\frac{1}{2}k_2t} & -e^{\frac{1}{2}k_3t} & e^{-\frac{1}{2}k_3t} \\ -\frac{k_2}{\varepsilon_2}e^{\frac{1}{2}k_2t} & \frac{k_2}{\varepsilon_2}e^{-\frac{1}{2}k_2t} & \frac{k_3}{\varepsilon_3}e^{\frac{1}{2}k_3t} & -\frac{k_3}{\varepsilon_3}e^{-\frac{1}{2}k_3t} \\ e^{-\frac{1}{2}k_2t}\left(\frac{k_2}{\varepsilon_2} - \frac{k_1}{\varepsilon_1}\right) & -e^{\frac{1}{2}k_2t}\left(\frac{k_2}{\varepsilon_2} + \frac{k_1}{\varepsilon_1}\right) & 0 & 0 \\ 0 & 0 & e^{k_3\left(\frac{1}{2}t+h\right)}\left(\frac{k_4}{\varepsilon_4} + \frac{k_3}{\varepsilon_3}\right) & e^{-k_3\left(\frac{1}{2}t+h\right)}\left(\frac{k_4}{\varepsilon_4} - \frac{k_3}{\varepsilon_3}\right) \end{pmatrix} \tag{D.44}$$

$$tanh(k_2l_y) = -\frac{\varepsilon_3k_3(k_2\varepsilon_2[k_4\varepsilon_1 + k_1\varepsilon_4]cosh(k_2t) + [k_1k_4\varepsilon_2^2 + k_2^2\varepsilon_1\varepsilon_4]sinh(k_2t))}{\varepsilon_2k_2([k_1k_4\varepsilon_3^2 + k_3^2\varepsilon_1\varepsilon_4]cosh(k_2t) + [k_1k_3^2\varepsilon_3^2\varepsilon_1 + k_2^2k_4\varepsilon_1\varepsilon_3^2]sinh(k_2t))} \tag{D.45}$$

where l_y tends to 0 this will become the case for IMI while if the metal layer becomes semi-infinite then this reduces down to:

$$tanh(k_3l_y) = -\left(\frac{\varepsilon_2\varepsilon_3k_3k_4 + \varepsilon_4\varepsilon_3k_2k_3}{\varepsilon_2\varepsilon_4k_3^2 + \varepsilon_3^2k_2k_4}\right) \tag{D.46}$$

Appendix E

Numerical Methods

In the realm of EM, commercial simulation software works by solving either the integral or differential forms of Maxwell's equations discussed in Section 1.1.1. In this thesis, two commercial software, CST Studio Suite® and COMSOL Multiphysics®, are used which will be discussed in more detail in the following sections.

E.1 CST Studio Suite®

CST Studio Suite®, is a prominent commercial software renowned for its efficacy in evaluating the EM response of different structures. Within this software, there are various EM solver products available, including CST Microwave Studio® for high-frequency range, with a comprehensive array of solver types, such as transient, frequency domain, integral equation, eigenmode, to name a few, CST EM Studio Suite® for low-frequency analysis, with solvers for static and low-frequency problems, and CST particle Studio Suite® for simulations where particle tracking is required. In the course of this thesis, only CST Microwave Studio® was used which is based on the Finite integration technique (FIT) which solves the integral form of Maxwell's equations[239]:

$$\oint_{\partial A} \vec{E} \cdot d\vec{s} = -\int_{A} \frac{\partial \vec{B}}{\partial t} \cdot d\vec{A} \tag{E.1}$$

$$\oint_{\partial A} \vec{H} \cdot d\vec{s} = \int_{A} \left(\frac{\partial \vec{D}}{\partial t} + \vec{J} \right) \cdot d\vec{A} \oint_{\partial V} \vec{B} \cdot d\vec{A} = 0 \tag{E.2}$$

$$\oint_{\partial V} \vec{D} \cdot d\vec{A} = \int_{V} \rho dV \tag{E.3}$$

First, the structures are designed using the graphical solid modelling front end of the software. The structure is then divided into a series of mesh cells by the automatic meshing procedure contained in the software. The primary mesh can be viewed in the software using *mesh view* but a secondary mesh which is not visualised is also applied orthogonally to the first. Using these two meshes together Maxwell's equations are spatial discretised. The type of mesh is designated by the application with three mesh types available: hexahedral, tetrahedral and surface. The time domain/transient solver, the only solver of CST microwave Studio® used as part of this thesis, uses a hexahedral mesh, shown in Fig. E.1 as a hexahedral mesh on the dual dielectric structures discussed in Chapter 2, while a frequency domain solver will use either hexahedral or tetrahedral.

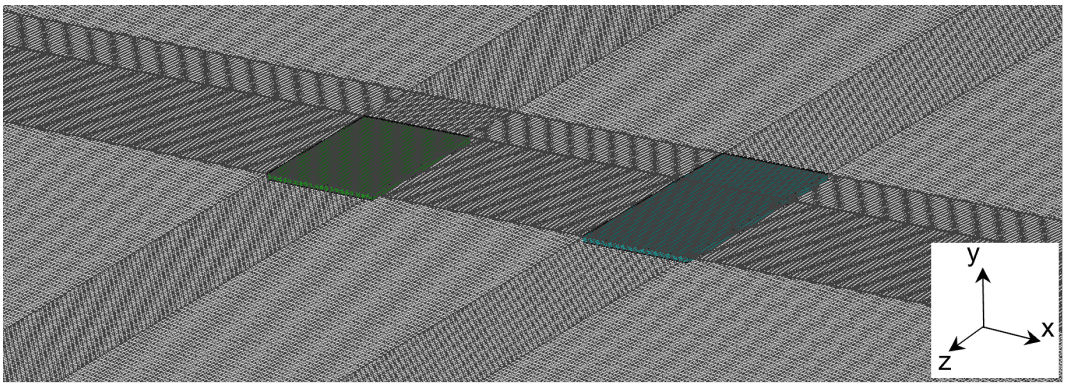

Fig. E.1 Perspective screenshot from CST microwave studio of the hexahedral mesh used for the dual-dielectric structures Chapter 2

E.1.1 Transient/time domain solver

The Transient solver of CST Microwave Studio® is a powerful and adaptable time-domain solver, capable of retrieving the full broadband response of the structures with a single simulation pass. This simulation solver has been demonstrated to be very effective for many applications operating at high frequencies such as antennas and transmission lines, among others. The time domain solver operates by calculating how fields develop at discrete time and position samples, considering the transmission of energy between ports and/or open space. However, if the structure under study is electrically much smaller than the smallest incident wavelength the efficiency of the solver significantly decreases and alternative solvers should be used, such as a frequency domain solver.

E.2 COMSOL Multiphysics®

The advanced numerical methods offered in terms of modelling and evaluation of complex physics-based problems have led to COMSOL Multiphysics® to emerge as a popular general-purpose software platform. It can even account for multiphysics phenomena with tools and interfaces for mechanical and chemical applications, coupling them together, with many different modules available for these wide-ranging applications such as RF, AC/DC, Semiconductor and Ray optics, among others. This software unlike CST Studio Suite® solves the differential form of Maxwell's equations. In the thesis, COMSOL Multiphysics® was typically used for plasmonic structures employing the RF module due to being a frequency domain solver so can better mesh and more accurately evaluate the relatively small features common in plasmonic structures.

E.2.1 RF module

The RF module of COMSOL Multiphysics® is a commonly used tool for designing a variety of devices working as microwave frequencies and above, such as circuits, waveguides and antennas, among others. This is due to the properties of these structures that can be determined such as S-parameters, reflection, transmission, and electromagnetic field distributions by simulation of the electromagnetic wave propagation and resonances. In terms of the thesis the frequency domain solver was the only interface used but due to the *multiphysics* aspect of COMSOL Multiphysics® other physical effects could have been considered such as temperature which can change the behaviour of a structure. The frequency-domain solver again meshes the structure using either semi-automatic, such as free tetrahedral meshing which can be manually configured, or automatic meshing with meshing sweeps. Typically for the studies in the thesis, a combination of manual and automatic techniques were used. An example of the tetrahedral meshing for the plasmonic meniscus lens from Chapter 3 is shown in Fig. E.2.

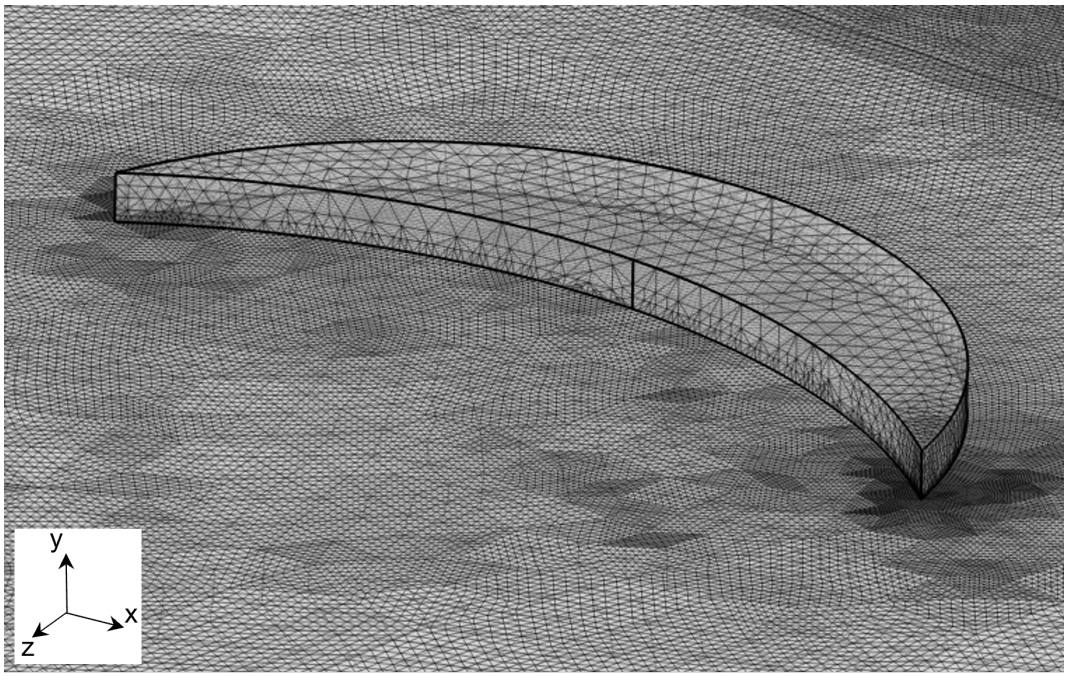

Fig. E.2 Perspective screenshot from COMSOL multiphysics of the tetrahedral mesh used for the plasmonic meniscus lens Chapter 3

Appendix F

Publications list and Awards

- Total publications: 5 (+1 in preparation)
- Total international conference submissions: 22
- Google Scholar h/i10 index: 3/2 (45+ citations)

F.1 Fully Peer-reviewed manuscripts

- **J. A. Riley**, M. Horák, C. Johnson-Richards, N. Healy, V. Křápek, and V. Pacheco-Peña, "Plasmonic sensing using Babinet's principle," Nanophotonics, 12, 20, 2023, pp. 3895–3909, doi:10.1515/nanoph-2023-0317.
- W. Aljuaid, **J. A. Riley**, N. Healy, and V. Pacheco-Peña, "On-fiber high-resolution photonic nanojets via high refractive index dielectrics," Opt. Express, 30, 24, p. 43678, Nov. 2022, doi: 10.1364/OE.474894.
- **J. A. Riley**, N. Healy, and V. Pacheco-Peña, "Plasmonic meniscus lenses," Sci. Rep., 12, 1, p. 894, 2022, doi: 10.1038/s41598-022-04954-0.
- M. Nicolussi, **J. A. Riley**, and V. Pacheco-Peña, "Unidirectional transparency in epsilon-near-zero based rectangular waveguides induced by parity-time symmetry," Appl. Phys. Lett., 119, 26, p. 263507, Dec. 2021, doi: 10.1063/5.0076236.
- V. Pacheco-Peña, **J. A. Riley**, C.-Y. Liu, O. V Minin, and I. V Minin, "Diffraction limited photonic hook via scattering and diffraction of dual-dielectric structures," Sci. Rep., 11, 1, p. 20278, Dec. 2021, doi: 10.1038/s41598-021-99744-5.

F.2 International conference submissions

- **J. A. Riley**, M. Horák, C. Johnson-Richards, N. Healy, V. Křápek, and V. Pacheco-Peña "On the performance of plasmonic sensors enabled by Babinet's principle" 1st URSI UK 2024
- **J. A. Riley**, C. Johnson-Richards, N. Healy, and V. Pacheco-Peña "Electromagnetic properties of additive manufactured polymers at telecommunication wavelengths" 1st URSI UK 2024
- **J. A. Riley**, M. Horák, C. Johnson-Richards, N. Healy, V. Křápek, and V. Pacheco-Peña "Towards dielectric sensing via Babinet's principle-inspired plasmonic platforms" Under review for 4th URSI Atlantic Radio Science Meeting (AT-RASC) 2024
- **J. A. Riley**, M. Horák, V. Křápek and V. Pacheco-Peña, "Dielectric Sensing by Babinet's Principle in Plasmonics," 17th International Congress on Artificial Materials for Novel Wave Phenomena, Metamaterials 2023, 2023, pp. X-300-X-302, doi:10.1109/Metamaterials58257.2023.10289502.
- **J. A. Riley**, M. Horák, V. Křápek and V. Pacheco-Peña, "Using Babinet's principle in plasmonics for dielectric sensing," 2023 XXXVth General Assembly and Scientific Symposium of the International Union of Radio Science (URSI GASS), August, 2023, pp. 1–4, doi:10.23919/URSIGASS57860.2023.10265586..
- Alessandro Ventisei, Tony Knightley, Ross Macdonald, **J. A. Riley**, Alex Yakovlev, Victor Pacheco-Peña., "Utilizing Petri-Nets to Represent Electromagnetic Waveguide Junction Switching Processes," 2023 XXXVth General Assembly and Scientific Symposium of the International Union of Radio Science (URSI GASS), August, 2023, pp. 1–4, doi:10.46620/URSIGASS.2023.0750.DMMN9628
- **J. A. Riley**, Oleg V. Minin, Igor V. Minin, Victor Pacheco-Peña, "Generating photonic hooks using dual-dielectric designs" 2023 XXXVth General Assembly and Scientific Symposium of the International Union of Radio Science (URSI GASS), August, 2023.
- M. Horák, V. Čalkovský, V. Křápek, **J. A. Riley**, V. Pacheco-Peña, J. Mach, and T. Šikola, "Plasmon Resonances in Ga Nanoparticles and Plasmonic Antennas for Biosensing," 13th Int. Conf. Metamaterials, Photonic Cryst. Plasmon. META 2023, 2023.

- **J. A. Riley** et al., "Designing plasmonic sensors using Babinet's principle," 2023 Conference on Lasers and Electro-Optics Europe and European Quantum Electronics Conference, CLEO/Europe-EQEC 2023, 2023, pp. 4599, doi:10.1109/CLEO/EUROPE-EQEC57999.2023.10232614.

- **J. A. Riley**, N. Healy, and V. Pacheco-Peña, "Exploiting effective media to make meniscus lenses for surface plasmon polariton focusing," in 2022 Sixteenth International Congress on Artificial Materials for Novel Wave Phenomena (Metamaterials), Sep. 2022, pp. X-365-X–367. doi: 10.1109/Metamaterials54993.2022.9920842.

- **J. A. Riley**, O. V. Minin, I. V. Minin, and V. Pacheco-Peña, "Exploiting dual-dielectric devices to produce photonic hooks," in 2022 Sixteenth International Congress on Artificial Materials for Novel Wave Phenomena (Metamaterials), Sep. 2022, pp. 368–370. doi: 10.1109/Metamaterials54993.2022.9920808.

- W. Aljuaid, **J. A. Riley**, N. Healy, and V. Pacheco-Peña, "Producing Photonic Nanojet Outside of Immersed High Refractive Index Engineered dielectrics on Optical Fibers," in 2022 Sixteenth International Congress on Artificial Materials for Novel Wave Phenomena (Metamaterials), Sep. 2022, pp. X-010-X–012. doi: 10.1109/Metamaterials54993.2022.9920871.

- M. Nicolussi, **J. A. Riley**, and V. Pacheco-Peña, "Parity-Time symmetry for near-zero reflection in Epsilon-Near-Zero media emulated by rectangular waveguides," in 2022 Sixteenth International Congress on Artificial Materials for Novel Wave Phenomena (Metamaterials), Sep. 2022, pp. X-329-X–331. doi: 10.1109/Metamaterials54993.2022.9920891.

- **J. A. Riley** et al., "Modelling and computing decision-making processes and temporal derivatives with electromagnetic waves," in 2022 Sixteenth International Congress on Artificial Materials for Novel Wave Phenomena (Metamaterials), Sep. 2022, pp. X-332-X–334. doi: 10.1109/Metamaterials54993.2022.9920916.

- **J. A. Riley**, N. Healy, and V. Pacheco-Peña, "Tailoring surface plasmon polaritons for lensing applications," U.K Semiconductors 2022.

- W. Aljuaid, **J. A. Riley**, N. Healy, and V. Pacheco-Peña, "Attaching truncated dielectric particles to optical fibres to produce high resolution focusing for imaging and sensing systems," 2022. doi: 10.1063/1.5086175.

- **J. A. Riley**, N. Healy, and V. Pacheco-Peña, "On the performance of plasmonic meniscus lenses for surface plasmon focusing," in 2022 3rd URSI Atlantic and Asia Pacific Radio Science Meeting (AT-AP-RASC), May 2022, pp. 1–4. doi: 10.23919/AT-AP-RASC54737.2022.9814416.
- **J. A. Riley**, N. Healy, and V. Pacheco-Peña, "Producing surface plasmon polariton focusing using all-metallic devices," in 2022 3rd URSI Atlantic and Asia Pacific Radio Science Meeting (AT-AP-RASC), May 2022, pp. 1–4. doi: 10.23919/AT-AP-RASC54737.2022.9814416.
- **J. A. Riley**, N. Healy, and V. Pacheco-Peña, "Exploiting the concept of effective media to manipulate surface plasmons without dielectrics," in XXXIV General Assembly and Scientific Symposium of the International Union of Radio Science, 2021, September. doi: 10.1021/nl051013j.K.
- **J. A. Riley**, N. Healy, and V. Pacheco-peña, "Exploiting meniscus lenses for surface plasmons focusing," in XXXIV General Assembly and Scientific Symposium of the International Union of Radio Science, 2021, September. doi: 10.1021/nl051013j.2.
- **J. A. Riley**, N. Healy, and V. Pacheco-Peña, "Controlling surface plasmons using all-metallic structures," 11th Int. Conf. Metamaterials, Photonic Cryst. Plasmon. META 2021, pp. 1–2, 2021.
- **J. A. Riley**, N. Healy, and V. Pacheco-Peña, "Manipulating Surface Plasmons Propagation Using Ultra-Compact and Non-Dielectric Designs," 2020 14th Int. Congr. Artif. Mater. Nov. Wave Phenomena, Metamaterials 2020,

F.3 Awards

- Young Scientist award - URSI GASS 2023
- 1st prize presentation - internal Newcastle University Engineering Conference 2021
- 3rd prize poster - internal Newcastle University Engineering Conference 2020